Chapter 6
Emittance Growth and Beam Loss

R. Carrigan, V. Lebedev, N. Mokhov, S. Nagaitsev, V. Shiltsev, G. Stancari, D. Still, and A. Valishev

A wide range of diffusion and beam loss mechanisms were studied during the Tevatron Run II commissioning and operations. Many of them were well known [Coulomb scattering, residual gas and intrabeam scattering (IBS)] but required substantial studies and deeper theoretical insights because of unique experimental conditions and beam parameters.

6.1 Single and Multiple Scattering

Conventionally, multiple and single particle scattering in a storage ring are considered to be independent. Such an approach is simple and often yields sufficiently accurate results. Nevertheless, there is a class of problems where such an approach is not adequate and single and multiple scattering need to be considered together. This can be achieved by solving an integro-differential equation for the particle distribution function, which correctly treats particle Coulomb scattering as well as the betatron motion. We start our consideration from the Fokker–Planck equation describing the evolution of particle distribution due to multiple scattering, then we consider multiple IBS, and finally we will move to a simultaneous treatment of multiple and single Coulomb scattering, where we will consider two problems: the beam scattering on the residual gas and an evolution of longitudinal particle distribution in a hadron collider due to single and multiple IBS.

R. Carrigan • V. Lebedev (✉) • N. Mokhov • S. Nagaitsev • V. Shiltsev • G. Stancari • D. Still • A. Valishev
Accelerator Physics Center, Fermi National Accelerator Laboratory, MS341, PO Box 500, Batavia, IL 60510, USA
e-mail: val@fnal.gov; shiltsev@fnal.gov

V. Lebedev and V. Shiltsev (eds.), *Accelerator Physics at the Tevatron Collider*, Particle Acceleration and Detection, DOI 10.1007/978-1-4939-0885-1_6,

6.1.1 Diffusion Equation in the Action-Phase Variables

Let $f(x, \theta, t)$ be a one-dimensional beam transverse phase-space distribution function at time t. In the presence of damping and diffusion the evolution of the function f in a ring can be described by a Fokker–Planck equation:

$$\frac{\partial f}{\partial t} + v_0\theta\frac{\partial f}{\partial x} + \frac{\partial}{\partial\theta}(\kappa(x,t)xf) = \frac{\partial}{\partial\theta}(\lambda(x,\theta,t)\theta f) + \frac{1}{2}\frac{\partial}{\partial\theta}\left(D_\theta(x,\theta,t)\frac{\partial f}{\partial\theta}\right). \quad (6.1)$$

Here the functions $\kappa(x, t)$, $\lambda(x, \theta, t)$ and $D_\theta(x, \theta, t)$ describe the focusing, damping, and diffusion in the ring, and $v_0 = \beta c$ is the average beam velocity. Making the transition to the action-phase variables (I, ψ), assuming that the distribution function does not depend on the phase ψ, and performing averaging over the ring circumference one obtains the general form of the Fokker–Planck equation for nonlinear oscillator:

$$\frac{\partial f}{\partial t} - \frac{\partial}{\partial I}(\lambda(I)If) = \frac{\omega(0)}{2}\frac{\partial}{\partial I}\left(\frac{D(I)}{\omega(I)}I\frac{\partial f}{\partial I}\right). \quad (6.2)$$

Here $\lambda(I)$ and $D(I)$ are the damping rate and the diffusion averaged over the betatron phase and the ring circumference, $\omega(I)$ is the betatron frequency, and the action for small amplitude betatron oscillations is introduced as follows:

$$I = \frac{1}{2}\left(\beta_x\theta^2 + 2\alpha_x x\theta + \frac{x^2}{\beta_x}\left(1 + a_x{}^2\right)\right). \quad (6.3)$$

In the case of three-dimensional motion the general form of Eq. (6.2) is:

$$\frac{\partial f}{\partial t} - \sum_{k=1}^{3}\frac{\partial}{\partial I_k}(\lambda_k(\mathbf{I})I_k f) = \frac{1}{2}\sum_{k=1}^{3}\omega_k(0)\frac{\partial}{\partial I_k}\left(\frac{D_k(\mathbf{I})}{\omega_k(\mathbf{I})}I_k\frac{\partial f}{\partial I_k}\right), \quad \mathbf{I} = \left(I_x, I_{y,}, I_z\right), k = x, y, z. \quad (6.4)$$

Note that Eqs. (6.2) and (6.4) conserve the number of particles.

In the case of linear focusing and damping, and amplitude independent diffusion the functions $\kappa(x, t)$, $\lambda(x, \theta, t)$ and $D_\theta(x, \theta, t)$ do not depend on x and θ; and they are directly related to the functions of Eq. (6.1) averaged over circumference (revolution time): $\lambda = \langle\lambda(t)\rangle_t$, $D = \langle\beta_x(t)D_\theta(t)\rangle_t$. That yields the following form of Fokker–Planck equation:

$$\frac{\partial f}{\partial t} - \lambda\frac{\partial}{\partial I}(If) = \frac{D}{2}\frac{\partial}{\partial I}\left(I\frac{\partial f}{\partial I}\right). \quad (6.5)$$

Multiplying Eq. (6.5) by I and integrating we obtain

$$\frac{d}{dt}\bar{I} \equiv \int_0^\infty I\frac{\partial f}{\partial t}dI = \int_0^\infty I\left(\frac{\partial}{\partial I}(\lambda I f) + \frac{1}{2}\frac{\partial}{\partial I}\left[DI\frac{\partial f}{\partial I}\right]\right)dI = -\lambda\bar{I} + \frac{D}{2}. \tag{6.6}$$

The replacement of action by the betatron amplitude $a = \sqrt{2I}$ converts the right-hand side of Eq. (6.5) being proportional to the two-dimensional laplacian of f:

$$\frac{D}{2}\frac{d}{dI}\left(I\frac{df}{dI}\right) = \frac{D}{4}\Delta_a f \equiv \frac{D}{4}\frac{1}{a}\frac{d}{da}\left(a\frac{df}{da}\right). \tag{6.7}$$

As an example of Eq. (6.5) application we will find the beam lifetime corresponding to the evolution of particle distribution at the stationary stage when all details of initial distribution are smeared out by diffusion and damping.[1] For unlimited aperture and nonzero damping rate the beam life time is infinite and the equilibrium distribution function is:

$$f(I,t) = Ce^{-I/I_0}, \tag{6.8}$$

where $I_0 = D/2\lambda$ is the average beam action. Further we assume that the aperture limitation is important for one dimension only. Then the boundary condition is: $f_0(I_b) = 0$, where I_b determines the ring acceptance. Looking for a solution in the following form:

$$f(I,t) = C\ \ e^{-t/\tau}f_0(I), \tag{6.9}$$

and substituting it into Eq. (6.5) one obtains

$$f_0'' + \left(\frac{1}{I} + \frac{1}{I_0}\right)f_0' + \frac{1}{II_0}\left(1 + \frac{1}{\lambda\tau}\right)f_0 = 0. \tag{6.10}$$

where τ is the beam intensity lifetime and C is a constant. The substitutions $\xi = -I/I_0$ and $a = 1 + 1/(\lambda\tau)$ reduce this equation to the equation of the confluent hypergeometric function ${}_1F_1(a,b,\xi)$ with $b = 1$. Thus the solution (for $\alpha, \lambda > 0$) is:

$$f_0(I) = {}_1F\left(1 + \frac{1}{\lambda\tau}, 1, -\frac{I}{I_0}\right). \tag{6.11}$$

[1] This case describes well the beam lifetime in an electron synchrotron when the horizontal beam emittance is set by equilibrium between synchrotron radiation (SR) damping and diffusion due to SR. The vertical emittance is much smaller and therefore the beam loss due to diffusion in vertical plane is negligible. It makes the problem being single dimensional.

where τ is determined by the requirement that the first root is located at $\xi = -I_b/I_0$, i.e., ${}_1F_1(1+1/(\lambda\tau), 1, -I_b/I_0) = 0$. In the practically interesting case of sufficiently large aperture the numerical solution yields approximate equation for beam lifetime:

$$\tau \approx \frac{0.612}{\lambda} \exp\left(0.812 \frac{I_b}{I_0}\right), \tag{6.12}$$

which has an accuracy better than 2 % for $2.2 < \sqrt{I_b/I_0} < 8$. In the absence of damping the solution is:

$$f(I,t) = C\ e^{-t/\tau} J_0\left(\mu_0 \sqrt{\frac{I}{I_b}}\right), \quad \tau = \frac{8 I_b}{D \mu_0{}^2}, \mu_0 = 2.405\ldots, \tag{6.13}$$

where $J_0(x)$ is the Bessel function of zero order and μ_0 is its first root.

In conclusion we will find the beam lifetime in the absence of cooling for the case of equal aperture limitations and equal diffusions for both the horizontal and vertical planes. We assume a round vacuum chamber, equal beta-functions and sufficiently small momentum spread so that its contribution to the beam sizes could be neglected. Then Eq. (6.4) can be rewritten in the following form:

$$\frac{\partial f}{\partial t} = \frac{D}{2}\left(\frac{\partial}{\partial I_x}\left(I_x \frac{\partial f}{\partial I_x}\right) + \frac{\partial}{\partial I_y}\left(I_y \frac{\partial f}{\partial I_y}\right)\right), \tag{6.14}$$

with the boundary condition $f_0(I_x, I_y)\big|_{I_x+I_y=I_b} = 0$. Making transition to amplitudes, $\left(a_x = \sqrt{2I_x}, \quad a_y = \sqrt{2I_y}\right)$ and using Eq. (6.7) we can rewrite Eq. (6.14) as follows:

$$\frac{\partial f}{\partial t} = \frac{D}{4} \Delta_4 f, \tag{6.15}$$

where Δ_4 denotes the laplacian in the four-dimensional phase space. An axial symmetric solution can be presented as a function of single variable—the radius in the four-dimensional space $a = \sqrt{a_x{}^2 + a_y{}^2}$. That yields:

$$\frac{\partial f_0}{\partial t} = \frac{D}{4} \frac{1}{a^3} \frac{d}{da}\left(a^3 \frac{df_0}{da}\right). \tag{6.16}$$

Looking for solution in the following form $f(a,t) = C\ e^{-t/\tau} f_0(a)/a$ with boundary condition $f_0\left(\sqrt{2I_b}\right) = 0$ one obtains:

$$f(I,t) = C \frac{e^{-t/\tau}}{\sqrt{I/I_b}} J_1\left(\mu_{10} \sqrt{\frac{I}{I_b}}\right), \quad \tau = \frac{8 I_b}{D \mu_{10}{}^2}, \mu_{10} = 3.832\ldots, \tag{6.17}$$

where function $J_1(x)$ is the Bessel function of the first order, and μ_{10} is its first root. Comparing Eqs. (6.13) and (6.17) one can see that the beam lifetime in the case of two-dimensional aperture limitation with round vacuum chamber is ≈2.54 times shorter than in the case of single dimensional aperture limitation.

6.1.2 Multiple IBS

IBS of charged particles in beams results in an exchange of energy between various degrees of freedom resulting in an increase of average energy of particles in the beam frame and an increase of the total beam emittance in 6D phase space. The total Coulomb cross section of a two-particle scattering in vacuum diverges; however, it has a finite value for collisions in plasma (or beam) due to field screening by other particles [1] or finite beam dimensions. Usually two scattering regimes are considered: (1) single scattering, when a rare single collision produces a large change of particle momentum (the Touschek effect), and (2) multiple scattering, when multiple frequent collisions cause diffusion. The first phenomenon is usually responsible for the creation of distribution tails and the beam loss in electron machines, while the second one for changes in the distribution core. Such separation is useful in many applications. It usually represents a good approximation for electron synchrotrons where the RF bucket length is much larger than the bunch length. However there are cases when it fails to deliver an accurate result. In particular it cannot be used to compute the beam lifetime in Tevatron where particles fill the entire RF bucket.

The IBS in accelerators is already a rather well-understood subject. The first decisive published work appears to be that of Piwinski [2], followed by Bjorken and Mtingwa [3]. These two earlier works were both carried out from first principles of two-body Coulomb collisions and largely ignored multiple scattering prior works on Coulomb scattering in plasma [4, 5] and astrophysics [6]. In what follows we re-derive the results of [3] using the Landau kinetic equation [4]. The new theoretical results include: (1) closed-form IBS rate expressions using symmetric elliptic integrals, (2) new IBS expressions for beams with coupled betatron motion and the vertical dispersion, and (3) a theoretical approach that combines the small and large angle Coulomb scattering. These new results are then compared with experimental measurements in several Fermilab machines.

Multiple Scattering in Single Component Plasma

Consider spatially homogeneous non-relativistic one-component plasma. The evolution of the velocity distribution function, $f(v_x, v_y, v_z)$, in such plasma is described by the Landau kinetic equation [4]:

$$\frac{df}{dt} = -2\pi n r_0^2 c^4 L_c \frac{\partial}{\partial v_i} \int \left(f \frac{\partial f'}{\partial v_j'} - f' \frac{\partial f}{\partial v_j} \right) \omega_{ij} d^3 v', \tag{6.18}$$

where

$$\omega_{ij} = \frac{\left(\mathbf{v}-\mathbf{v}'\right)^2 \delta_{ij} - \left(v_i - v_i'\right)\left(v_j - v_j'\right)}{\left|\mathbf{v}-\mathbf{v}'\right|^3}, \tag{6.19}$$

$$\int f(\mathbf{v}) d^3 v = 1, \tag{6.20}$$

r_0 is the particle classical radius, n is the plasma density, c is the speed of light, $L_c = \ln(\rho_{max}/\rho_{min})$ is the Coulomb logarithm,

$$\begin{aligned} \rho_{min} &= r_0 c^2/\overline{v^2}, \\ \rho_{max} &= \sqrt{\overline{v^2}/4\pi n r_0 c^2}, \end{aligned} \qquad \overline{v^2} = \sigma_{vx}^2 + \sigma_{vy}^2 + \sigma_{vz}^2, \tag{6.21}$$

and $\sigma_{vi} \equiv \sqrt{\overline{v_i^2}}, i = (x, y, z)$ are the rms velocity spreads. Equation (6.18) is obtained in the logarithmic approximation and is justified when $\ln(\rho_{max}/\rho_{min}) \gg 1$, where the plasma perturbation theory can be used. The Landau kinetic equation (6.18) is a nonlinear second-order integro-differential equation on the unknown function f, which is assumed to be nonnegative and integrable together with its moments up to order 2. The general time-dependent solution of this equation is not known. However, one can verify by inspection that the stationary solution of Eq. (6.18) is any Maxwellian velocity distribution function. It can be also easily checked that the following quantities are conserved:

$$\int f\, d^3 v, \int f v d^3 v, \text{and } \frac{1}{2}\int f |v|^2 d^3 v, \tag{6.22}$$

corresponding respectively to the spatial density, momentum, and kinetic energy of plasma. The symmetric form of Eq. (6.18) can be easily rewritten in a Fokker–Planck form:

$$\frac{df}{dt} = -\frac{\partial}{\partial v_i}(F_i f) + \frac{1}{2}\frac{\partial}{\partial v_i}\left(D_{ij}\frac{\partial f}{\partial v_j}\right), \tag{6.23}$$

where

$$\begin{aligned} F_i(v) &= -4\pi n r_0^2 c^4 L_c \int f\left(v'\right)\frac{u_i}{|\mathbf{u}|^3} d^3 v', \\ D_{ij} &= 4\pi n r_0^2 c^4 L_c \int f\left(v'\right)\frac{u^2\delta_{ij} - u_i u_j}{|\mathbf{u}|^3} d^3 v', \\ \mathbf{u} &= \mathbf{v} - \mathbf{v}', \end{aligned} \tag{6.24}$$

thus demonstrating that the Landau kinetic equation includes both the dynamic friction and the diffusion.

Let us assume a general Gaussian velocity distribution. By appropriate rotation of coordinate frame it can be reduced to the three-temperature distribution function

$$f = \frac{1}{(2\pi)^{3/2}\sigma_{vx}\sigma_{vy}\sigma_{vz}} \exp\left(-\frac{1}{2}\left(\frac{v_x^2}{\sigma_{vx}^2}+\frac{v_y^2}{\sigma_{vy}^2}+\frac{v_z^2}{\sigma_{vz}^2}\right)\right). \tag{6.25}$$

Then let us calculate the growth rate for the second moments of the distribution function

$$\Sigma_{ij} = \int f v_i v_j d^3 v. \tag{6.26}$$

First, it is clear from symmetry of Eq. (6.25) that only the diagonal elements of $\boldsymbol{\Sigma}$ are nonzero, $\boldsymbol{\Sigma} = \mathrm{diag}(\sigma_{vx}^2, \sigma_{vy}^2, \sigma_{vz}^2)$. Second, using Eq. (6.18) we can find the rate of change of these second order moments due to Coulomb scattering in plasma

$$\frac{d}{dt}\Sigma_{ij} = \int \frac{\partial f}{\partial t} v_i v_j d^3 v. \tag{6.27}$$

The result describes the rate of energy exchange between degrees of freedom in plasma:

$$\frac{d\boldsymbol{\Sigma}}{dt} = \frac{(2\pi)^{3/2} n {r_0}^2 c^4 L_c}{\sqrt{\sigma_{vx}^2+\sigma_{vy}^2+\sigma_{vz}^2}} \begin{pmatrix} \Psi(\sigma_{vx},\sigma_{vy},\sigma_{vz}) & 0 & 0 \\ 0 & \Psi(\sigma_{vy},\sigma_{vz},\sigma_{vx}) & 0 \\ 0 & 0 & \Psi(\sigma_{vz},\sigma_{vx},\sigma_{vy}) \end{pmatrix}. \tag{6.28}$$

The function $\Psi(x,y,z)$ can be expressed [7] through the symmetric elliptic integral of the second kind, $R_D(x,y,z)$, so that:

$$\Psi(x,y,z) = \frac{\sqrt{2}r}{3\pi}\left(y^2 R_D\left(z^2,x^2,y^2\right) + z^2 R_D\left(x^2,y^2,z^2\right) - 2x^2 R_D\left(y^2,z^2,x^2\right)\right), \tag{6.29}$$

$$R_D(u,v,w) = \frac{3}{2}\int_0^\infty \frac{dt}{\sqrt{(t+u)(t+v)(t+w)^3}} \tag{6.30}$$

where $r = \sqrt{x^2+y^2+z^2}$; $x,y,z \geq 0$. An algorithm for fast numerical evaluation of $R_D(u,v,w)$ is discussed in [7]. The function $\Psi(x,y,z)$ is chosen such that it depends on the ratios of its variables but not on r. It is symmetric with respect to the variables y and z, and is normalized such that $\Psi(0,1,1) = 1$. The energy conservation yields: $\Psi(1,0,1) = \Psi(1,1,0) = -\frac{1}{2}$ and $\Psi(x,y,z) + \Psi(y,z,x) + \Psi(z,x,y) = 0$. And in a thermal equilibrium, $\Psi(1,1,1) = 0$. In a case of two equal

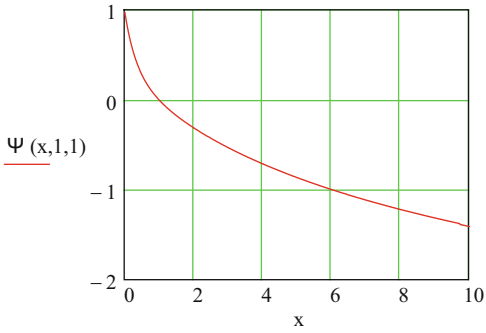

Fig. 6.1 The function $\Psi(x, 1, 1)$ for two equal temperatures

temperatures, the temperature relaxation rate given by (6.28) is identical to that given in [8] and can be expressed in terms of elementary functions:

$$\Psi(x, y, y) = \frac{\sqrt{2}\sqrt{x^2 + 2y^2}}{\pi y^2}\left(F\left(x^2, y^2\right)\left[y^2 + 2x^2\right] - 2x\right), \tag{6.31}$$

where

$$F(u, v) = \begin{cases} \dfrac{1}{\sqrt{(v-u)^3}}\left(v\mathrm{acos}\left(\sqrt{\dfrac{u}{v}}\right) - \sqrt{u}\sqrt{v-u}\right), & u < v, \\ \dfrac{2}{3\sqrt{v}}, & u = v, \\ -\dfrac{1}{\sqrt{(u-v)^3}}\left(v\mathrm{acosh}\left(\sqrt{\dfrac{u}{v}}\right) - \sqrt{u}\sqrt{u-v}\right), & u > v. \end{cases} \tag{6.32}$$

Figure 6.1 shows the function $\Psi(x, 1, 1)$ for x from 0 to 10. If one of the temperatures is zero, a very useful approximation (with a ~0.5 % accuracy) was obtained in [9]:

$$\Psi(0, x, y) \approx 1 + \frac{\sqrt{2}}{\pi}\ln\left(\frac{x^2 + y^2}{2xy}\right) - 0.055\left(\frac{x^2 - y^2}{x^2 + y^2}\right)^2. \tag{6.33}$$

Note that Eq. (6.28) is not self-consistent; i.e., it implies that the distribution function remains Gaussian; however, the diffusion and the friction due to multiple scattering does not allow for the beam distribution to remain Gaussian during the process of temperature exchange until it reaches the thermal equilibrium and the distribution becomes Maxwellian. Additionally, the single large-angle scattering (not considered in this section) creates non-Gaussian tails. However deviations from the Gaussian distribution are comparatively small and Eq. (6.28) represents a good approximation in most practical cases. In particular, it describes well the temperature relaxation in the course of electron beam transport on the case of non-magnetized electron cooling.

Multiple Scattering (IBS) in Accelerators

Although the beam focusing and dispersion effects in accelerators significantly complicate computation of IBS, they do not change the essence of the process. However, the time-dependent nature of transverse focusing results in a continuous growth of the 6-D beam emittance [2, 3]. In difference to plasma where the energy is conserved the binary collisions do not conserve energy in the beam frame resulting in unlimited emittance growth supported by energy transfer from the longitudinal beam motion (with nearly infinite reservoir of energy) to the internal particle motion in the beam frame (BF). The calculations of the IBS rates in accelerators will proceed in the following manner. First, one can verify that for the typical parameters at the Tevatron complex, the beam velocity spread in the BF is far from being relativistic[2] and the particle collision time, $\rho_{\max}/v$, is much smaller than the period of betatron oscillations in the BF. This implies that the results of the previous section can be used in each location and then averaged over the entire length of the accelerator to obtain the overall IBS rates. Second, we will make an assumption that at each location of the accelerator the distribution function, $f(\mathbf{v}, \mathbf{r}, t)$, in the BF, is Gaussian in the 6D phase space. Third, we will calculate the growth rates in the BF using Eq. (6.28). And finally, we will convert these rates into the laboratory frame (LF) emittance growth rates.

Generalizing the Landau kinetic equation [see Eq. (6.23)] for a spatially non-homogeneous distribution function in the BF one obtains:

$$\frac{df}{dt} = -2\pi N r_0^2 c^4 L_c \frac{\partial}{\partial v_i} \int \left(f \frac{\partial f'}{\partial v_j'} - f' \frac{\partial f}{\partial v_j} \right) \omega_{ij} d^3v' d^3r' \delta\left(\vec{r} - \vec{r}' \right), \tag{6.34}$$

where N is the number of particles per bunch, the distribution function is normalized to 1

$$\int f(\mathbf{v}, \mathbf{r}, t) d^3v d^3r = 1, \tag{6.35}$$

and we assume that in the absence of collisions the beam is in the equilibrium state, i.e., $\partial f/\partial t = 0$. The same as above we choose the initial distribution being Gaussian:

$$f(\mathbf{v}, \mathbf{r}) = \frac{\sqrt{|\Xi|}}{8\pi^3} \exp\left(-\mathbf{X}^{\mathrm{T}} \Xi \mathbf{X}\right), \tag{6.36}$$

where $\mathbf{X}^{\mathrm{T}} = (x, v_x, y, v_y, z, v_z)$, and Ξ is a symmetric positively defined 6×6 matrix determined by ring Twiss parameters and mode emittances of the beam

[2] Actually this condition is satisfied for all circular accelerators build to this time with exception of LEP presenting a weakly relativistic case.

(see Chap. 2). By definition its determinant is the squared product of inversed mode emittances, $|\boldsymbol{\Xi}| \equiv \det(|\boldsymbol{\Xi}|) = 1/(\varepsilon_1\varepsilon_2\varepsilon_3)^2$.

Let us define the second moments of the distribution function (6.36) in the BF:

$$\begin{aligned}\Sigma_{ij} &= \int f(\mathbf{v},\mathbf{r}) v_i v_j d^3v d^3r,\\ K_{ij} &= \int f(\mathbf{v},\mathbf{r}) r_i v_j d^3v d^3r,\\ \Lambda_{ij} &= \int f(\mathbf{v},\mathbf{r}) r_i r_j d^3v d^3r.\end{aligned} \tag{6.37}$$

Similar to Eq. (6.27) let us find the rate of change of these moments by using the Landau kinetic equation (6.34) for the distribution function (6.36). Simple integration immediately yields[3]

$$\frac{d\mathbf{K}}{dt} = \frac{d\boldsymbol{\Lambda}}{dt} = 0. \tag{6.38}$$

To calculate the rate for elements of matrix $\boldsymbol{\Sigma}$ we will introduce the rotation matrix $\mathbf{T}$, reducing $\boldsymbol{\Sigma}$ to its diagonal form

$$\mathbf{T}^{\mathrm{T}}\boldsymbol{\Sigma}\mathbf{T} = \begin{pmatrix} \sigma_1^2 & 0 & 0\\ 0 & \sigma_2^2 & 0\\ 0 & 0 & \sigma_3^2 \end{pmatrix}, \tag{6.39}$$

and the matrix function $\boldsymbol{\Psi}_{\mathrm{IBS}}(\mathbf{T}^{\mathrm{T}}\boldsymbol{\Sigma}\mathbf{T})$ such that

$$\boldsymbol{\Psi}_{\mathrm{IBS}}\left(\mathbf{T}^{\mathrm{T}}\boldsymbol{\Sigma}\mathbf{T}\right) = \begin{pmatrix} \Psi(\sigma_1,\sigma_2,\sigma_3) & 0 & 0\\ 0 & \Psi(\sigma_2,\sigma_3,\sigma_1) & 0\\ 0 & 0 & \Psi(\sigma_3,\sigma_1,\sigma_2) \end{pmatrix}, \tag{6.40}$$

with $\Psi(x,y,z)$ given by Eq. (6.29).

Similar to Eq. (6.28) one can now calculate the rate for matrix $\boldsymbol{\Sigma}$ due to the IBS in the beam frame in the absence of betatron and synchrotron oscillations:

$$\frac{d\boldsymbol{\Sigma}}{dt} = \frac{Nr_0{}^2c^4L_{\mathrm{c}}}{4\sqrt{2}a_1a_2a_3\sqrt{\mathrm{Tr}(\boldsymbol{\Sigma})}}\mathbf{T}\boldsymbol{\Psi}_{\mathrm{IBS}}\left(\mathbf{T}^{\mathrm{T}}\boldsymbol{\Sigma}\mathbf{T}\right)\mathbf{T}^{\mathrm{T}}, \tag{6.41}$$

where a_1a_2 and a_3 are the rms sizes of 3D bunch ellipsoid (principle rms beam dimensions). We will now convert this rate to the laboratory frame and calculate the

[3] Note that at this point we consider only variations of f related to the scattering. Effects of betatron motion will be accounted at the next stage of calculations.

emittance growth rates. For accelerators with linear optics, the bunch distribution (6.36) is defined in the LF as:

$$F(\mathbf{r},\boldsymbol{\theta}) = \frac{1}{(2\pi)^3\varepsilon_1\varepsilon_2\varepsilon_3}\exp\left(-\frac{I_1}{\varepsilon_1}-\frac{I_2}{\varepsilon_2}-\frac{I_3}{\varepsilon_3}\right), \tag{6.42}$$

where $\mathbf{r}$ and $\boldsymbol{\theta}$ are the LF canonical coordinates and momenta, I_k are the particle's action variables, and ε_k are the mode emittances of the beam. The mode emittances are defined such that:

$$\varepsilon_k = \int I_k F(\mathbf{r},\boldsymbol{\theta}) d^3\theta d^3 r. \tag{6.43}$$

For a given particle the action variables are bi-linear forms of coordinates and momenta:

$$I_k = B^k_{ij}\theta_i\theta_j + C^k_{ij}\theta_i r_j + Q^k_{ij} r_i r_j, \tag{6.44}$$

where $\mathbf{B}$, $\mathbf{C}$, and $\mathbf{Q}$ are real 3×3 matrices, defined by the accelerator lattice at each location, and summation on the repeated subscripts is implied. It is obvious that (6.36) implies,

$$-\ln(F) = \sum_k \frac{I_k}{\varepsilon_k} = \frac{1}{2}\Theta_{ij}\theta_i\theta_j + \frac{1}{2}H_{ij}\theta_i r_j + \frac{1}{2}M_{ij} r_i r_j, \tag{6.45}$$

where $\boldsymbol{\Theta}$, H, and $\mathbf{M}$ are real 3×3 matrices, uniquely defined by the lattice at each accelerator location and related to BF matrices (6.37). We can now calculate the emittance growth rates as

$$\frac{d\varepsilon_k}{dt} = \left\langle \int I_k \frac{dF}{dt} d^3\theta d^3 r \right\rangle_s, \tag{6.46}$$

where $\langle\rangle_s$ implies averaging over the accelerator circumference. Using (6.40) and (6.41) we obtain

$$\frac{d\varepsilon_k}{dt} = \frac{N r_0^2 c^2}{4\sqrt{2}\beta^2\gamma^4}\left\langle \frac{L_c \sum_{i,j=1}^{3} B^k_{ij} R_{ij}}{a_1 a_2 a_3 \sqrt{\mathrm{Tr}(\boldsymbol{\Sigma})}} \right\rangle_s, \tag{6.47}$$

where β and γ are the usual relativistic Lorentz factors of the bunch in the lab frame, a_i are the principle rms bunch sizes in the laboratory frame, and the 3×3 matrix $\mathbf{R}$ is given by the following expression:

$$\mathbf{R} = \left(\mathbf{G}^{-1}\right)^{\mathrm{T}} \mathbf{T}\boldsymbol{\Psi}_{\mathrm{IBS}}\left(\mathbf{T}^{\mathrm{T}}\boldsymbol{\Sigma}\mathbf{T}\right)\mathbf{T}^{\mathrm{T}}\mathbf{G}^{-1}. \tag{6.48}$$

The BF matrix $\boldsymbol{\Sigma}$ is related to the LF matrix $\boldsymbol{\Theta}$ as follows:

$$\boldsymbol{\Sigma} = (\beta\gamma c)^2 \mathbf{G}^{\mathrm{T}} \boldsymbol{\Theta}^{-1} \mathbf{G}, \tag{6.49}$$

where $\mathbf{G} = \mathrm{diag}(1, 1, 1/\gamma)$. Equation (6.47) is the most general IBS emittance growth rate for an arbitrary Gaussian 6D distribution function in a linear accelerator lattice.

Let us now discuss several specific cases. As a first example consider an accelerator lattice with uncoupled $x - y$ betatron motion. However we will account that both dispersions can be nonzero. Then,

$$\boldsymbol{\Theta} = \begin{pmatrix} \beta_x/\varepsilon_x & 0 & -\beta_x\Phi_x/\varepsilon_x \\ 0 & \beta_y/\varepsilon_y & -\beta_y\Phi_y/\varepsilon_y \\ -\beta_x\Phi_x/\varepsilon_x & -\beta_y\Phi_y/\varepsilon_y & \Theta_{33} \end{pmatrix}, \tag{6.50}$$

where $\Theta_{33} = {\sigma_p}^{-2} + \frac{A_x}{\varepsilon_x} + \frac{A_y}{\varepsilon_y}$, $\Phi_x = D_x^{'} + \frac{\alpha_x D_x}{\beta_x}$, $\Phi_y = D_y^{'} + \frac{\alpha_y D_y}{\beta_y}$, $A_x = \frac{1}{\beta_x}\left({D_x}^2 + (\beta_x\Phi_x)^2\right)$, $A_y = \frac{1}{\beta_y}\left({D_y}^2 + (\beta_y\Phi_y)^2\right)$; $F_D = 1 + \frac{{D_x}^2{\sigma_p}^2}{\varepsilon_x\beta_x} + \frac{{D_y}^2{\sigma_p}^2}{\varepsilon_y\beta_y}$;

β_x, β_y, α_x, and α_y, are the beta-functions and their negative half derivatives; D_x, D_y, $D_x^{'}$, and $D_y^{'}$ are the dispersions and their derivatives; ε_x, ε_y and $\varepsilon_z = \sigma_z\sigma_p$ are the non-normalized transverse and longitudinal rms beam emittances; σ_z is the rms bunch length and σ_p is the relative rms momentum spread. In this case the Eq. (6.47) becomes:

$$\frac{d\varepsilon_k}{dt} = \frac{N{r_0}^2c^2}{4\sqrt{2}\sigma_z\beta^2\gamma^4\sqrt{\varepsilon_x\varepsilon_y}} \left\langle \frac{L_c \sum_{i,j=1}^{3} \mathbf{B}_{ij}^k \mathbf{R}_{ij}}{\sqrt{\beta_x\beta_y F_D \mathrm{Tr}(\boldsymbol{\Sigma})}} \right\rangle_s, \tag{6.51}$$

with

$$\mathbf{B}^x = \begin{pmatrix} \beta_x & 0 & -\Phi_x\beta_x \\ 0 & 0 & 0 \\ -\Phi_x\beta_x & 0 & A_x \end{pmatrix}, \mathbf{B}^y = \begin{pmatrix} 0 & 0 & 0 \\ 0 & \beta_y & -\Phi_y\beta_y \\ 0 & -\Phi_y\beta_y & A_y \end{pmatrix}, \\ \mathbf{B}^z = \begin{pmatrix} 0 & 0 & 0 \\ 0 & 0 & 0 \\ 0 & 0 & \beta_z \end{pmatrix}, \tag{6.52}$$

where $\beta_z = \sigma_z/\sigma_p$. The Coulomb logarithm is computed similar to the plasma case with the following correction affecting the value of maximum impact parameter in Eq. (6.21):

$$\rho_{\max} = \min\left(\sigma_{\min}, \gamma\sigma_z, \sqrt{\frac{\mathrm{Tr}(\boldsymbol{\Sigma})}{4\pi n r_0 c^2}}\right), \tag{6.53}$$

where $2\sigma_{\min}{}^2 = \sigma_x{}^2 + \sigma_y{}^2 - \sqrt{\left(\sigma_x{}^2 - \sigma_y{}^2\right)^2 + 4D_x{}^2D_y{}^2\sigma_p{}^4}$, $\sigma_x{}^2 = \varepsilon_x\beta_x + D_x{}^2\sigma_p{}^2$, and $\sigma_y{}^2 = \varepsilon_y\beta_y + D_y{}^2\sigma_p{}^2$. If one of the dispersions is equal to zero, then $\sigma_{\min} = \min(\sigma_x, \sigma_y)$.

The above equations can be used for a coasting beam with following substitutions: $\sigma_z \to L/(2\sqrt{\pi})$, $\mathbf{B}_z = \mathrm{diag}(0, 0, 2)$ implying that $d\varepsilon_3/dt \to d\overline{\sigma_p{}^2}/dt$. Note that the factor of 2 in matrix $\mathbf{B}_z$ reflects the absence of the synchrotron motion, taken into account in Eq. (6.51).

In many practical applications the longitudinal temperature in the BF is much smaller than the transverse one ($\theta_{\parallel}/\gamma \ll \theta_{\perp}$) and the vertical dispersion can be neglected. The Eq. (6.51) (bunched beam) then can be reduced to the following:

$$\frac{d}{dt}\begin{pmatrix}\varepsilon_x\\ \varepsilon_y\\ \sigma_p{}^2\end{pmatrix} = \frac{Nr_0{}^2c}{4\sqrt{2}\beta^3\gamma^3\sigma_z}\left\langle \frac{L_c}{\sigma_x\sigma_y\theta_{\perp}}\begin{pmatrix}\Psi_x(\theta_x,\theta_y)\\ \Psi_y(\theta_x,\theta_y)\\ \Psi(0,\theta_x,\theta_y)\end{pmatrix}\right\rangle_s, \tag{6.54}$$

where $\Psi_y(\theta_y,\theta_x) = \Psi(\theta_y,\theta_x,0)\beta_y/\gamma^2$, $\Psi_x(\theta_x,\theta_y) = \Psi(0,\theta_x,\theta_y)A_x + \Psi(\theta_x,\theta_y,0)\beta_x/\gamma^2$, $\theta_{\perp} = \sqrt{\theta_x{}^2 + \theta_y{}^2}$, $\theta_x{}^2 = \varepsilon_x/\beta_x(1 + \sigma_p{}^2(\Phi_x\beta_x)^2/\sigma_x{}^2)$, $\theta_y{}^2 = \varepsilon_y/\beta_y$. For an ultra-relativistic machine, $\gamma \gg Q_x$, the terms with $\beta_{x,y}/\gamma^2$ are small and can be neglected.

Similar to the suppression of IBS in an electron beam by magnetic field the multiple IBS is suppressed if σ_p becomes so small that the collision time becomes comparable to the betatron frequency [10]. Such conditions can be achieved in the case of deep beam cooling.

6.1.3 Single and Multiple Scattering at the Residual Gas

It was already mentioned in the previous section that the Coulomb scattering creates non-Gaussian tails. In this section we will consider how Coulomb scattering can be treated so that both single and multiple scattering are correctly accounted. The diffusion coefficient for particle scattering in the medium is well known. For scattering in a ring it can be expressed in the following form:

$$D = 4\pi c\beta\left(\frac{r_0}{\gamma\beta^2}\right)^2\sum_i Z_i(Z_i+1)L_c^i\oint n_i(s)\beta_x(s)\frac{ds}{L}, \tag{6.55}$$

where the summing is performed over partial densities of residual gas, Z_i is their charges, and the integration over ring circumference averages the gas density, $n_i(s)$, weighted by the horizontal beta-function, β_x(s). For simplicity of equation we are considering an evolution of particle distribution in the horizontal plane. The same expressions are applicable to the vertical plane. For the high energy scattering ($\beta > \alpha_{FS}Z_i$, $\alpha_{FS} \approx 1/137$) the Coulomb logarithm is:

$$L_c^i = \ln\left(\frac{\theta_{\max}^i}{\theta_{\min}^i}\right), \theta_{\min}^i \approx \alpha_{FS} {Z_i}^{1/3} \frac{m_e c}{p}, \theta_{\max}^i \approx \min\left(\frac{274}{{A_i}^{1/3}} \frac{m_e c}{p}, \theta_b\right), \tag{6.56}$$

where p is the particles momentum and the minimum and maximum angles are determined by the field screening due to atomic electrons and by the diffraction on nuclei.

The solutions of Eq. (6.5) with diffusion of Eq. (6.55) are commonly used to describe the emittance growth in particle accelerators due to various random diffusion processes, including multiple elastic Coulomb scattering. This equation describes the core of the beam distribution well, but completely fails to describe its tails in the case of Coulomb scattering. Far-away tails can be sufficiently well estimated using a single scattering approximation, but in many applications a prediction of tails behavior in the vicinity of the core is required. It is possible to computer-model the distribution function by Monte Carlo methods. However, we found it beneficial to advance the analytical treatment of the Coulomb scattering process to a point, where, for a given residual gas pressure, the distribution function can be obtained by solving an integro-differential equation, proposed below. In what follows we consider Coulomb scattering on the residual gas, but the theory can be easily adapted to other Coulomb scattering phenomena.

To simplify formulas we omit the summation over different gas species below. Neglecting the nuclear form-factor, one can write the differential elastic small angle cross section in the following form [11]:

$$\frac{d\sigma}{d\Omega} \approx 4Z(Z+1)\left(\frac{r_0}{\gamma\beta^2}\right)^2 \frac{1}{\left(\theta_x^2 + \theta_y^2 + \theta_{\min}^2\right)^2}, \tag{6.57}$$

After integrating this over θ_y one obtains the one-dimensional cross section

$$\frac{d\sigma}{d\theta_x} \approx 2\pi Z(Z+1)\left(\frac{r_0}{\gamma\beta^2}\right)^2 \frac{1}{\left(\theta_x^2 + \theta_{\min}^2\right)^{3/2}} \tag{6.58}$$

and the total cross section

$$\sigma_{\text{tot}} \approx \frac{4\pi Z^2}{\theta_{\min}^2}\left(\frac{r_0}{\gamma\beta^2}\right)^2. \tag{6.59}$$

For a combined treatment of both the small- and large-angle elastic scattering let us write the right-hand side of Eq. (6.5) in a general form of the collision integral [3]:

$$\frac{\partial f}{\partial t} - \lambda \frac{\partial (If)}{\partial I} = \left\langle \int_{-\infty}^{\infty} \left(\left. \frac{d\sigma}{d\theta_x} \right|_{(\theta - \theta')} - \sigma_{\text{tot}} \delta\left(\theta - \theta'\right) \right) n v_o f \delta\left(x - x'\right) d\theta' dx' \right\rangle_{\psi, s}$$

$$= \left\langle \int_{-\infty}^{\infty} \left(2\pi Z(Z+1) \left(\frac{r_0}{\gamma \beta^2} \right)^2 \frac{1}{\left(\left(\theta_x - \theta_x'\right) + \theta_{\min}^2 \right)^{3/2}} - \sigma_{\text{tot}}, \delta\left(\theta - \theta'\right) \right) \right.$$

$$\left. n v_o f \delta\left(x - x'\right) d\theta' dx' \right\rangle_{\psi, s}, \tag{6.60}$$

where $\delta(\ldots)$ is the Dirac delta-function, and averaging is performed over the betatron phase, ψ, and machine circumference. Expressing particle angles and coordinates through the action-phase variables, (I, ψ), one obtains

$$\frac{\partial f}{\partial t} - \lambda \frac{\partial}{\partial I} (If) = \int_0^{I_b} W\left(I, I'\right) f\left(I', t\right) dI', \quad I < I_b, \tag{6.61}$$

where I_b is the ring acceptance, and we introduced a scattering kernel, $W(I, I')$,

$$W\left(I, I'\right) = n v_o \left\langle \int_{-\infty}^{\infty} \left(\left. \frac{d\sigma}{d\theta_x} \right|_{(\theta - \theta')} - \sigma_{\text{tot}} \delta\left(\theta - \theta'\right) \right) \delta\left(x - x'\right) d\varphi' \frac{d\varphi}{2\pi} \right\rangle_s. \tag{6.62}$$

Neglecting $\theta_{\min}$ in the cross section (6.58), denoting

$$B = 4\pi v_0 \left(\frac{r_p}{\gamma_0 \beta_0^2} \right)^2 Z(Z+1) \oint n(s) \beta(s) \frac{ds}{L}, \tag{6.63}$$

and temporally omitting the term with $\sigma_{\text{tot}} \delta(\theta - \theta')$ one obtains

$$W\left(I, I'\right) = \frac{B}{16\pi} \int_0^{2\pi} d\varphi \int_0^{2\pi} d\varphi' \frac{\delta\left(\sqrt{I} \cos\varphi - \sqrt{I'} \cos\varphi'\right)}{\left| \sqrt{I} \sin\varphi - \sqrt{I'} \sin\varphi' \right|^3}. \tag{6.64}$$

A lengthy integration yields[4]

[4] Method of the integration can be found below in the computation of similar integral for intra-beam scattering [see details further down Eq. (6.80)]. Note also that the Kernel (6.66) can be used without δ-function [like in Eq. (6.65)] in alternative form of integro-differential equation: $\partial f / \partial t - \lambda \partial (If) / \partial I = \int_0^{I_b} W\left(I, I'\right) \left(f\left(I', t\right) - f(I, t) \right) dI'$.

$$W\left(I,I^{'}\right)=\frac{B}{4}\frac{I+I^{'}}{\left|I-I^{'}\right|^{3}}\quad . \tag{6.65}$$

Neglecting $\theta_{\min}$ in our transition from Eq. (6.60) to Eq. (6.64) causes divergence of the integral (6.65) at $I\approx I'$, when the scattering angle is small. Instead of performing the exact integration using Eq. (6.58) (which is already an approximation), one can eliminate this divergence by modifying the kernel of Eq. (6.65) similar to the method used to limit the divergence in Eq. (6.57). Combining Eqs. (6.60) and (6.65) one obtains the kernel:

$$W\left(I,I^{'}\right)=\frac{B}{4}\left(\frac{I+I^{'}+I_{\min}/2}{\left(\left(I-I^{'}\right)^{2}+\left(I+I^{'}\right)I_{\min}+I_{\min}^{2}/4\right)^{3/2}}-\frac{2}{I_{\min}}\delta\left(I-I^{'}\right)\right), \tag{6.66}$$

where to find the coefficient in front of δ-function we used the law of particle conservation which requires that

$$\int_{0}^{\infty}W\left(I,I^{'}\right)dI^{'}=0. \tag{6.67}$$

The divergence in Eq. (6.65) was eliminated artificially by adding terms containing $I_{\min}$ in a manner similar to $\theta_{\min}$ in Eq. (6.57). Thus, although the new kernel (6.66) is not exact, it, however, has the correct asymptotic. It is symmetric with respect to I and I' as it can be seen from its definition (6.64). At small scattering angles it has the accuracy similar to Eq. (6.5) but it correctly accounts for single and multiple scatterings. Note that the form of the kernel, $W(I,I')$, assumes that the range of beam particle angles is smaller than the maximum scattering angle $\theta_{\max}$, which is well justified in most practical cases. Otherwise $\theta_{\max}$ has to be explicitly taken into account in Eq. (6.57).

The accelerator aperture is always finite. Therefore, the upper limit in the integral of Eq. (6.65) should be replaced with the boundary action value, I_b. This also yields the boundary condition for the distribution function, $f(I_b,t)=0$.

It is now quite trivial to obtain a Fokker–Planck equation from Eq. (6.61) by expanding the function f in series at $I'=I$, $f\left(I^{'},t\right)\approx f(I,t)+f^{'}(I,t)\left(I^{'}-I\right)+\frac{1}{2}f^{''}(I,t)\left(I^{'}-I\right)^{2}$, and integrating to $I_b=\overline{\beta}\theta_{\max}^{2}$, where $\overline{\beta}$ is the average ring beta-function. The integration yields:

$$\frac{\partial f}{\partial t}-\lambda\frac{\partial}{\partial I}(If)\approx\frac{B}{4}\ln\left(\frac{I_{\max}}{I_{\min}}\right)\frac{\partial}{\partial I}\left[I\frac{\partial f}{\partial I}\right]. \tag{6.68}$$

Recalling that $\ln(I_{\max}/I_{\min})=2L_{\mathrm{c}}$ we arrive to Eq. (6.5) with diffusion of Eq. (6.55).

Normally the difference between the maximum and minimum impact parameters is many orders of magnitude. It makes it impossible to solve Eq. (6.61) directly. However considered above diffusion model allows one to create an effective numerical algorithm which solves for the distribution function evolution under single and multiple scattering. For a numerical solution we split the total range of the action variable, $[0, I_b]$, into N equal size cells, $\Delta I = I_b/N$. Then, Eq. (6.61) can be rewritten as

$$\delta f_n = \frac{\delta t}{\Delta I}\left(\lambda \frac{f_{n+1} I_{n+1} - f_{n-1} I_{n-1}}{2} + \sum_{m=0}^{N-1} \widetilde{W}(n,m) f_m\right), \quad I_n = n\Delta I. \tag{6.69}$$

Taking into account that the cell size is much larger than the minimum action, $I_{\min}$, we can write the probability of a particle exchange for two distant cells

$$\widetilde{W}(n,m) = \frac{B}{4}\frac{n+m}{|n-m|^3}, \quad n \neq m, \;\; m \pm 1. \tag{6.70}$$

To find the probability of the particle exchange for nearby cells we use diffusion equation. It yields:

$$\widetilde{W}(n, n \pm 1) = \frac{BL_c}{2}\left(n \pm \frac{1}{2}\right). \tag{6.71}$$

The probability $\widetilde{W}(n,n)$ is determined by the particle conservation so that

$$\sum_{m=0}^{\infty} \widetilde{W}(n,m) = 0 \;\; . \tag{6.72}$$

The index m in this sum is running to infinity. It takes into account that a particle can be scattered outside of the accelerator aperture. Consequently, the particle number is not conserved in a finite aperture of a ring.

6.1.4 Single and Multiple Scattering for Longitudinal Degree of Freedom in Hadron Colliders

The single IBS scattering becomes important when there is a large difference between rms velocities of different degrees of freedom in the BF. In this case a single scattering can result in a momentum transfer significantly exceeding the rms value of the coldest degree of freedom thus creating non-Gaussian tails and particle loss. In ultra-relativistic colliders and storage rings the longitudinal momentum spread in the beam frame, $\Delta p'_{||} = \Delta p_{||}/\gamma$, is much smaller than the transverse one.

In this case a single scattering with large momentum transfer can result in that both particles scatter out of longitudinal machine acceptance. For the case when the longitudinal temperature is much smaller than the transverse one it is called the Touschek effect. It was first investigated in electron storage rings for a flat beam and non-relativistic energies in the BF [12, 13]. The radiation damping in electron synchrotrons typically results in the rms momentum spread being much smaller than the RF bucket height. That allows one to consider single and multiple scattering separately resulting in a simple treatment of the single IBS developed in [13]. However this approximation is usually not valid in hadron colliders where initially the beam is usually well inside of the RF bucket and the beam loss is dominated by single scattering; but shortly later, the multiple scattering results in the beam distribution reaching the RF bucket boundary leading to domination of multiple scattering in the particle loss.

As it was already pointed out the considered above model of IBS assumes that the beam stays Gaussian in the course of its distribution evolution and the focusing is linear. These conditions are satisfied sufficiently well for transverse degrees of freedom. However such approximation is quite coarse for the longitudinal degree of freedom if the bunch length is comparable to the RF bucket length. In further consideration we assume that the longitudinal momentum spread in the BF is much smaller than the transverse one ($\sigma_p/\gamma \ll \theta_\perp$); that the transverse distributions are Gaussian and do not depend on the longitudinal action; and we also take into account that the longitudinal motion is nonlinear and is described by dimensionless Hamiltonian:

$$H = \frac{\hat{p}^2}{2} + U(\phi) \xrightarrow[\text{harmonic RF}]{\text{Single}} \frac{\hat{p}^2}{2} + 2\Omega_s{}^2 \left(\sin \frac{\phi}{2} \right)^2, \tag{6.73}$$

where Ω_s is the small amplitude synchrotron frequency.

In the case when multiple scattering is only accounted the evolution of longitudinal distribution and the particle loss from the RF bucket can be described by Eq. (6.2) with $\lambda = 0$:

$$\frac{\partial f}{\partial t} = \frac{1}{2} \frac{\partial}{\partial I} \left(\frac{D_{||}(I)}{\omega(I)} I \frac{\partial f}{\partial I} \right). \tag{6.74}$$

Here in comparison to Eq. (6.2) we redefined diffusion coefficient so that $D_{||}(\omega) = \omega(0) D(\omega)$. It simplifies formulas and looks more natural for description of diffusion in the longitudinal motion. To find $D_{||}(\omega)$ we will follow the following procedure. As one can see from Eq. (6.73) a momentum change $\delta\hat{p}$ results in an energy change: $\delta H = \hat{p}\, \delta\hat{p}$. Taking into account that $dH = \omega(I)\, dI$ we obtain:

$$\frac{d}{dt} \overline{\delta I^2} = \left\langle \frac{\hat{p}^2}{\omega(I)^2} \frac{d}{dt} \overline{\delta \hat{p}^2} \right\rangle_\psi, \tag{6.75}$$

where $\langle \ldots \rangle_\psi$ denotes averaging over synchrotron phase. On the other hand, multiplying Eq. (6.74) by $(I' - I)^2$ and integrating it with $f(I) = \delta(I' - I)$ one obtains

$$\frac{d}{dt}\overline{\delta I^2} = \frac{1}{2}\int \left(I' - I\right)^2 \frac{\partial}{\partial I'}\left(\frac{D_{||}(I')}{\omega(I')} I' \frac{\partial f}{\partial I'}\right) dI' = \int \left(\frac{D_{||}(I')}{\omega(I')} I' + \left(I' - I\right)\frac{d}{dI'}\left(\frac{D_{||}(I')}{\omega(I')} I'\right)\right) f(I') dI' \xrightarrow{f(I') = \delta(I' - I)} \frac{D_{||}(I)}{\omega(I)} I. \tag{6.76}$$

Comparing Eqs. (6.75) and (6.76) one obtains

$$D_{||}(I) = \left\langle \frac{\hat{p}^2}{I\omega(I)} \frac{d}{dt}\overline{\delta \hat{p}^2} \right\rangle_\psi. \tag{6.77}$$

Using cross section of Eq. (6.57) and performing averaging one finally obtains[5]:

$$D_{||}(I) = \frac{\widetilde{A} L_c}{2\pi I \omega(I)} \oint \hat{p}^2 n(\phi) d\psi, \tag{6.78}$$

where we took into account that the local diffusion is proportional to the beam linear density $n(\phi) = \int f(I(\phi, \hat{p})) d\hat{p}$ normalized so that at the process beginning $\int_{-\pi}^{\pi} n(\phi) d\phi = 1$, the choice of parameter

$$\widetilde{A} = 4\pi^3 \sqrt{2\pi} \frac{N r_0^2 f_{RF}^3 \eta^2}{\beta^4 \gamma^3} \left\langle \frac{\Psi(0, \theta_x, \theta_y)}{\sigma_x \sigma_y \sqrt{\theta_x^2 + \theta_y^2}} \right\rangle_s, \tag{6.79}$$

will be clarified later in this section, f_{RF} is the RF frequency, η is the ring slip factor, and N is the initial particle number in the bunch. Substituting diffusion (6.78) into Eq. (6.6) (for $\lambda = 0$) and performing integration with linear RF and Gaussian distribution yield the momentum growth rate of Eq. (6.54).

[5] For rectangular distribution with total bunch length ϕ_{tot} ($n(\phi) = 1/\phi_{tot}$ within bunch) and linear RF one obtains $\oint \hat{p}^2 n(\phi) d\psi = 2\pi\omega I/\phi_{tot}$, and, consequently, $D_{||}(I) = \widetilde{A} L_c/\phi_{tot}$.

To take into account the single scattering one needs to replace the Fokker–Planck equation (6.74) by integro-differential equation[6] [14]:

$$\frac{\partial f(I,t)}{\partial t} = \int_0^{a_b} W\left(I,I'\right)\left(f\left(I',t\right) - f(I,t)\right)dI', \tag{6.80}$$

where a_b is the longitudinal acceptance determined by a finite value of the maximum momentum deviation or by RF bucket size. Further we will assume that the upper limit of the integral is equal to infinity but the boundary condition determines that $f(a) = 0$ for $a > a_b$. To proceed further we need to take into account that even strong single scattering which instantly moves a particle to the longitudinal bucket boundary implies a small angle scattering (in the BF) which differential cross section is proportional to $1/q^3$, where $\hat{q} = \hat{p} - \hat{p'}$ is the longitudinal momentum transfer. Integrating over longitudinal distribution and averaging over betatron motion one obtains:

$$\frac{\partial f(I,t)}{\partial t} = \frac{\widetilde{A}}{8\pi}\int_0^{\infty} n(\phi)\frac{f\left(I',t\right) - f(I,t)}{\left|\hat{p} - \hat{p}'\right|^3}\delta\left(\phi - \phi'\right)d\psi d\psi' dI'. \tag{6.81}$$

In difference to Eq. (6.60) the local diffusion (scattering) is position dependent, i.e., is proportional to the local density, $n(\phi)$. For now we also neglect the divergence in the integral at $\hat{p} = \hat{p}'$. This deficiency will be addressed later in a manner similar to the one used in the derivation of integro-differential equation (6.61) describing scattering on the residual gas. The parameter $\widetilde{A}$ used in Eq. (6.81) should be determined by averaging over transverse distributions and the ring circumference. As will be shown below that it is determined by Eq. (6.79). Comparing Eqs. (6.80) and (6.81) one can write for the kernel in the integral:

$$\begin{aligned} W\left(I,I'\right) &= \frac{\widetilde{A}}{8\pi}\int_{-\pi}^{\pi}\int_{-\pi}^{\pi} n(\phi)\frac{\delta\left(\phi - \phi'\right)}{\left|\hat{p} - \hat{p}'\right|^3}d\psi d\psi' = \frac{\widetilde{A}\omega\omega'}{8\pi}\oint\oint n(\phi)\frac{\delta\left(\phi - \phi'\right)}{\left|\hat{p} - \hat{p}'\right|^3}\frac{d\phi d\phi'}{\hat{p}\hat{p}'} \\ &= \widetilde{A}\frac{\omega\omega'}{4\pi}\int_{\max\left(a(I),a\left(I'\right)\right)}^{\min\left(b(I),b\left(I'\right)\right)} n(\phi)\left(\frac{1}{\left|\hat{p} - \hat{p}'\right|^3} + \frac{1}{\left|\hat{p} - \hat{p}'\right|^3}\right)\frac{d\phi}{\hat{p}\hat{p}'}. \end{aligned} \tag{6.82}$$

where $b(I)$ and $a(I)$ determine the range of motion ($\phi \in [a(I), b(I)]$), and we used that $d\psi = \omega d\phi/\hat{p}$. This equality can be obtained by making a ratio of two

[6] Here we choose alternative form of Eq. (6.61).

straightforward equations: $d\psi = \omega \quad dt$ and $d\phi = \hat{p}\, dt$. Substituting $\hat{p} = \sqrt{2H(I) - U(\phi)}$ and performing integration one obtains for $I' \geq I$:

$$W\left(I, I'\right) = \frac{\widetilde{A}\omega\omega'}{8\pi\left(H\left(I'\right) - H(I)\right)^3}\left[\left(H\left(I'\right) - H(I)\right)\int_{a(I)}^{b(I)} n(\phi)\frac{d\phi}{\hat{p}} + 2\int_{a(I)}^{b(I)} n(\phi)\hat{p}\, d\phi\right], \quad I' \geq I. \tag{6.83}$$

Taking into account that the kernel is a symmetric function, $W(I, I') = W(I', I)$, one obtains the kernel for $I \geq I'$. To remove divergence at $I = I'$ we follow the recipe of Eq. (6.66). That yields:

$$W\left(I, I'\right) = \widetilde{A}\omega\omega' \frac{\left(H\left(I'\right) - H(I)\right)\int_{a(I)}^{b(I)} n(\phi)\frac{d\phi}{\hat{p}} + 2\int_{a(I)}^{b(I)} n(\phi)\hat{p}\, d\phi}{8\pi\left(\left(H\left(I'\right) - H(I)\right)^2 + \left(H\left(I'\right) - H(I)\right)\Delta E_{\min} + {\Delta E_{\min}}^2/4\right)^{3/2}}, \quad I' \geq I. \tag{6.84}$$

To verify that the parameters $\widetilde{A}$ used in Eqs. (6.78) and (6.80) are equal we obtain the diffusion equation (6.74) from integro-differential (6.80). Expending distribution function into Tailor series one obtains:

$$\begin{aligned}\frac{\partial f(I,t)}{\partial t} \approx \int_{I_{\min}}^{I_{\max}} &\left(W\left(I, I + I'\right)\left(f'(I)I' + f''(I)\frac{I'^2}{2}\right)\right. \\ &\left. + W\left(I - I', I\right)\left(-f'(I)\Delta I + f''(I)\frac{I'^2}{2}\right)\right) dI',\end{aligned} \tag{6.85}$$

where the term with $f(I)$ is equal to zero and was omitted due to particle conservation [see Eq. (6.67)]. Changing the integration variable to $H = I\omega$, introducing functions

$$B(H) = \frac{1}{2}\int_{a(H)}^{b(H)} n(\phi)\frac{d\phi}{\hat{p}} = \frac{1}{4\omega}\oint n(\phi)d\psi \quad \text{and} \quad C(H) = \frac{1}{2}\int_{a(H)}^{b(H)} n(\phi)\hat{p}\, d\phi = \frac{1}{4\omega}\oint n(\phi)\hat{p}^2 d\psi,$$

and expending the kernel to Tailor series we obtain:

$$\frac{\partial f}{\partial t} \approx \frac{\widetilde{A}\omega}{4\pi}\int_{H_{\min}}^{H_{\max}} \left((hB(H)+C(H)) \left(f'_H(H)h + f''_H(H)\frac{h^2}{2} \right) \right.$$
$$\left. + \left(h\left(B(H) - B'_H(H)h\right) + C(H) - C'_H h\right) \left(-f'_H(H)h + f''_H(H)\frac{h^2}{2} \right) \right) \frac{dh}{h^3}$$
$$\approx \frac{\widetilde{A}\omega}{2\pi}\int_{H_{\min}}^{H_{\max}} \left(f'_H(H)C'_H + f''_H(H)C(H) \right)\frac{dh}{h} = \frac{\widetilde{A}\omega}{2\pi}\left(f'_H(H)C'_H + f''_H(H)C(H) \right)$$
$$\ln\left(\frac{H_{\max}}{H_{\min}}\right), \tag{6.86}$$

where $h = H(I') - H(I)$ and in the final two equalities we left only logarithmic terms. After simple transformations taking into account that $\ln(H_{\max}/H_{\min}) = 2L_c$ we obtain Eq. (6.74) with diffusion of Eq. (6.78).

In conclusion we note that to find an evolution of bunch population and rms emittances, Eq. (6.80) with kernel (6.84) has to be solved together with the equations describing the evolution of transverse emittances. For numerical solution one can adopt an algorithm considered above in Sect. 6.1.3.

6.2 Diffusion due to RF Noise

Another important mechanism instigating longitudinal emittance growth is related to noise in the RF system of a storage ring. In the absence of longitudinal cooling (which is normally the case for hadron colliders) this effect has to be accounted in computations of particle distribution evolution and all means have to be applied to minimize it to an acceptable level. In this section we generalize the theory which was initially developed in [15] and which describes an effect of RF system noise on the evolution of longitudinal particle distribution.

6.2.1 Noise Induced Diffusion for Nonlinear Oscillator

A particle motion in the field of nonlinear oscillator perturbed by noise can be described by a Hamiltonian $H(\phi, \hat{p}, t)$ consisting of the main unperturbed part and a perturbation driven by a small random value $\alpha(t)$:

$$H(\phi,\hat{p},t) = H_0(\phi,\hat{p}) + \alpha(t)\hat{V}(\phi,\hat{p}). \tag{6.87}$$

Let us apply a canonical transformation to the action and phase variables I, ψ of the unperturbed Hamiltonian: $H_0(\phi,\hat{p}) = H_0(I)$, leading to the oscillation frequency $\omega(I) = dH_0/dI$.

Perturbation changes the action I so that:

$$\frac{dI}{dt} = -\alpha(t)\frac{\partial\hat{V}}{\partial\psi} = -\frac{\alpha(t)}{\omega}\frac{d\hat{V}}{dt} \equiv -\frac{\alpha(t)}{\omega}W(\phi,\hat{p}), \tag{6.88}$$

where $W = -d\hat{V}/dt$ is a power function of the perturbation. The noise $\alpha(t)$ is conventionally described by its correlator $K(\tau)$:

$$\langle\alpha(t)\rangle = 0, \quad \langle\alpha(t)\alpha(t-\tau)\rangle = K(\tau). \tag{6.89}$$

Let Δt be a time interval, large compared with the noise correlation time, but still so small, that action changes only a little for that time.[7] Thus, at lowest order over the small parameter α, the action changes according to

$$\begin{aligned}\left\langle \Delta I^2 \right\rangle &= \frac{1}{\omega^2}\left\langle \int_t^{t+\Delta t}\int_t^{t+\Delta t} \alpha(t_1)W(t_1)\alpha(t_2)W(t_2)dt_1dt_2 \right\rangle \\ &= \frac{\Delta t}{\omega^2}\int_{-\infty}^{\infty} K(\tau)c(\tau)d\tau,\end{aligned} \tag{6.90}$$

where $c(\tau) \equiv \langle W(t)W(t-\tau)\rangle_t$ and $\langle\rangle_t$ denotes time averaging over a period of the nonlinear oscillations $T = 2\pi/\omega$.

Ensemble of these oscillators can be described by a distribution function $f(I, t)$. Its evolution is induced by the noise and satisfies the Fokker–Planck equation (FPE) of (6.74). Taking initial distribution being localized at small interval of actions near I, or $f(I') = \delta(I' - I)$, a change of action is determined by Eq. (6.76). Comparing Eqs. (6.90) and (6.76), one obtains the diffusion coefficient:

$$D_{||}(I) = \frac{1}{I\omega}\int_{-\infty}^{\infty} K(\tau)c(\tau)d\tau. \tag{6.91}$$

To express the diffusion through the noise spectral density we expend the periodic function $c(t)$ into the Fourier series:

[7] It implies that the emittance growth rate is sufficiently small which is true in hadron colliders and storage rings.

$$
\begin{aligned}
c(\tau) &= \sum_{n=-\infty}^{\infty} c_n \exp(in\omega\tau), \\
c_n &= \frac{1}{T}\oint \exp(-in\omega\tau)c(\tau)d\tau = \frac{1}{T^2}\oint\oint \frac{dV}{dt'}\frac{dV}{dt''}\exp\left(-in\omega\left(t' - t''\right)\right)dt'dt'' \\
&= |W_n|^2 = n^2\omega^2|V_n|^2,
\end{aligned}
\tag{6.92}
$$

where the Fourier amplitudes are given by

$$
V_n = \frac{1}{T}\oint \hat{V}\left(\phi(t), \hat{p}\left(t\right)\right)\exp(-in\omega t)dt. \tag{6.93}
$$

Usually, the unperturbed Hamiltonian is presented as a sum of kinetic and potential energies: $H_0(\phi, \hat{p}) = \hat{p}^2/2 + U(\phi)$. In this case, it can be more convenient to perform a calculation of the Fourier images (6.93) transforming them to integrals over the coordinate:

$$
W_n = \frac{1}{T}\oint W\exp(-in\omega t)dt = \frac{1}{T}\oint W\exp(-in\omega t(\phi))\frac{d\phi}{\hat{p}\left(\phi\right)}, \tag{6.94}
$$

where $t(\phi)$ is a function inverse to $\phi(t)$. Note that the functions $p(\phi)$ and $t(\phi)$ are not single-valued; they require separate analytic equations for every trajectory interval between the turning points in the unperturbed potential $U(\phi)$. In a simplest case when $U(\phi)$ is an even function with a single local minimum at $\phi = 0$ there are only two turning points, $\phi = \pm\alpha(I)$, and

$$
t(\phi) = \begin{cases} t_0(\phi) \equiv \int_0^x d\phi' / \left|\hat{p}\left(\phi'\right)\right|, & \text{for the half cycle with } \hat{p} > 0, \\ T_0/2 + t_0(-\phi), & \textit{otherwise}. \end{cases} \tag{6.95}
$$

These expressions can be further simplified when the perturbing potential $\hat{V}\left(t\right) = \hat{V}\left(\phi(t), \hat{p}\left(t\right)\right)$ has a definite parity. If it is odd $\left(\hat{V}\left(t + T/2\right) = -\hat{V}\left(t\right)\right)$, all even harmonics of Eq. (94) are zeroed, and the result can be presented as:

$$
|W_n| = \begin{cases} \frac{4}{T}\left|\int_0^a \frac{d\phi}{\hat{p}} W\sin\left(n\omega t_0(\phi)\right)\right|, & \text{for odd } n \\ 0, & \text{otherwise} \end{cases}, \quad \text{for odd } \hat{V}, W. \tag{6.96}
$$

In opposite case

$$
|W_n| = \begin{cases} \frac{4}{T}\left|\int_0^a \frac{d\phi}{\hat{p}} W\cos\left(n\omega t_0(\phi)\right)\right|, & \text{for even } n \neq 0 \\ 0, & \text{otherwise} \end{cases}, \quad \text{for even } \hat{V}, W. \tag{6.97}
$$

The diffusion coefficient of Eq. (6.91) can be expressed as a Fourier series of the noise power at harmonics $n\omega$:

$$D(I) = \frac{4\pi}{I\omega}\sum_{n=1}^{\infty} |W_n|^2 P(n\omega), \tag{6.98}$$

where

$$P(\omega) = \frac{1}{2\pi}\int_{-\infty}^{\infty} K(\tau)\mathrm{e}^{-i\omega\tau}d\tau \tag{6.99}$$

is the noise spectral power at n-th harmonic of oscillations, so that $K(\tau) = \int_{-\infty}^{\infty} P(\omega)\mathrm{e}^{i\omega\tau}d\omega$.

The diffusion is driven by the noise power at resonance harmonics. If the noise is white, $P(n\omega) = P$ and $K(\tau) = 2\pi P\delta(\tau)$, the diffusion comes out as

$$D(I) = \frac{2\pi P\langle W^2\rangle}{I\omega} = \frac{P}{I}\oint W^2 dt. \tag{6.100}$$

The above equations solve a general problem of nonlinear oscillator affected by noise. The distribution function of such oscillators is described by the FPE (6.74), and the diffusion coefficient is calculated by one or another method described above.

6.2.2 Linear Oscillator

A simplest application of the suggested approach is a linear oscillator driven by noise. Then $H_0 = \hat{p}^2/2 + U(\phi)$,

$$U(\phi) = {\Omega_\mathrm{s}}^2\phi^2/2, \quad \phi = \sqrt{2I/\Omega_\mathrm{s}}\sin\psi, \hat{p} = \sqrt{2I\Omega_\mathrm{s}}\cos\psi. \tag{6.101}$$

In the case of phase noise the perturbation is described by $\hat{V}(\phi) = {\Omega_\mathrm{s}}^2\phi$ and $\alpha(t) \equiv \widetilde{\phi}(t)$, where $\widetilde{\phi}(t)$ is the function describing RF phase fluctuations with corresponding spectral density of $P_\phi(\omega)$. That yields a constant diffusion determined by the noise spectral density at the synchrotron frequency:

$$D = 2\pi{\Omega_\mathrm{s}}^4 P_\phi(\Omega_\mathrm{s}), \quad \frac{d}{dt}\overline{\phi^2} = \pi{\Omega_\mathrm{s}}^2 P_\phi(\Omega_\mathrm{s}), \quad \frac{d}{dt}\overline{I} = \pi{\Omega_\mathrm{s}}^3 P_\phi(\Omega_\mathrm{s}). \tag{6.102}$$

In the case of amplitude noise the perturbation is described by $\hat{V}(\phi) = {\Omega_\mathrm{s}}^2\phi^2/2$ and $\alpha(t) = \widetilde{V}(t)/V_0$, where $\alpha(t)$ is the relative RF voltage fluctuations with

corresponding spectral density of $P_u(\omega)$. That yields a constant diffusion linearly growing with action determined by the noise spectral density at the double synchrotron frequency:

$$D = \pi \Omega_s{}^3 I P_u(2\Omega_s), \quad \frac{d}{dt}\overline{\phi^2} = \pi \Omega_s{}^2 \overline{\phi^2} P_u(2\Omega_s), \\ \frac{d}{dt}\bar{I} = \pi \Omega_s{}^2 I P_u(2\Omega_s). \tag{6.103}$$

6.2.3 Phase and Amplitude Noise in Storage Rings with Single Harmonic RF

Now let us apply a general theory developed above to an analysis of the bunch widening due to noise in a single harmonic RF system. Then the unperturbed longitudinal motion is described by the Hamiltonian:

$$H(\phi, p) = \frac{\hat{p}^2}{2} + \Omega_s{}^2(1 - \cos\phi), \tag{6.104}$$

where $\Omega_s = \omega_0 \sqrt{eV_0 h\eta / \left(2\pi mc^2 \gamma \beta^2\right)}$ is the synchrotron frequency, η is the ring slip-factor, ω_0 is the angular frequency of particle revolution, and h is the harmonic number. The canonical momentum $\hat{p}$ is associated with the energy offset as $\hat{p} = \eta h \omega_0 \delta p / p$. A noise in the amplitude $\widetilde{V}(t)$ and phase $\widetilde{\phi}(t)$ of RF voltage is accounted by substitution,

$$V_0 \to V_0 + \widetilde{V}(t), \quad \phi \to \phi + \widetilde{\phi}(t),$$

leads to the Hamiltonian similar to (6.87):

$$H(\phi, \hat{p}) = \frac{\hat{p}^2}{2} + \Omega_s{}^2(1 - \cos(\phi)) - \Omega_s{}^2 \widetilde{u}(t)\cos\phi + \Omega_s{}^2 \widetilde{\phi}(t)\sin\phi \\ = H_0 + \widetilde{u}(t) V_u + \widetilde{\phi}(t) V_\phi. \tag{6.105}$$

where $\widetilde{u}(t) = \widetilde{V}(t)/V_0$, and we assume that $\gamma > \gamma_t$.

The solution for unperturbed motion is well known. The turning point phase, the action and frequency are:

$$\phi_{\max} = 2a \sin\left(\sqrt{H/(2\Omega_s)}\right), \\ I = \frac{1}{2\pi}\oint \hat{p}\, dx = \frac{8\Omega_s}{\pi}\left(\mathrm{E}(\kappa) - \left(1 - \kappa^2\right)K(\kappa)\right) \le \frac{8\Omega_s}{\pi}, \\ \omega = 2\pi \left(\oint \frac{dx}{\hat{p}}\right)^{-1} = \frac{\pi \Omega_s}{2K(k)} \le \Omega_s, \tag{6.106}$$

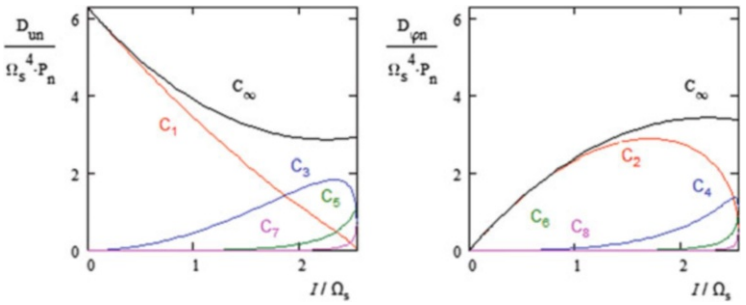

Fig. 6.2 Dimensionless diffusions for the phase (*left*) and amplitude (*right*) RF noise

where $\kappa = \sin(\phi_{\max}/2) = \sqrt{H/(2\Omega_s)}$, and a substitution

$$\sin(\phi/2) = \sin(\phi_{\max}/2)\sin\psi \equiv \kappa\sin\psi \tag{6.107}$$

was used to reduce the integrals to the elliptic functions: $\mathrm{E}(k) = \int_0^{\pi/2}\sqrt{1-k^2\sin^2(\phi/2)}d\phi$ and $K(k) = \int_0^{\pi/2} d\phi/\sqrt{1-k^2\sin^2(\phi/2)}$.

To find the diffusion for the white noise we use (6.100), where we take into account that the correlation functions for phase and amplitude noises are $K_\phi(\tau) = 2\pi P_\phi\delta(\tau)$ and $K_u(\tau) = 2\pi P_u\delta(\tau)$, and P_ϕ and P_u are the spectral powers of the phase and amplitude noise $\widetilde{\phi}(t)$ and $\widetilde{u}(t)$. Simple calculations yield both diffusion coefficients:

$$\begin{aligned} D_\phi &= \frac{8P_\phi\Omega_s^5}{I}\int_0^{\phi_{\max}}\cos^2\phi\sqrt{\kappa^2-\sin^2(\phi/2)}d\phi = \frac{8P_\phi\Omega_s^5}{I}\big(2E(\kappa)-2\big(1-\kappa^2\big)K(\kappa)-\mathrm{R}(\kappa)\big), \\ D_u &= \frac{8P_u\Omega_s^5}{I}\int_0^{\phi_{\max}}\sin^2\phi\sqrt{\kappa^2-\sin^2(\phi/2)}d\phi = \frac{8P_u\Omega_s^5}{I}\mathrm{R}(\kappa), \end{aligned} \tag{6.108}$$

where

$$\mathrm{R}(\kappa) = \frac{8}{15}\left[2\big(1-\kappa^2+\kappa^4\big)E(\kappa) - \big(2-3\kappa^2+\kappa^4\big)K(\kappa)\right]. \tag{6.109}$$

The curves marked as C_∞ in Fig. 6.2 present dependencies of these diffusions on the action in a dimensionless form. For small amplitude oscillations these functions coincide with the results for linear approximation of Eqs. (6.102) and (6.103).

For colored noise using Fourier amplitudes of Eq. (6.93) one obtains:

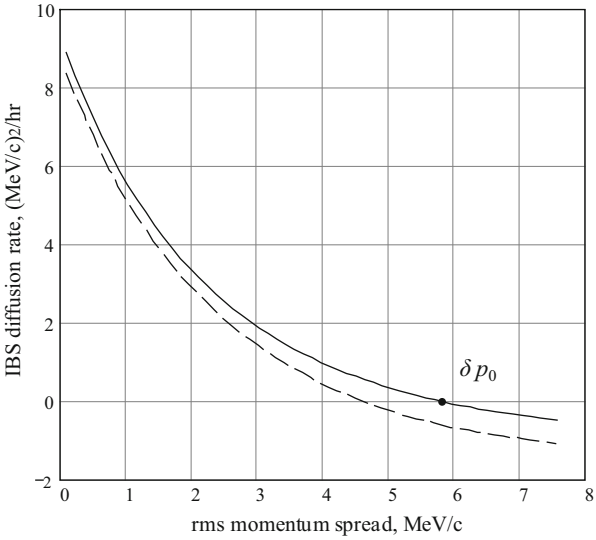

Fig. 6.3 The calculated longitudinal IBS diffusion rate as a function of the rms beam momentum spread in the Recycler for a coasting beam of 100×10^{12} antiprotons with a constant 5 μm emittance (norm. 95 %). The *solid line* is modeled with realistic beta-functions; the *dashed line* is the round-beam, zero-dispersion, smooth approximation

$$D_\phi = \sum_{n=1}^{\infty} P_\phi(n\omega) C_{\phi n}(I), \quad C_{\phi n}(I) = \frac{\omega \Omega_s{}^4}{\pi I} \left| \oint d\phi \cos\phi \exp(in\omega t(\phi)) \right|^2,$$
$$D_u = \sum_{n=1}^{\infty} P_u(n\omega) C_{un}(I), \quad C_{un}(I) = \frac{\omega \Omega_s{}^4}{\pi I} \left| \oint \frac{d\phi}{2\pi} \sin\phi \exp(in\omega t(\phi)) \right|^2. \tag{6.110}$$

Due to symmetry function $C_{\phi n}(I) = 0$ for even n, and $C_{un}(I) = 0$ for odd. The first few nonzero functions are presented in Fig. 6.3. In the case of white noise the spectral density is the same at all harmonics. Consequently, it can be moved out of sums in Eq. (6.110). Then the coefficients

$$C_{\phi\infty} = \sum_{n=1}^{\infty} C_{\phi n}, \quad C_{u\infty} = \sum_{n=1}^{\infty} C_{2n}, \tag{6.111}$$

describe the diffusion due to white noise so that $D_\phi = PC_{\phi\infty}$ and $D_u = PC_{u\infty}$. These equations are identical to Eq. (6.108).

The integrals in Eq. (6.110) can be calculated using properties of the Jacobian elliptic functions appearing after the substitution (6.107) and leading to:

$$\theta = am(\vartheta, \kappa), \quad \sin(\phi/2) = \kappa sn(\vartheta, \kappa), \quad p = 2\Omega_s cn(\vartheta, \kappa) \text{ with}$$
$$\vartheta = 2K(\kappa)\psi/\pi. \tag{6.112}$$

From here (see [16], p. 911, [17], pp. 292, 295),

$$V_{\phi,n} = \Omega_s{}^2 \oint \frac{d\psi}{2\pi} \sin\phi \exp(in\psi) = -\omega \oint \frac{d\psi}{2\pi} \phi \exp(in\psi) \frac{dp}{d\psi}$$

$$= \begin{cases} \dfrac{2in\omega^2}{\cosh(n\nu)}, & \text{for odd } n \\ 0, & \text{otherwise } n \end{cases} \quad V_{u,n} = \Omega_s{}^2 \oint \frac{d\psi}{2\pi} \cos\phi \exp(in\psi)$$

$$= -2\omega_s{}^2 \kappa^2 \oint \frac{d\psi}{2\pi} sn^2(\vartheta, \kappa) \exp(in\psi) = \begin{cases} \dfrac{2in\omega^2}{\sin h(n\nu)}, & \text{for even } n \\ 0, & \text{otherwise } n \end{cases} \tag{6.113}$$

where $\nu = \pi K'(\kappa)/(2K(\kappa))$.

In conclusion we need to note that in the case when the bandwidth of RF noise is larger than the revolution frequency (like for the LHC RF system) the summing in Eq. (6.110) should also include the revolution frequency harmonics: $\sum_{n=1}^{\infty} C_n P(n\omega_s) \rightarrow \sum_{n,m=1}^{\infty} C_n P(n\omega_s + m\omega_0)$.

6.3 Experimental Studies of Single and Multiple Scattering

6.3.1 IBS in the Fermilab Recycler Ring

The Fermilab Recycler is a 3.3-km 8.9-GeV/c fixed momentum storage ring located in the Fermilab Main Injector tunnel. Table 6.1 presents relevant Recycler parameters. On the Run II, the Recycler played a key role as the repository of large stacks of antiprotons (6×10^{12}) with the appropriate phase space characteristics to be used in collider stores. Small-angle multiple IBS is the dominant heating mechanism, which determines the equilibrium emittance achievable in the Recycler.

The longitudinal IBS heating has been of concern because of a small longitudinal emittance required for Tevatron collisions. Figure 6.3 shows the calculated longitudinal IBS diffusion rate. The IBS theory, described above, has been used to make these calculations. Also, the measured Recycler lattice functions have been used. One can see in Fig. 6.3 (solid line) that the longitudinal heating vanishes for a certain rms momentum spread, δp_o, and becomes cooling above this momentum spread. For comparison, also shown in Fig. 6.3 is the heating (cooling) rate calculated in a smooth, round-beam, zero-dispersion approximation using the value of the average β-function, β_{ave} from Table 6.1. One can exploit this feature of the longitudinal diffusion rate to minimize the longitudinal emittance growth by compressing the bunch length, and thus increasing the momentum spread, until the diffusion rate vanishes. In the Recycler ring this is accomplished by employing a barrier-bucket RF system. For a typical 95 % transverse emittance of 5–7 mm mrad the point of vanishing longitudinal heating cannot be reached without losing the "tail" particles at the momentum aperture. A practical solution has been to maintain the momentum spread as high as possible (around 4 MeV/c), while preserving the

Table 6.1 Recycler ring parameters

Parameter	Value	Units
Average β-function, β_{ave}	30	m
Max. dispersion	2	m
Transition, γ_t	20.7	
Typ. transverse beam emittances (n, 95 %), ε_n	3–7	mm mrad
Number of antiprotons	$\leq$6	10^{12}

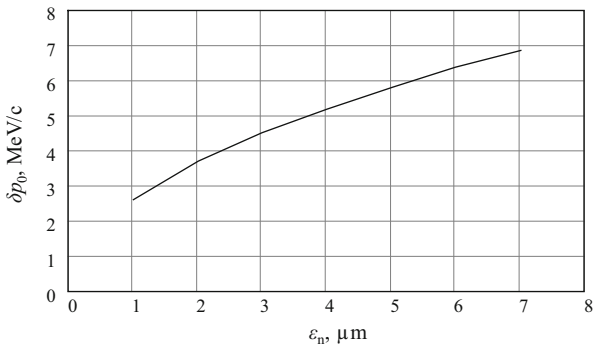

Fig. 6.4 The calculated value of the rms momentum spread in MeV/c, for which the longitudinal IBS heating vanishes, as a function of beam emittance (norm., 95 %)

beam lifetime. Figure 6.4 shows the value of the rms momentum spread, δp_o, for which the diffusion rate vanishes, as a function of the transverse beam emittance.

Below, we describe an experiment in which we created a beam distribution with the momentum spread less than δp_o for a given emittance and observed longitudinal heating, and an experiment in which we created a beam distribution with the momentum spread greater than δp_o for a given emittance and observed longitudinal cooling.

To verify the Recycler IBS model we first created a beam distribution with a large transverse emittance and a small rms momentum spread. According to the IBS model this would correspond to longitudinal heating and small transverse cooling. The vacuum-related transverse heating rate was measured in a separate experiment by recording emittances of a coasting beam with very low current (1×10^{10}) to avoid the IBS contribution. This vacuum-related growth rate was measured to be 0.60 mm mrad/h. Figure 6.5 shows the transverse emittance evolution for a costing beam of 100×10^{10} protons.

One can observe from Fig. 6.5 that the emittance growth rate is in fact smaller than that for a zero beam current. We attribute the difference to IBS-related transverse cooling, which, according to our model, is −0.15 mm mrad/h.

The longitudinal degree of freedom allows us to observe the effect of IBS directly because it is the dominant effect. All other heating mechanisms are negligible for high beam currents. Figure 6.6 shows the evolution of the rms momentum spread for the same beam as in Fig. 6.5. The IBS model uses the transverse emittance growth rate as an input parameter.

The second experiment was to demonstrate the longitudinal IBS cooling. The measurements were conducted with a bunched antiproton beam of 25×10^{10}, which was initially cooled transversely to a very small emittance (<2 mm mrad).

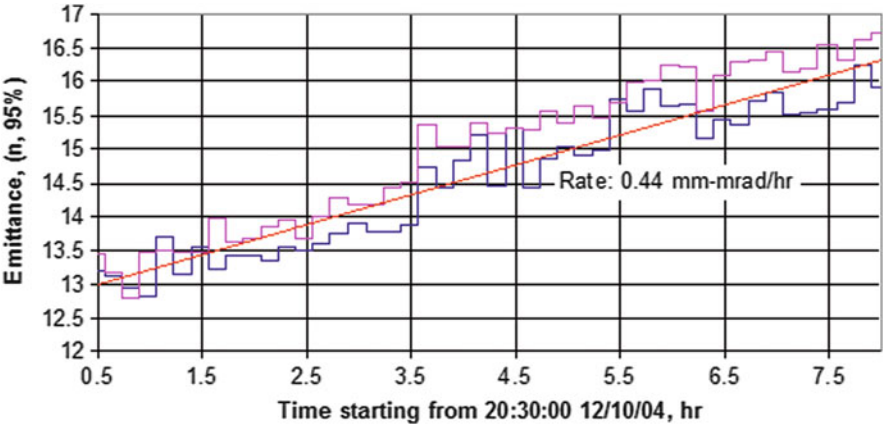

Fig. 6.5 The transverse emittance (horizontal and vertical) evolution for a coasting beam of 100×10^{10} protons in the Recycler. The linear fit yields a growth rate of 0.44 μm/h

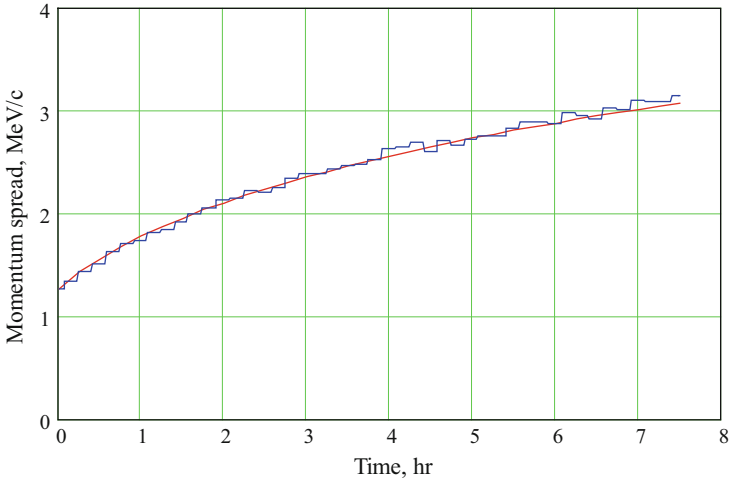

Fig. 6.6 A comparison of the measured rms momentum spread (MeV/c) and the IBS model as a function of time for a coasting beam of 100×10^{10} protons

The rms momentum spread was increased to over 4.5 MeV/c by compressing the beam longitudinally. Figures 6.7 and 6.8 show the measured transverse emittance and longitudinal rms momentum spread evolutions. Also shown is the IBS model. The only adjustable parameter in this model is the vacuum-related emittance growth rate. The best fit corresponds to this rate being 0.55 mm mrad/h—consistent with our previous measurements.

In conclusion, we would like to note that the developed IBS model for the Recycler has been verified with beam measurements made during storage and

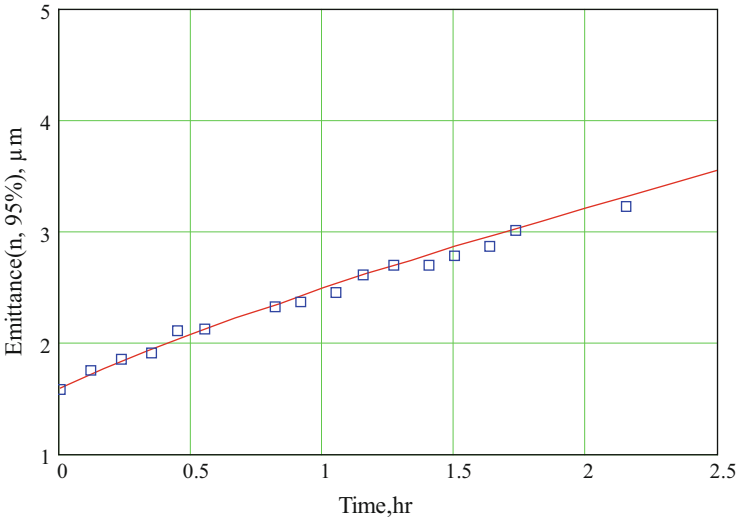

Fig. 6.7 The measured transverse emittance evolution for a bunched antiproton beam (25×10^{10}). Also shown is the IBS model (*solid line*)

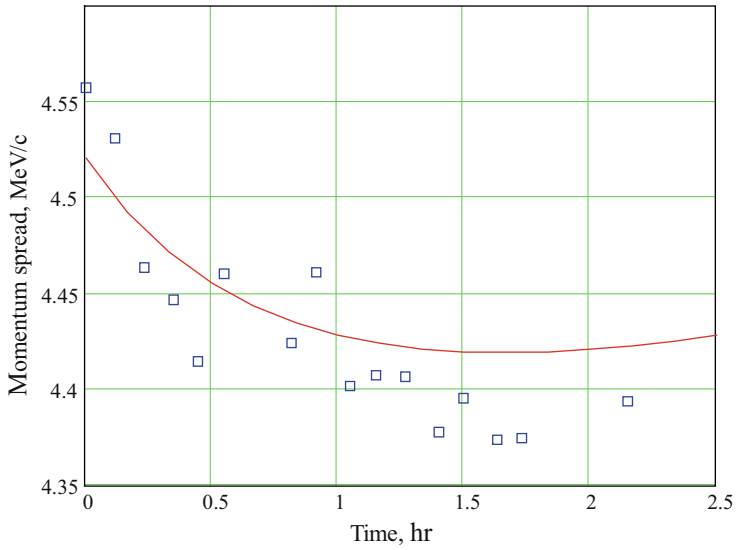

Fig. 6.8 The longitudinal rms momentum spread (MeV/c) as a function of time (hours). The IBS model (*solid line*) has only one adjustable parameter—the vacuum-related transverse emittance growth rate

cooling of the antiprotons before extraction to the Tevatron. We separately verified longitudinal IBS heating and cooling effects by adjusting the beam parameters to demonstrate these effects. Furthermore, the good agreement observed between model and measurement increased our confidence in the beam diagnostics.

6.3.2 Single and Multiple Gas Scattering in Tevatron

The luminosity evolution model described below required separation of different mechanisms affecting the particle loss and emittance growth. In particular we needed to separate the contributions of the gas scattering and the emittance growth driven by external noises, e.g., magnetic field fluctuations, vibrations, etc. Both mechanisms create transverse diffusion but in difference to the magnetic noise the gas scattering creates non-Gaussian tails. This difference was utilized to separate these contributions in the below described experiment [18] carried out in 2002.

First, using the beam scraping it was verified that the particle distribution of a 150 GeV proton beam, injected into Tevatron, is very close to a Gaussian one. Second, a new beam was injected. It was unbunched to exclude the beam heating by the RF noise and the IBS. The beam intensity was sufficiently small to make sure that the coherent effects did not affect the beam dynamics. Third, the beam was scraped horizontally and vertically. The scraping time of a few minutes is much shorter than a characteristic time of the beam evolution. The fraction of particles removed by the vertical scraping (~25 %) allowed us to predict the initial vertical particle distribution with sufficient accuracy. Fourth, the beam scrapers were removed and the beam was left untouched for 1 h. Then, we moved the vertical scraper in, while recording the beam intensity as a function of the scraper position. The vertical scraper was chosen so that the beam momentum spread would not affect the measurements.

The results of the measurements and the comparison with numeric simulations are shown in Fig. 6.9. Taking into account that only one fitting parameter, the unknown average Tevatron beampipe vacuum pressure, is used there is a good agreement between the theory and the measurements. Note that although the Coulomb logarithm is not a well-determined value and depends on Z its uncertainty does not exceed 10–20 %. The experimentally determined value, L_c, coincides with the theoretical one within 5 % for $Z = 7$. The measured 0.8 mm mrad/h emittance growth rate (rms normalized) corresponds to an average Tevatron vacuum of 4×10^{-9} Torr (room-temperature N_2 equivalent). Note that high accuracy of the beam current measurements allowed us to measure tiny tails of the distribution function, which could not be seen by regular beam profile monitors. If the large angle scattering is switched off in the simulations, so that particle scattering is described by diffusion only, there is large difference between calculations and measurements as presented in Fig. 6.10.

A good agreement between the observed and the predicted distribution function tails yields an important practical conclusion that the emittance growth at the injection energy is largely due to gas scattering. However the accuracy of the experiments does not exclude an emittance growth rate excited by noise in magnets at the level of about 20 %, i.e., about 0.16 mm mrad/h. Vacuum improvements carried out in 2003–2006 further reduced the emittance growth rate and the beam loss due to scattering on the residual gas by a factor of 5–10. Indirect measurements point out that the emittance growth rate does not exceed 0.1 mm mrad/h at injection.

The normalized emittance growth due to gas scattering is inversely proportional to the beam energy and is about 6.5 times smaller at the collision energy. We have

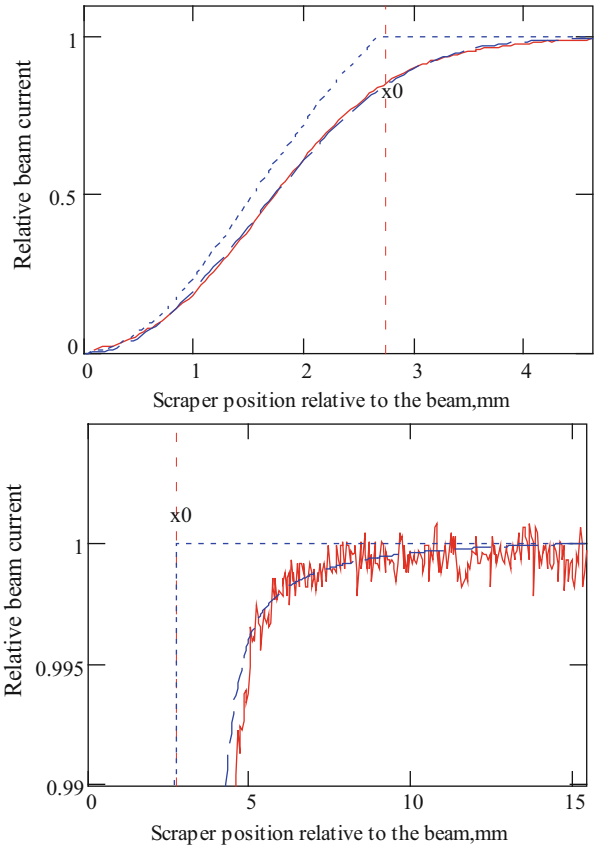

Fig. 6.9 Dependence of the beam current on the vertical scraper position for the beam core (*top*) and beam tails (*bottom*); *solid line*—measurements, *dashed line*—computer simulations for $L_c = 8.6$, *dotted line*—the dependence which would be measured with the initial distribution; x_0 marks the final scraper position at the initial scraping

limited knowledge about the magnetic field fluctuations in the Tevatron magnets but have reasons to believe that their contribution to the normalized emittance growth rate at the top energy is bigger than the one due to the vacuum (see next section).

6.3.3 Emittance Growth Mechanisms in the Tevatron Beams

The luminosity in the head-on collisions can be obtained from a well-known formula

$$L = \gamma f_B \frac{N_a N_p}{4\pi\beta^* \varepsilon} H(\sigma_s/\beta^*), \tag{6.114}$$

where ε is the average rms normalized emittances of two round beams $(\varepsilon_a + \varepsilon_p)/2$, $H(x)$ is the "hourglass factor" which depends on the ratio of the RMS bunch length σ_s and beta-function at IPs β^*, γ is the relativistic factor, and f_B is the frequency of

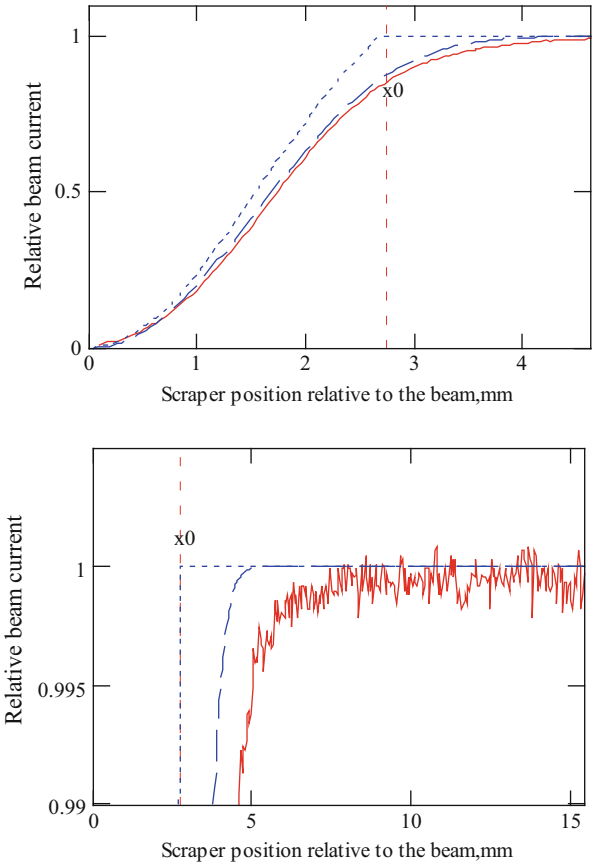

Fig. 6.10 The same as Fig. 6.9, but the large angle scattering is switched off in the model

bunch collisions. Evolution of the Tevatron luminosity over the course of colliding store can be well approximated by a simple empirical fit [19]:

$$L(t) = \frac{L_0}{1 + t/\tau_{\mathrm{L}}}, \tag{6.115}$$

with only two parameters are used: the initial luminosity L_0 and the initial luminosity lifetime τ_{L}. The luminosity integral $I = \int L dt$ is the most critical parameter for collider experiments. It depends on the product of peak luminosity and the luminosity lifetime, e.g., for a single store with initial luminosity L_0 and duration T, the integral is $I \approx L_0 \tau_{\mathrm{L}} \ln(1 + T/\tau_{\mathrm{L}})$. From Eq. (6.114), one obtains:

$$\tau_{\mathrm{L}}^{-1} = \frac{dL(t)}{L(t)dt} = \left|\tau_{\varepsilon}^{-1}\right| + \tau_{N_{\mathrm{a}}}^{-1} + \tau_{N_{\mathrm{p}}}^{-1} + \tau_{\mathrm{H}}^{-1}. \tag{6.116}$$

The luminosity lifetime has four major contributions coming from the growth rates of beam emittances, the beam intensity decay rates, and the hourglass factor

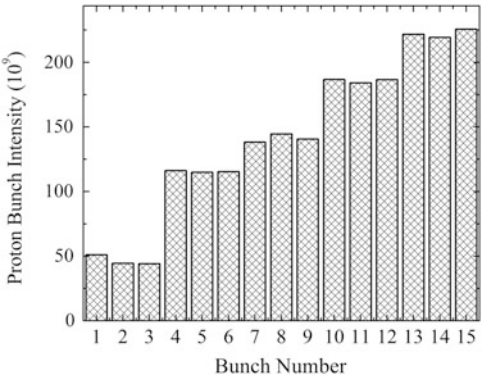

Fig. 6.11 Proton bunch populations at the beginning of the experimental studies store [20]

decay rate. For the end of the Collider Run II operation with range of initial luminosities between 3.0×10^{32} cm^{-2} s^{-1} to 4.0×10^{32}, the largest contribution to the luminosity lifetime of about $\tau_L = 5.2$–5.7 h came from the beam emittance growth with a typical time of $\tau_\varepsilon \sim 10$–13 h. The growth was dominated by IBS in the proton and antiprotons bunches, with small contributions coming from the beam gas scattering and external noises. The beam–beam effects can lead to fast emittance blowups and significant losses (see discussion in Chap. 8) but those were routinely corrected or compensated. The hourglass factor decays with $\tau_H \sim 70$–100 h due to longitudinal IBS heating and a smaller contribution coming from the RF system noises.

Several beam experiments have been conducted to separate contributions of different phenomena to the emittance growth. In one of them [20], 15 proton bunches with various intensities were accelerated to 980 GeV, positioned to the proton helix with the low-beta optics (see Fig. 6.11). The bunches had very different emittances ε varied from 2.3 to 3.6 π mm mrad and rms bunch lengths σ_z in the range from 1.71 to 2.10 ns. The bunches were left in the machine for 3.1 h and their emittances, bunch lengths, and intensities were regularly measured by the Flying Wires system and the SBD system, correspondingly (see details on the Tevatron beam instrumentation in Chap. 9).

The transverse velocity spread is much larger than the longitudinal one for the Tevatron bunches. Then, neglecting the dispersion contribution to the beam size and further simplifying Eq. (6.54) one obtains estimates for the growth rates:

$$\frac{d\varepsilon_T}{dt} \approx \frac{\gamma^{3/4} N_p C_T}{{\varepsilon_T}^{1.5} \varepsilon_L^{0.5}}, \qquad \frac{d\sigma_z^2}{dt} \approx \frac{N_p C_L}{\gamma^{1/4} {\varepsilon_T}^{1.5} \varepsilon_L^{0.5}}, \tag{6.117}$$

where C_L and C_T are the constants determined by machine parameters, and both vertical and horizontal emittances are assumed equal, $\varepsilon_x \approx \varepsilon_y \approx \varepsilon_T$. Equation (6.117) suggests that the IBS-driven emittance growth has to be proportional to the factor $F_{IBS} = N_p/({\varepsilon_T}^{1.5}\sigma_s)$. Note that in the described below analysis we used the vertical emittance only because its systematic error and uncertainty for the Tevatron Flying Wires system are much smaller than for the horizontal emittance.

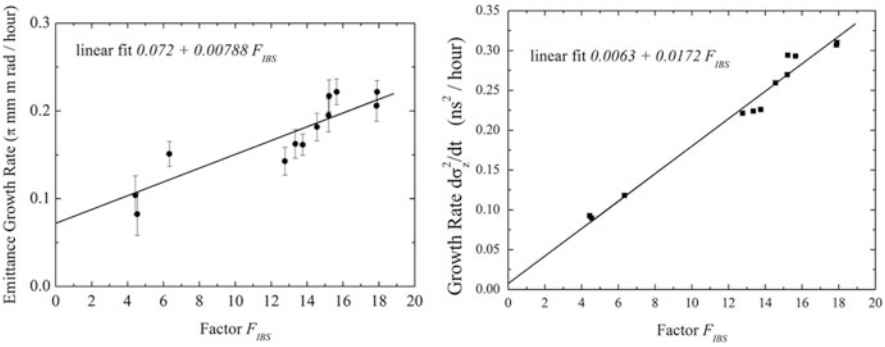

Fig. 6.12 Vertical emittance growth rates (rms, norm.) of proton bunches vs the IBS factor F_{IBS} (*left*); the rms bunch length growth rates vs the IBS factor F_{IBS} (*right*) [20]

Such choice is justified by the presence of strong $x-y$ coupling which is additionally amplified by operation close to the coupling resonance. That results in an equalization of emittances so that they are quite close and are proportional to each other. The experience accumulated in the course of Run II also verifies such choice. Since the bunch emittances are evolving in time, then F_{IBS} is a function of time, too. The observed growth rates for the emittance and the rms bunch length are plotted versus F_{IBS} for all the bunches are presented in Fig. 6.12.

The observed growth rates can be approximated by linear fits:

$$\begin{aligned}\frac{d\varepsilon_V}{dt}\left[\pi\,\mathrm{mm\,mrad/h}\right] &= \left(0.072 \pm 0.02\right) + \left(0.0079 \pm 0.0015\right)\cdot F_{\mathrm{IBS}},\\ \frac{d\sigma_s^2}{dt}\left[\mathrm{ns}^2/\mathrm{h}\right] &= \left(0.0063 \pm 0.0193\right) + \left(0.0173 \pm 0.0013\right)\cdot F_{\mathrm{IBS}}.\end{aligned} \tag{6.118}$$

The intercept in the transverse emittance growth of 0.072 π mm mrad/h yields an upper estimate on the growth rate due to intensity independent effects such as scattering on the residual gas and diffusion driven by external noises. The emittance growth due to the gas scattering is equal to

$$\frac{d\varepsilon_{x,y}}{dt} = \frac{2\pi c {r_{\mathrm{p}}}^2}{\gamma\beta^2}\left(\sum_i n_i Z_i (Z_i+1) L_{C_i}\right)\overline{\beta_{x,y}}, \tag{6.119}$$

where $\overline{\beta_{x,y}} = \int \beta_{x,y} ds/C \approx 70$ m. It yields that the observed zero-intensity emittance growth rate corresponds to an equivalent average room-temperature N_2 ($Z_i = 7$) vacuum pressure of $(2.4 \pm 0.7) \times 10^{-9}$ Torr, which, consequently, yields the beam intensity lifetime due to nuclear beam-gas interaction of about 140 ± 40 h. It contradicts to the measured beam lifetime of about $\tau_{\mathrm{H}} \sim 800 \pm 500$ h (confirmed in many other similar measurements), i.e., less than 20 % of the observed low intensity beam emittance growth rate is due to the gas scattering.

Consequently, the corresponding equivalent average pressure of room-temperature N_2 is less than $P \approx 0.5 \times 10^{-9}$ Torr; and that most of the growth rate ($\approx$0.06 π mm mrad/h) is related to other mechanism. The most probable reason is the emittance growth related to the transverse beam shaking at the lowest betatron sideband exited by noise in magnets. Note that the large angle electromagnetic scattering on the residual gas and the Touschek scattering give rise to the lifetimes of about 30,000 and 7,000 h, respectively, and, thus, produce negligible contributions to beam loss.

Indirect confirmation of the noise effect comes from the observed ambient beam betatron motion amplitude of some 110 nm in one of the high-beta (900 m) BPMs during collisions (corresponding to $A_\beta \approx$ 10-25 nm at the arcs, see Chap. 2, Sect. 2.4). That exceeds the Schottky noise by more than an order of magnitude. If that motion is due to the external noise, then corresponding emittance growth rate can be estimated as:

$$\frac{d\varepsilon_{\mathrm{T}}}{dt} \approx \gamma f_0 \frac{A_\beta^2}{2\overline{\beta} N_{\mathrm{dec}}}, \tag{6.120}$$

where N_{dec} the decoherence time expressed in the number of turns. That yields the growth rate of about 0.01–0.05 π mm mrad/h in high luminosity stores. Here we assumed that N_{dec} is mostly determined by nonlinearity of the beam–beam forces and is estimated to be about 50–100 turns for protons with beam-beam parameter of $\xi \sim 0.02$.

The intercept in the bunch length growth is proportional to lengthening due to RF noise. Assuming that the phase noise dominates one obtains a spectral density of phase noise at the synchrotron frequency[8] $5 \cdot 10^{-11}$ rad^2/Hz. It coincides with the direct phase noise measurements within measurement accuracy.

6.4 Tevatron Run II Beam Halo Collimation System and Collimation Studies

Even in good operational conditions, a finite fraction of the beam will leave the stable central area of accelerator because of beam–gas interactions, IBS, proton–antiproton interactions in the IPs, RF noise, ground motion, and resonances excited by the accelerator elements imperfection. These particles form a beam halo. As a result of halo interactions with limiting apertures, hadronic and electromagnetic showers are induced in accelerator and detector components causing numerous deleterious effects ranging from minor to severe. The most critical for colliders are beam losses in superconducting magnets and accelerator related backgrounds in the

[8] Note that by definition the spectral density used in measurements is 4π larger than the spectral density used in Sect. 6.2.3.

collider detectors. Only with a very efficient beam collimation system can one reduce uncontrolled beam losses in the machine to an allowable level. Beam collimation is mandatory at any superconducting hadron collider to protect components against excessive irradiation, minimize backgrounds in the experiments, maintain operational reliability over machine life, and reduce the impact of radiation on the environment [21].

During the Collider Run I (1994–1996) the Tevatron halo removal system experienced limitations that prompted a design of a new system for the Collider Run II. The new design specified that the entire halo removal process needed to be more efficient and putting the collimators in after the beam acceleration has to be much faster with the target time of about 5 min. This implied that the halo removal process would have to be based on a two-stage collimation and setting the collimation up have to be automated. A new collimation system [22] has been designed for the Tevatron Run II to localize most of the losses in the straight sections D17, D49, EØ, F17, F48, F49, and AØ. It incorporated four *primary collimators* (targets) and eight newly built 1.5-m long *secondary collimators*. New motion control hardware capable of fast processing of data from beam loss beam intensity monitors was installed. That allowed us to build a computer controlled feedback allowing us to achieve a 2 in. collimator displacement (full travel) within 15 s. A central control software system was also developed to coordinate the global sequence of motion for all 12 collimators while incorporating the halo removal system into the Tevatron Collider sequencer software. At the design stage, a multi-turn particle tracking and beam halo interactions with the collimators were performed with the STRUCT code [23]. Using the STRUCT calculated beam loss distributions and the MARS code [24] we carried out the Monte Carlo hadronic and electromagnetic shower simulation, and the secondary particle transport in the accelerator and detector components, including shielding calculations with real materials and magnetic fields. The Collider Run II halo removal system was installed, commissioned, and became operational since June 2001.

The system was upgraded several times following operational needs. For example, in 2002, the Tevatron Electron Lenses (TEL) have been set up to remove undesirable uncaptured particles from the abort beam gaps and, thus, reduce the risk of damage of high-energy physics particle detectors CDF and D0 during beam aborts. In 2003, following several instances of unsynchronized abort kicker pre-fires in the Tevatron, an additional *tertiary* collimator was installed at the A48 location to protect the CDF detector components [25]. In 2005 the beam scraping procedures were optimized for faster operation and highly efficient repeated scraping (double scraping) of the beams. Also, in 2010 a collimation during the portion of the low-beta squeeze was added in order to reduce losses at CDF and D0 that were causing frequent quenches. Quenching the low-beta quadrupoles during the squeeze became more of a problem once the antiproton intensity and beam brightness became larger. Sensitive steps in the low-beta squeeze, where the beam separation between the proton and antiproton is small, create losses at large beta locations, mainly the cryogenic low-beta quadrupoles. A single collimator at E0 was placed at 5σ to create a limiting aperture moving the loss point of sensitive steps away from CDF and D0 IPs to a region that has robust quench limits.

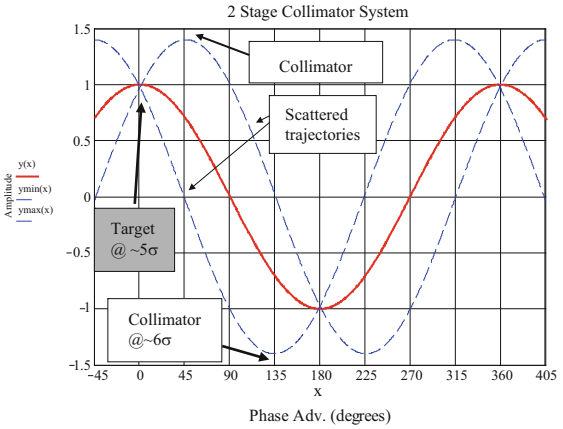

Fig. 6.13 Placement of the target and secondary collimators to produce a two-stage collimator system [27]

This additional collimator has worked well, allowing an increase in number of antiprotons while basically excluding quenches in the low-beta squeeze. Novel ideas to improve the beam collimation efficiency—namely, a bent crystal collimation and hollow electron beam collimation— have been extensively and successfully studied at the end of Run II.

6.4.1 Collimation System Design

The principles of a two-stage collimation system are described in [21]. The system consists of horizontal and vertical primary collimators and a set of secondary collimators placed at an optimal phase advance, to intercept most of the particles out-scattered from the primary collimators during the first turn after beam halo interaction with primary collimators. An impact parameter of multi-GeV and TeV protons on the primary collimators is ~1 μm [26]. The design studies [22] show that in the Tevatron, a 5-mm thick tungsten primary collimator positioned at 5σ (of rms beam size) from the beam axis in both vertical and horizontal planes would function optimally, reducing the beam loss rates as much as a factor of 4–10 compared to the system without such a scatterer. Secondary collimators located at the appropriate phase advances are a 1.5-m long L-shaped steel jaws positioned at 6σ from the beam axis in the horizontal and vertical planes. They are aligned parallel to the envelope of the circulating beam. Figure 6.13 schematically depicts placement of the collimators in such a system.

In the course of Run II the halo removal system consist of 12 collimators. Four of them are primary collimators and eight are secondary collimators. The collimators are arranged in four sets: two proton and two antiproton sets. They are installed around the Tevatron ring as shown in Fig. 6.14. Placement of collimators in the Tevatron is limited to a few locations since there is limited warm space and the proton and antiproton beams are on helical orbits.

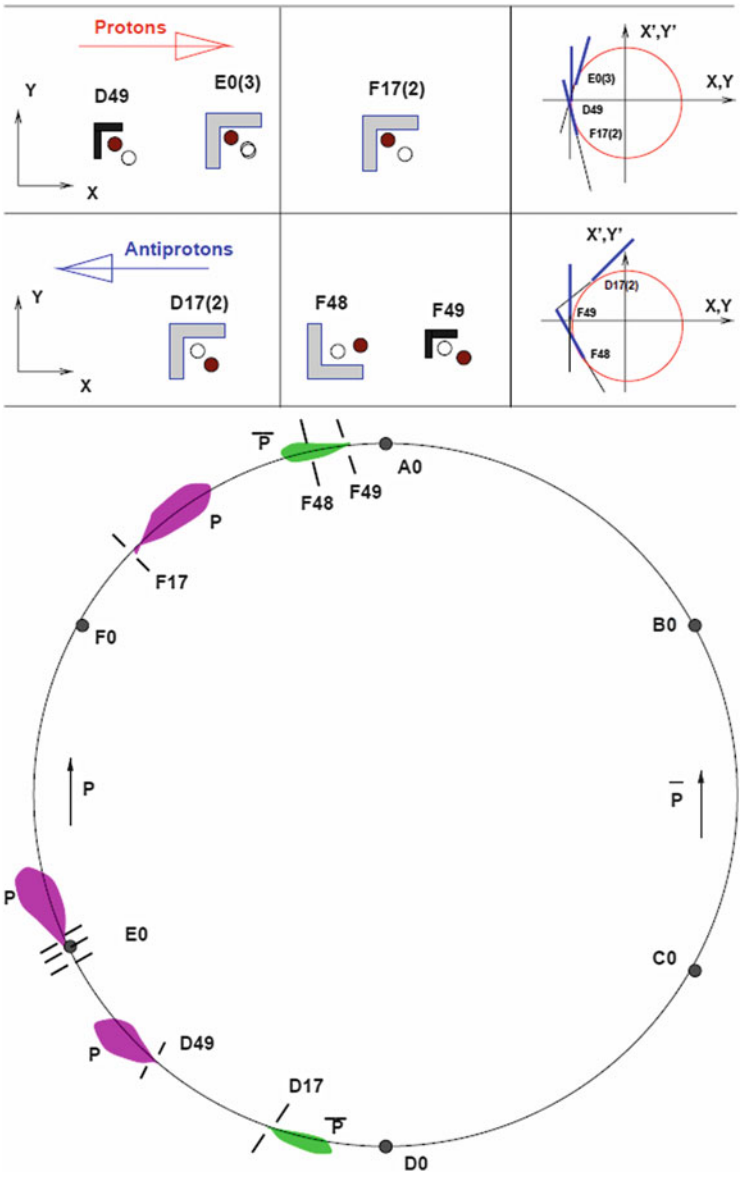

Fig. 6.14 Tevatron Collider Run II Halo Removal Collimator Layout. CDF and D0 detectors are located at B0 and D0, respectively [27]

A proton primary collimator is placed at the beginning of the D17 straight section outward and up of the closed orbit (Fig. 6.14). It intercepts the large amplitude protons and a positive off-momentum beam. Protons scattered from

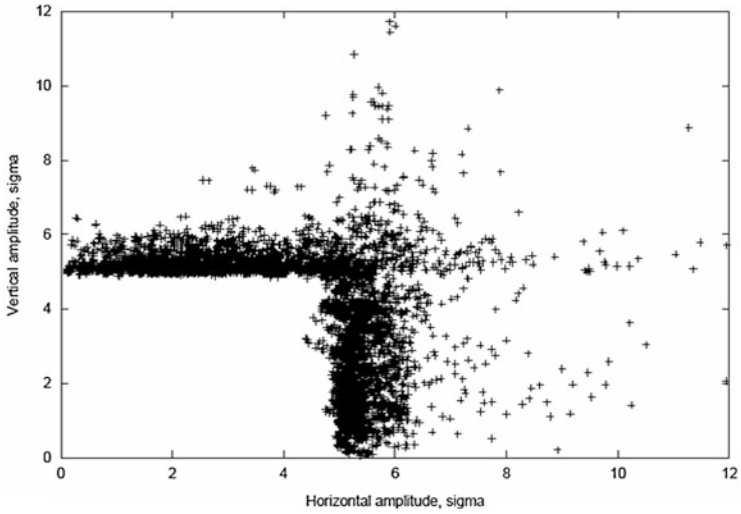

Fig. 6.15 Proton beam halo on a secondary collimator [27]

this collimator are presented by a vertical line in the transverse phase diagram (Fig. 6.14). Protons with a positive angle are intercepted by a D17(3) secondary collimator at the end of the D17 straight section. An A0 secondary proton collimator positioned outward and up of the circulating beam is intended to intercept the negative angle protons emitted from the primary collimator. A primary collimator D49 and secondary collimators E0(1) and F17(2) are used to deal with the protons with negative momentum deviations. Antiproton beam cleaning consists of primary collimators F49, F17(3) and secondary collimators D17(2), F48, F17(1) and E0(2).

Detailed STRUCT/MARS simulations assumed that halo particles first hit the primary collimator with a 1 to 3 μm impact parameter. On the next turns, the impact parameter—as a result of scattering—increases to about 0.3 mm. After the first interaction with a primary collimator, high amplitude particles are intercepted by the secondary collimators, but a large number of particles survive. Some fraction of the halo is not intercepted by a primary/secondary collimator pair and will interact with a primary collimator on the next turns. On average, halo protons interact with the primary collimator 2.2 times. Particles with the amplitudes less than 6σ are not intercepted by the secondary collimators and do survive for several tens of turns until they increase amplitude in the next interactions with the primary collimator. The tail of halo is extended above 6σ (Fig. 6.15). Large-amplitude particles, which escape from the cleaning system at the first turn, are able to circulate in the machine, before being captured by the collimators on the later turns. This defines the machine geometric aperture.

The calculations [22] have shown and later measurements confirmed that the inefficiency of the Tevatron collimation system defined as a leakage of halo protons from its components is $\sim 10^{-3}$. At the same time, the most critical function of the system in Run II has been identified as reduction of background rates in the collider

experiments. Beam loss in the B0 and D0 depends strongly on the secondary collimator offset with respect to the primary collimators. It has been shown in [28] that a part of the accelerator-related backgrounds in the D0 and CDF detectors is originated from the beam halo loss in the inner triplet region. The studies [29] have revealed that it is mainly due to beam-gas elastic scattering in the regions between the nearest to the IP secondary collimator and the corresponding inner triplet. This process will obviously increase the background rates. In addition to the optically small aperture at $\beta_{\max}$ location, the aperture restrictions in this area are the D0 forward detector's Roman pots placed at 8σ and the B0 Roman pots placed at 10σ at the entrance and exit of the beam separators. Note that the Roman pot systems had been removed in the middle of the Collider Run II. Thus, for the collider detectors, the above-defined inefficiency is not the whole story. The more appropriate definition of collimation inefficiency would be a ratio of backgrounds in the detectors with collimation to that without collimation. For the Tevatron Run II it is calculated as 6.7×10^{-3}, or a factor of 150 reduction of losses. The corresponding measurements are described below.

6.4.2 Collimation System Operation

The collimator hardware consists of a Motorola VME 162 processor and Advanced Controls System Corp. Step/Pac stepping motor drivers that interface to the VME processor [30]. LVDT's (linear voltage differential transformers) are used to read collimator positions. Figure 6.16 is the block diagram for the hardware controls for a single collimator.

The Collider II collimator halo removal system was designed with the capability of incorporating feedback into the motion of a collimator. The system uses two sources for feedback. The first source is feedback from a local beam loss monitor. Four standard Tevatron beam loss monitors and amplifiers are interfaced to the VME processor to provide loss monitor feedback. Two of these loss monitors are used to detect losses in the proton direction and two in the antiproton direction. Two loss monitors for each particle type are used to provide redundant loss monitor signals in case of failure during collimator movement. The second source of feedback comes from a beam intensity signal. A Fast Bunch Integrator system (see Chap. 9) is used to provide beam intensity signals for both proton and antiproton beams at a 360 Hz update rate. Feedback is accomplished by encoding proton and antiproton intensity signals onto the global machine data link (MDAT). The MDAT signal is decoded by each of the VME processors at a 720 Hz rate.

Processing the feedback internal to the VME is accomplished by sampling the loss monitor and/or beam intensity signal periodically while the collimator is moving. The smallest step the collimator can make is 25 μm. This minimum step takes 20 ms to complete. A wait step occurs after the move step to provide more flexibility to timing movements. During this step, loss monitor signals and/or beam intensity signals are sampled every 4 ms and are compared to a loss limit value or

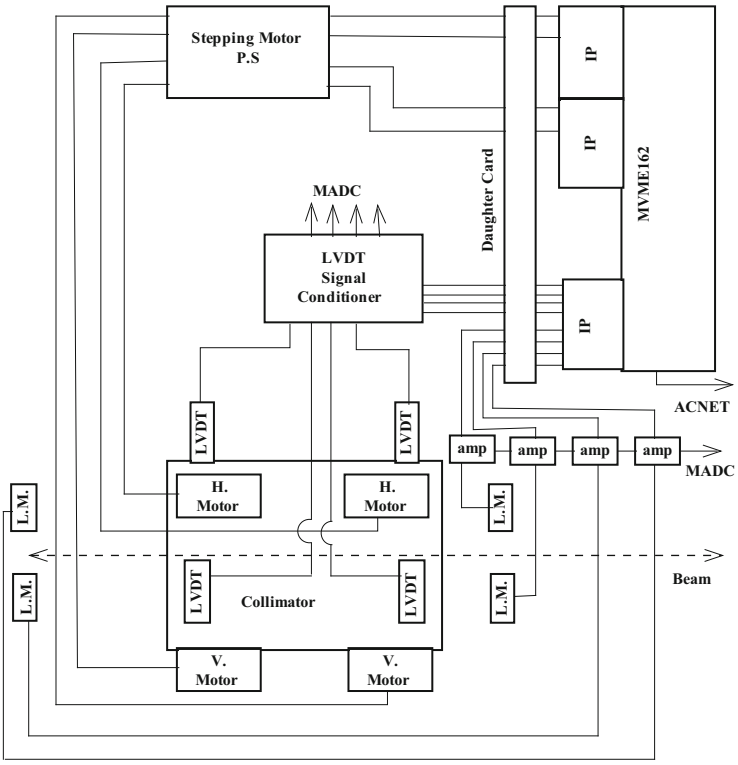

Fig. 6.16 Block diagram of the hardware controls for a single collimator [27]

beam intensity percentage allowed to be removed to decide if the collimator is to be halted for the next step. Each collimator VME frontend has 17 parameters that the user can change to specify details about feedback processing.

The halo removal system also utilizes software that allows global coordination of all 12 local collimator VME front ends. This global coordination software is called an open access client (OAC). An OAC is a central process that runs on a VAX (LINUX after control system change) and has controls hooks into the main Tevatron sequencer software [30]. The OAC employs a finite state machine that is configurable by the user to preprogram one or many collimators to complete a task on a transition of a state. For example, on the state "Goto injection positions" all collimator front ends are preprogrammed with local parameters that define their out of beam positions. The OAC owns a configurable matrix of states of the collimators and the user specifies which collimators are to move when the state is transitioned. Once the state is transitioned, all collimators will be moved back to their injection positions. There were 11 defined collimator states with names like: "Go to injection positions", "Begin halo removal scraping", and "Retract proton collimators". There is one special collimator state which is "Global Collimator Abort". A transition to

this state stops all 12 collimators immediately. Figure 6.16 is a block diagram of the OAC.

The halo removal process is conducted in the Tevatron at the flattop energy of 980 GeV after the proton and antiproton beams have been brought into collisions. This process is initiated by the Tevatron sequencer software. There are four sub-sequence operations that are necessary in order to complete the halo removal. (1) *Move Collimators to Initial Positions*—this sub-sequence moves all the collimators at 1.25 mm/s speed into the beam to the "half way" point to the beam. The motivation of this sub-sequence is to speed up the process. (2) *Intermediate Halo Removal*—here each set (proton and antiproton) of collimators and targets are moved together under beam loss monitor feedback until a small loss is detected and all collimators are stopped. This sub-sequence is also preformed in order to reduce the total amount of time the halo removal process takes. (3) *Perform Halo Removal*—each secondary collimator and target is moved serially into the beam. Secondary collimators are moved under loss monitor feedback with a step size of 0.025 mm until they reach the edge of the beam to shadow the losses by the primary collimator. After all secondary collimators are placed next to the beam, each target is moved under loss monitor and beam intensity feedback until 0.4 % of each beam (proton and antiproton) is removed. (4) *Retract Collimators for Store*—after targets and secondary collimators have reached their final assignment, they are retracted approximately 1 mm. This is the position they remain at for the duration of the store. This roughly leaves the targets and secondary collimators at the 5 and 6σ points as specified by the system design. The halo removal system is a necessary and integral part of Tevatron Collider operations. The halo removal system is completely automated and benefits operations with ease of use. The entire process takes as fast as 7 min. Figure 6.17 presents loss rates during the process of beam collimation early in store #8709 (May 2011).

A zero time in Fig. 6.17 corresponds to the moment when two 980-GeV beams are brought to collisions. Over the next six and a half minutes collimators sequentially approach the beams and scrape them. Horizontal position of one of the collimators (D49H) is shown in the bottom plot. One can see that the collimator moved very close to the beam twice—that is intentionally done to repeat the scraping procedure and guarantee lower loss rates afterward. The proton beam intensity on the upper plot shows a number of small drops due to the scraping. The bottom plot shows proton halo loss rate as measured by CDF detector and the antiproton loss rate measured by D0 detector. After the scraping is over—at about 7 min—the CDF detector luminosity monitor starts operation and reports maximum luminosity of about 430×10^{30} cm^{-2} s^{-1}. Note that compared to the first moments after the collisions are initiated, during the luminosity operation the proton halo loss rate drops by factor of 100 from 2–3 MHz to 20–30 kHz, while antiproton rate is down by a factor of 4–5 (from some 8–10 to 2 kHz).

The merit of halo removal efficiency is to simply record the proton and antiproton halo losses at CDF and D0 IPs before halo removal, and, then, to divide it by the same losses recorded at the completion of halo removal. Table 6.2 presents statistics of the reduction in the losses averaged over 100 stores in January–May 2011.

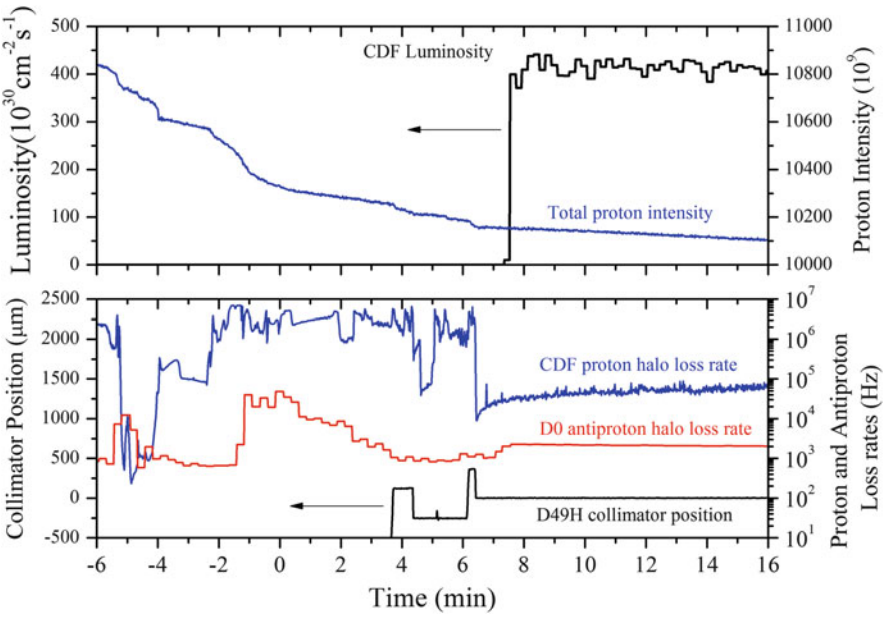

Fig. 6.17 Collimation process early in store #8709 (May 2011). *Upper plot* shows proton beam intensity and CDF luminosity. *Bottom plot* shows proton halo loss rate as measured by CDF detector, D0 antiproton loss rate and horizontal position of one of the collimators (D49H). Zero time corresponds to the moment when two beams are brought to collisions [27]

Table 6.2 Merit of halo removal efficiency (2010–2011)

Halo loss counter at CDF or D0 IP	Factor of reduction of halo losses after halo removal
CDF proton halo loss	112
CDF antiproton halo loss	80
D0 proton halo loss	13
D0 antiproton halo loss	19

One can see that the biggest reduction is seen in the CDF proton rate (over a factor of 100). The reduction in the D0 proton halo loss is relatively small, that can be attributed to the fact that for the proton direction the CDF Interaction Point acts as an additional collimator and, thus, reduces the proton halo losses at D0.

6.4.3 Abort Gap Beam Removal

Particles not captured by the Tevatron RF system, and, therefore, not synchronized with it, pose a threat since they can quench the superconducting magnets during acceleration or at beam abort [31]. The mechanisms of such uncaptured beam

generation are somewhat different at the injection (150 GeV) and top (980 GeV) energies. Coalescing in the Main Injector typically leaves a few percent of the 150 GeV beam particles outside RF buckets. These particles are transferred together with the main bunches to the Tevatron. In addition, the single IBS (the Touschek effect), diffusion due to multiple IBS, and phase and amplitude noise of the RF voltage, drive particles out of the RF buckets. This is exacerbated by the fact that after coalescing and injection, 95 % of the particles cover almost the entire RF bucket area. The uncaptured beam is lost at the very beginning of the Tevatron energy ramp. These particles are out-of-sync with the Tevatron RF accelerating system, so they do not gain energy and quickly ($<$1 s) spiral radially into the closest horizontal aperture. If the number of particles in the uncaptured beam is too large, the corresponding energy deposition results in a quench (loss of superconductivity) of the superconducting (SC) magnets and, consequently, terminates the high-energy physics store. At the injection energy, an instant loss of uncaptured beam equal to 3–7 % of the total intensity can lead to a quench depending on the spatial distribution of the losses around the machine circumference.

At the top energy, uncaptured beam generation is mostly due to the IBS and RF noise while infrequent occurrences of the longitudinal instabilities or trips of the RF power amplifiers can contribute large spills of particles to the uncaptured beam. Uncaptured beam particles are outside of the RF buckets, and therefore move longitudinally relative to the main bunches. Contrary to the situation at the injection energy of 150 GeV, when synchrotron radiation (SR) losses are practically negligible, 980 GeV protons and antiprotons lose about 9 eV/turn due to SR. For uncaptured beam particles, this energy loss is not being replenished by the RF system, so they slowly spiral radially inward and die on the collimators, which determine the tightest aperture in the Tevatron during collisions. The typical time for an uncaptured particle to reach the collimator is about 20 min.

The presence of the uncaptured beam is very dangerous not only for the collider elements but also for the high-energy physics particle detectors CDF and D0 as the abort gap particles generate unwanted background and can be kicked onto the detectors' components by the beam abort kickers. A number of ideas have been proposed for elimination of the uncaptured beam in the Tevatron. The TEL has been found to be the most effective. The advantages of the TELs are twofold: (1) an electron beam is in close proximity to the proton or antiproton orbits and generates a quite strong transverse kick; (2) the TELs possess short rise and fall times (~100 ns), so they can be easily adjusted to operate in a variety of different pulsing schemes. Another uncaptured beam removal method tested during machine studies was a transverse strip line kicker operating with a narrow noise bandwidth. The kicker signal was timed into the abort gap to diffuse uncaptured beam particles transversely. With the noise power limited by a 300 W amplifier, that method was found significantly less effective than using the TELs.

The TEL #1 and #2 were installed in the Tevatron in 2001 and 2006, respectively, for compensation of beam–beam effects (see Chap. 8, Sect. 8.3). In early 2002, it was found that TEL-1 can effectively remove uncaptured protons if timed into the abort gap and operated in a resonant excitation regime [31]. TEL-2 is also

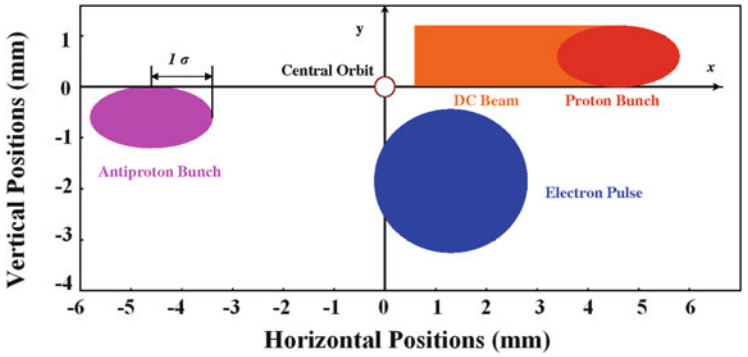

Fig. 6.18 The relative positions of the proton, antiproton, and electron beam during uncaptured beam removal [31]

able to function as an abort gap cleaner. For that, the electron beam pulse is synchronized to the abort gap and positioned near the proton beam orbit. Electric and magnetic forces due to the electron space charge produce a radial kick on high-energy protons depending on the separation d:

$$\Delta\theta = \mp\frac{1 \pm \beta_e}{\beta_e} \cdot \frac{2J_e L_e r_p}{e \cdot c \cdot \gamma_p} \cdot \begin{cases} \dfrac{d}{a}, & d < a, \\ \dfrac{a}{d}, & d > a, \end{cases} \tag{6.121}$$

where the sign reflects repulsion for antiprotons and attraction for protons, $\beta_e = v_e/c$ is the electron beam velocity, J_e and L_e are the electron beam current and the interaction length, a is the electron beam radius, r_p is the classical proton radius, and $\gamma_p = 1{,}044$ is the relativistic Lorentz factor for 980 GeV (anti)protons. The factor $1 \pm \beta_e$ reflects the fact that the contribution of the magnetic force is β_e times the electric force contribution and depends on the relative direction of the electron and proton velocities.

For 5 kV electrons with typical peak current of about 0.6 A and 5 mm away from the protons, the estimated kick is about 0.07 μrad. When the pulsing frequency of the TEL is near the proton beam resonant frequency, this beam–beam kick resonantly excites the betatron oscillations of the beam particles.

In the uncaptured beam removal operation, the TEL electron beam is placed 2–3 mm away from the proton beam orbit horizontally and about 1 mm down vertically as depicted in Fig. 6.18. For normal Tevatron operation, the fractional part of the tunes are $Q_x = 0.583$ and $Q_y = 0.579$ for horizontal and vertical planes respectively. These tunes are placed between the strong resonances at $4/7 \approx 0.5714$ and $3/5 = 0.6$. When an uncaptured particle loses energy due to synchrotron radiation, its horizontal orbit is changed proportionally to the lattice dispersion,

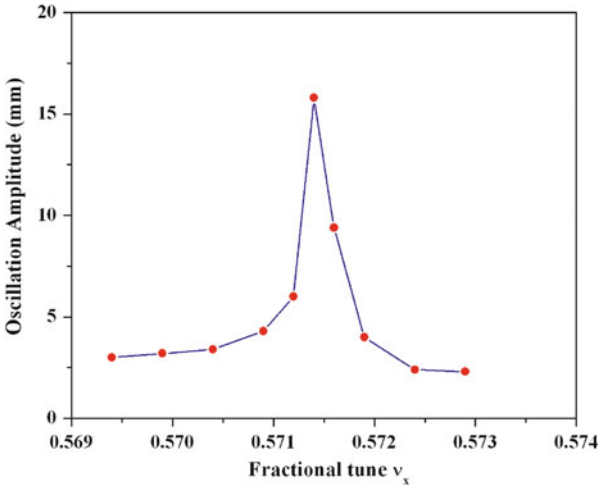

Fig. 6.19 Betatron oscillation amplitude of the particles driven by the TEL in vicinity of the $Q = 4/7$th resonance line (simulations) [31]

$x = D_x(\delta P/P)$, and its betatron tunes are changed due to the lattice chromaticity $Q'_{x,y} = dQ_{x,y}/(dP/P)$ so that

$$Q_{x,y} = Q^0_{x,y} + Q'_{x,y}\left(\frac{dp}{p_0}\right) + \Delta Q_{x,y}\left(x^2\right), \tag{6.122}$$

where the third term accounts for slight tune changes due to nonlinear magnetic fields. Typical operational chromaticities of the Tevatron at 980 GeV are set to $Q'_{x,y} \approx +(6\text{–}10)$, so the tune decreases with the energy loss. As the tune, driven by the TEL, approaches one of the resonant lines, the amplitude of the particle betatron oscillations grows, eventually exceeding a few millimeters until the particle is intercepted by the collimators. Figure 6.19 presents one set of the simulation results of the particle amplitude driven by the TEL in the vicinity of the `4/7th` resonance. The maximum amplitude is determined by the nonlinearity of the force due to the electron beam and the nonlinearity of the machine. Note that without the TEL, a particle would still be intercepted by a horizontal collimator after its orbit moved about 3 mm inward due to SR. The TEL simply drives it more quickly, preventing the accumulation of uncaptured beam.

The electron beam pulsing scheme is demonstrated in Fig. 6.20, where the green oscilloscope trace is the signal from the TEL Beam Position Monitor (BPM) pickup electrode and the blue trace is the total electron current. In the BPM signal, one can see three negative pulses representing the electron beam pulses in the 3 abort gaps whereas the 36 positive pulses are the proton bunch signals with the small negative adjacent antiproton bunch signals. The intensity of the antiproton bunches was ten times less than that of the proton bunches at the end of that particular store, so they appear only as very small spikes near the large proton bunches. During a typical HEP store, the train of three electron pulses is generated every seventh turn for the purpose of excitation of the 4/7 resonance for the most effective removal of the

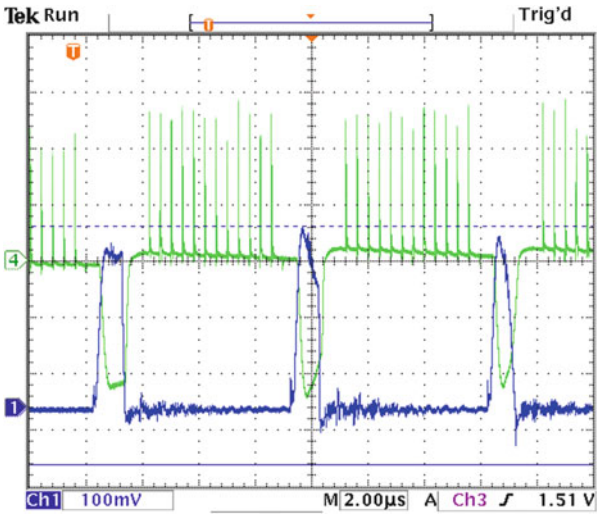

Fig. 6.20 Scope traces of the electron beam pulses (*blue*) and the TEL BPM signal showing electron, proton, and antiproton bunches (*green*). One division of the horizontal axis is 2 µs. About one Tevatron revolution period is shown

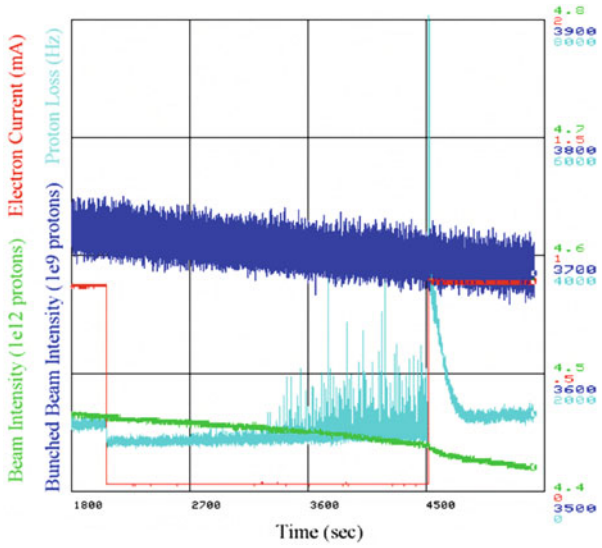

Fig. 6.21 Uncaptured beam accumulation and removal by TEL: the electron current was turned off and turned back on 40 min later again

uncaptured proton beam particles. The electron pulse width is about 1 µs and the peak amplitude is about 250 mA.

The uncaptured beam removal process was demonstrated in an experiment in which the TEL was turned off for about 40 min and then turned on again as shown in Fig. 6.21. The blue trace is the total bunched proton beam intensity measured by the Fast Bunch Integrator (see Chap. 9); the red trace is the average electron current measured at the TEL electron collector; the green trace is the total number of particles in the Tevatron as measured by DCCT; and the cyan trace is the abort gap proton beam loss rate measured by the CDF detector counters. After the TEL was

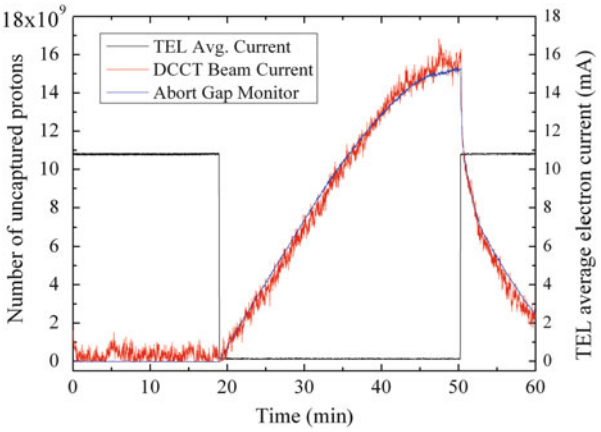

Fig. 6.22 Uncaptured beam accumulation and removal by the TEL. The *black line* represents the average electron current of the TEL; the *red line* is the uncaptured beam estimated from the DCCT measurement; the *blue line* is uncaptured beam in the abort gap measured by the AGM [29]

turned off, the abort gap loss rate was reduced by about 20 % but then started to grow. After about 20 min, the first spikes in the losses started to appear and grow higher. Notably, the bunched beam intensity loss rate (blue line) did not change, so the rate of particles escaping from the RF buckets was about constant. As soon as the TEL was turned on, a large increase in the abort gap losses and reduction of the total uncaptured beam intensity could be seen in Fig. 6.21. About 15×10^9 particles of the uncaptured beam in the abort gaps were removed by the TEL in about $\tau_{\mathrm{TEL}} = 3$ min and the abort gap loss rate went back to a smooth equilibrium baseline.

The calibration of the abort gap monitor (AGM—see details in Chap. 9) has been performed using the TEL as presented in Fig. 6.22. The TEL was turned off during a store (average electron current is shown in black) at about $t = 20$ min. Accumulation of the uncaptured beam started immediately and can be measured as an excess of the total uncaptured beam current with respect to its usual decay. The blue line in Fig. 6.22 shows the excess measured by the Tevatron DCCT, $\delta N_{\mathrm{DCCT}}(t) = N_{\mathrm{TEL\ on}}(t) - N_{\mathrm{decay\ fit\ TEL\ off}}(t)$. The abort gap uncaptured beam intensity measured by the AGM (red line) and the DCCT excess grow for about 30 min before reaching saturation at intensity of about 16×10^9 protons. Then the TEL was turned on resulting in the quick removal of the accumulated uncaptured beam from the abort gaps. This method of calibration of the AGM with respect to DCCT interferes with the collider operation resulting in higher losses (see Fig. 6.21 above and discussion), so this operation is performed only when required. The AGM is used for the routine monitoring of the uncaptured beam. The typical rms error of the uncaptured beam intensity measurement is about 0.01×10^9 protons for the AGM, and some 0.3×10^9 protons for the DCCT.

The amount of the uncaptured beam is determined by the rate of its generation and the removal time τ:

$$N_{\mathrm{DC}} = \left(\frac{dN_{\mathrm{bunched}}}{dt}\right) \times \tau. \tag{6.123}$$

The characteristic time needed for a 980 GeV particle to lose enough energy due to SR is about $\tau_{SR} = 20$ min, so the TEL reduces the uncaptured beam population by about one order of magnitude.

At injection energy, the synchrotron radiation of protons is negligible, so the TEL is the only means to control uncaptured beam. As noted above, one of the TELs is used routinely in the Tevatron operation for the purpose of uncaptured beam removal at 150 and 980 GeV. In 2007, the typical antiproton intensity increased to about a third of the proton intensity, and therefore the antiproton uncaptured beam accumulation started to pose an operational threat. An antiproton AGM, similar to the proton one, has been built and installed. By proper placement of the TEL electron beam between the proton beam and the antiproton beam (illustrated in Fig. 6.18), we are able to remove effectively both uncaptured protons and uncaptured antiprotons. In addition, we have explored the effectiveness of the uncaptured beam removal at several resonant excitation frequencies. For that, we have pulsed the TEL every 2nd, 3rd, 4th, 5th, 6th, and 7th turn. Reduction of the uncaptured beam intensity was observed at all of them, though usually the most effective was the every 7th turn pulsing when the Tevatron betatron tunes were close (slightly above) to $Q_{x,y} = 4/7 = 0.571$ or every 6th turn pulsing when tunes were closer to $Q_{x,y} = 7/12 = 0.583$.

6.4.4 Beam Halo Collimation by Bent Crystals

Since the original suggestion of bent crystal channeling [32] there has been interest in exploiting the technique for accelerator extraction [33] and, later, collimation [34]. Luminosity-driven channeling extraction was observed for the first time in a 900 GeV study at the Fermilab Tevatron during Collider Run I [35]. The experiment, Fermilab E853, demonstrated that useful TeV-level beams can be extracted from a superconducting accelerator during high luminosity collider operations without unduly affecting the background at the collider detectors. Multipass extraction was found to increase the efficiency of the process significantly. The beam extraction efficiency was about 25 %. Studies of time-dependent effects found that the turn-to-turn structure was governed mainly by accelerator beam dynamics. Based on the results of the E853 experiment, it was concluded that it is feasible to construct a parasitic 5–10 MHz proton beam from the Tevatron collider [36].

An efficient beam collimation system is mandatory for any collider or high-power accelerator. The Tevatron Run II approach has been to use a two-stage collimation system in which a primary collimator is employed to increase the betatron oscillation amplitudes of the halo particles, thereby increasing their impact parameters on secondary collimators (see preceding section). A bent crystal can coherently direct channeled halo particles deeper into a nearby secondary absorber. This approach has the potential of reducing beam losses in critical locations and, consequently, to reduce the radiation load to the downstream superconducting magnets.

There are several processes which can take place during the passage of protons through the crystals: (a) amorphous scattering of the primary beam; (b) channeling; (c) dechanneling due to scattering in the bulk of the crystal; (d) "volume reflection" off the bent planes; and (e) "volume capture" of initially unchanneled particles into the channeling regime after scattering inside the crystal. The particle can be captured in the channeling regime, oscillating between two neighboring planes if it enters within crystal's angular acceptance of:

$$\theta < \theta_c = \sqrt{\frac{2U_0}{pc}}, \tag{6.124}$$

where p is the particle momentum and U_0 is the crystal's planar potential well depth. The critical angle θ_c is about 7 μrad for 980 GeV/c protons in the (110) silicon crystal orientation. When the crystal is bent, particles still can be channeled (and thus deflected) if the bend radius R is greater than a critical value $R_c = pv/eE_m$, where E_m is the maximum strength of the electric field in the channel, about 6 GV/cm for the (110) silicon crystal orientation. That yields $R_c \approx 1.6$ m for 980 GeV/c protons. Bending of the crystal decreases the critical channeling angle, the capture probability of particles into the channeling regime and the dechanneling length [33]. If the particle momentum is not within the critical angle but has a tangency point with the bent planes within the crystal volume, almost all particles are deflected to the opposite direction with respect to the crystal bending. The effect is called the volume reflection (VR) [33] and it has very wide angular acceptance equal to the crystal bend angle (of the order of hundreds of microradians compared to several microradians of the channeling acceptance). The drawback of the volume reflection regime is that the deflection angle is small, approximately $(1.5–2) \times \theta_c$. However, this can be overcome by using a sequence of several precisely aligned bent crystals, so that the total deflection angle is proportionally larger.

In the Tevatron beam crystal collimation experiment T980 [37–39] both single crystals (for vertical and horizontal deflection) and multi-strip crystal assemblies (for vertical multiple VR) have been used. Collimation of circulating beams is very different from bent crystal experiments with extracted beams [40] because of smaller initial "impact parameters" and the possibility of interplay of different effects. In an accelerator such as the Tevatron several phenomena determine the impact parameter (the depth of the particle penetration at the first interaction with the crystal). These include four diffusion and two orbit processes. The first two diffusion processes are scattering on the residual gas and noise in magnetic field. They produce the amplitude growth of about 4 nm/√turn. The RF noise results in the diffusion rate of ~12 nm/√turn (hor.) and ~1 nm/√turn (vert.). The beam diffusion due to beam–beam or other nonlinear effects can produce up to ~10–40 nm/√turn; and, important only for the uncaptured DC beam particles located in the abort gaps, the diffusion due to the excitation by the TEL results in ~7 μm/turn. For interaction with amorphous targets, the diffusion rates are ~200 μm/√turn for a 5 mm length of amorphous silicon, and about ~1,200 μm/√turn for a 5 mm tungsten primary target. The two orbit processes

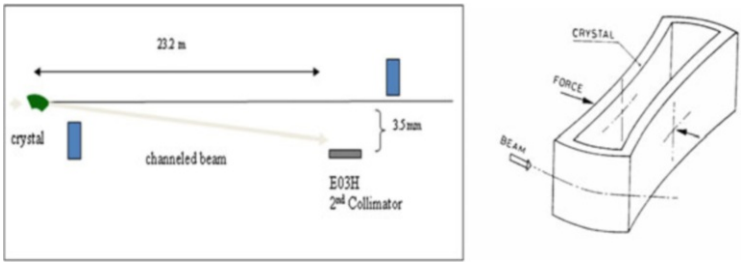

Fig. 6.23 (**a**) (*Left*) General layout of the T980 experiment at E0, the straight section used for the crystal collimation test; (**b**) (*right*) "O"-shape crystal prepared by Petersburg Nuclear Phusics Institute and used at RHIC and Tevatron. The length along the beam is 5 mm

are: transverse orbit oscillations with amplitude of ~20 μm and frequencies of ~15 Hz (i.e., with period equal to some 3,000 revolutions in the Tevatron—see Chap. 2, Sect. 2.4) and synchrotron motion of particles near the boundary of the RF bucket with amplitudes of ~1 mm (hor) and ~70 μm (vert) at ~35 Hz (1,300 turns). The orbit motion due to synchrotron oscillations occurs at nonzero dispersion locations, e.g., at the E03 location of the T980 experiment crystals where the dispersion is about $D_x = 2$ m horizontally and 18 cm vertically. The resulting impact parameters are estimated to be of the order of 0.2–1 μm for transverse halo particles and ~10–30 μm for the particles in the abort gaps which have leaked out of the RF buckets. All that makes the properties of the surface of the crystal (rather than the bulk of the crystal) pivotal for collimation (contrary to the extracted beam studies)—e.g., it's roughness or the miscut angle [40]. These processes are very hard to predict and simulate; hence, the T-980 experimental studies are of great importance for understanding the beam physics aspects and determining feasibility of the method for high energy colliders like the LHC and a Muon Collider.

Figure 6.23a shows a schematic of the T-980 experimental layout. During normal Tevatron operations, a 5-mm tungsten target scatters the proton beam halo into a 1.5-m long stainless steel secondary collimator E03, 50 m downstream of the target. For the bent crystal experiments, a goniometer containing single or multi-strip bent crystals is installed 23.7 m upstream of the E03 collimator. Scintillation counter telescopes detect secondary particles from protons interacting with the target and E03 collimator. An ionization chamber (beam loss monitor LE033) also detects secondary particles scattered from E03. A PIN diode telescope detects the secondaries scattered from the bent crystal. Under the above configuration, channeled beam is signaled by a reduction of the rate in the PIN telescope (channel LE033C) with attendant increases in the rates of the LE033 and E1 counters.

A modified BNL goniometer assembly [41] and an O-shaped 5-mm silicon crystal with a bending angle of 0.44 mrad were originally installed in the Tevatron downstream of the horizontal primary collimator in the fall of 2004. The crystal was set at $5.5\sigma_b \approx 2.5$ mm from the beam center and aligned in the halo by varying the crystal angle in steps of several μrad. The interaction probability in the 5 mm long crystal was monitored by the PIN diode and plotted as a function of the crystal angle as shown in

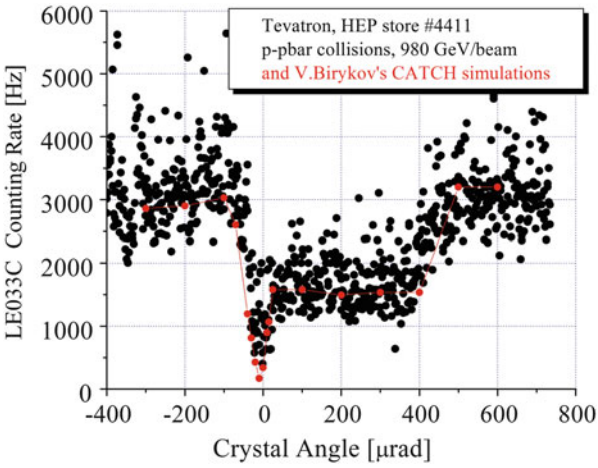

Fig. 6.24 Crystal angle (see text)

Fig. 6.24. A channeling dip is present at zero angle to the crystal's plane with a width of 22 ± 4 μrad (rms). The width of the channeling dip is a convolution of the beam divergence, the channeling critical angle, multipass channeling effects, and possible crystal distortions. It is difficult to do a deconvolution of the crystal angular scan to get the critical angle. However, the distribution is consistent with the beam divergence and 7 μrad channeling critical angle at 980 GeV. At the bottom of the dip the LE033C signal is 22 % of the signal at a random angular setting. This depth is a measure of the channeling efficiency and gives a channeling efficiency of $\eta_c = 78 \pm 12$ % including the effects of multiple passes. A shoulder extends 460 ± 20 μrad to the right of the channeling dip. This shoulder width is close to the expected magnitude of the crystal bend. The shoulder is a coherent crystal effect acting over the whole arc of the crystal bend due to volume reflection. Like channeling, the volume reflection diminishes nuclear interactions and thereby decreases the LE033 rate. The whole-arc efficiency, η_r, was 52 ± 12 %. The larger red dots and associated curve show the results of Biryukov's CATCH simulation [42] for the conditions in the Tevatron. Note that there are no free parameters in this simulation except average counting rate. Most impressive effect of using the bent crystal at the channeling angle instead of a tungsten primary collimator is the reduction of the CDF beam losses at the opposite side of the ring by a factor of two, in a good agreement with predictions [37].

In 2009 the 0.44-mrad bend O-shaped crystal in the horizontal goniometer was replaced with the new 0.36-mrad O-shaped one with negative 0.12-mrad miscut angle built by IHEP (Protvino), and a new vertical "push–pull"-type goniometer was installed 4-m upstream, housing two crystals—the multiple (eight) strip crystal from IHEP and the old 0.44 mrad O-shaped crystal, so that there were crystals for collimation in both vertical and horizontal planes. Since then crystal collimation has been routinely employed during many collider stores. Additional beam instrumentation was added. Fast automatic insertion of the crystals has been implemented. A vertical multi-strip crystal system has been successfully tested and both multiple-VR beam at the E03 collimator and channeled beam at the F17

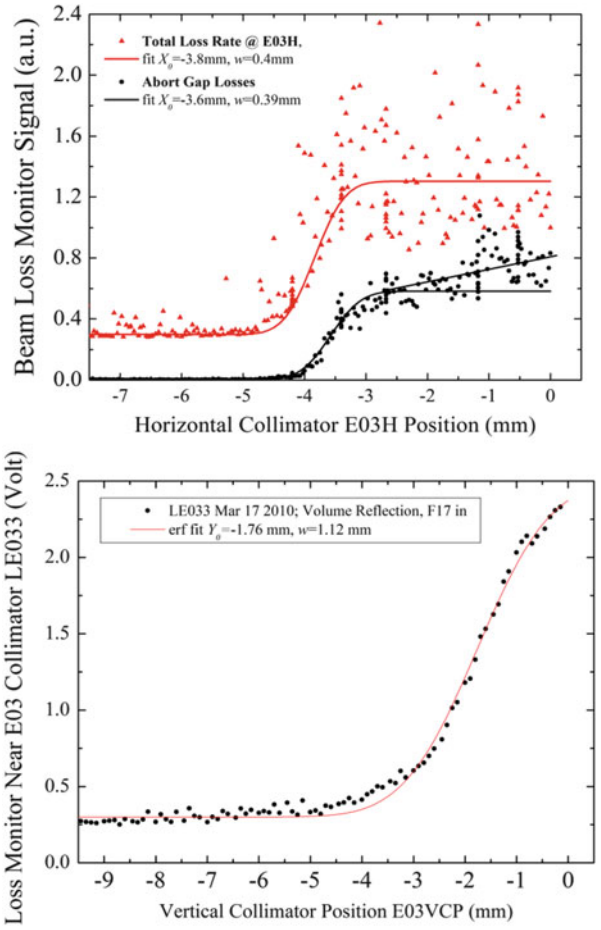

Fig. 6.25 Collimator scan with crystal set at: (**a**) (*top*) the channeling angle; (**b**) (*bottom*) Collimator scan with 8-strip vertical crystal set at the VR angle. *Solid lines* are for "erf" fits of the data [27]

collimator some 1 km downstream of the E03 have been observed. A reduction of ring wide losses was reproducibly obtained along with local loss effects on the collimator due to crystal channeling and VR. The first ever study of two plane crystal collimation was also conducted.

To measure the deflection of the channeled (or VR) particles once the crystal angle is set to the channeling (or VR) peak the position of an appropriate collimator can be slowly scanned, starting from a completely retracted position and moving toward the beam edge. An example of such a scan is shown in Fig. 6.25a for horizontally deflected channeled protons at the E03H collimator. The curves show the total measured loss rate (red dots) as well as the counting rate synchronized to the abort gaps only (black dots). There are three distinct regions: (a) a region of negligible losses, where the collimator does not intercept any beam; (b) a steep increase in the losses, where the collimator intercepts the channeled beam; (c) a region where the losses increase slowly: the collimator is additionally intercepting

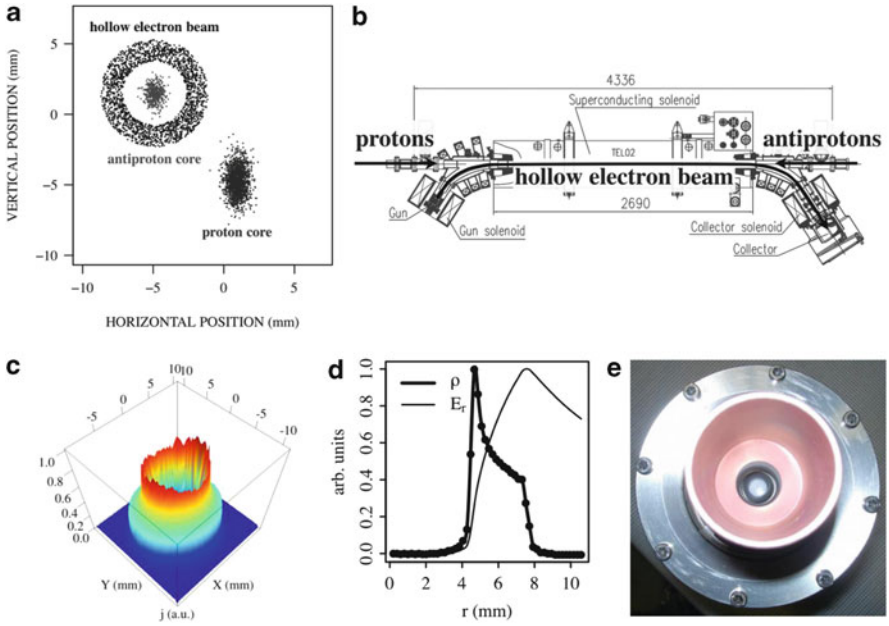

Fig. 6.26 Hollow electron beam collimator: (**a**) transverse beam layout; (**b**) top view of the beams in the Tevatron; (**c**) measured current profile; (**d**) measured charge density ρ and calculated radial electric field E_r; (**e**) photograph of the electron gun [27]

de-channeled and amorphous scattered particles. Both abort gap and total loss signals show a small deflection angle of (3.6–3.8)mm/24 m = 150–160 μrad instead of the expected 360 μrad. Such a difference can either be attributed to the effect of the "miscut angle" [38] or be due to non-ideal crystal surface that becomes important at the very small impact parameters. The angular spread in the channeled beam is about of 0.4 mm/24 m = 17 μrad rms that is larger than the channeling acceptance of $2 \times \theta_c = 13.4$ μrad. A similar scan of the VR beam made with the E03 vertical collimator presented in Fig. 6.25b shows the beam at 1.76 mm/28 m = 63 μrad, i.e., approximately where it is supposed to be, and about 40 μrad rms wide [39].

6.4.5 *Hollow Electron Beam Collimator*

The hollow electron beam collimator (HEBC) is a novel concept of controlled halo removal for intense high-energy hadron beams in storage rings and colliders [43, 44]. It is based on the interaction of the circulating beam with a 5-keV, magnetically confined, pulsed hollow electron beam in a 2-m-long section of the ring. The electrons enclose the circulating beam, kicking halo particles transversely and leaving the beam core unperturbed (Fig. 6.26a, b). By acting as a tunable

diffusion enhancer but not as a hard aperture limitation, the HEBC extends conventional collimation systems beyond the intensity limits imposed by tolerable losses. The concept was tested experimentally at the Tevatron between October 2010 and September 2011. It represents a promising option for scraping high-power beams in the Large Hadron Collider.

In high-power hadron machines, conventional two-stage collimation systems offer robust shielding of sensitive components and are very efficient in reducing beam-related backgrounds at the experiments. However, they have limitations. The minimum distance between the collimator and the beam axis is limited by instantaneous loss rates (especially as jaws are moved inward), radiation damage, and by the electromagnetic impedance of the device. Moreover, beam jitter, caused by ground motion and other vibrations and only partially mitigated by active orbit feedback, can cause periodic bursts of losses at aperture restrictions. The HEBC addresses these limitations, emerging as a viable complement to conventional systems.

In the TEL, the electron beam is generated by a pulsed 5-kV electron gun and transported with strong axial magnetic fields. Its size in the interaction region is controlled by varying the ratio between the magnetic fields in the main solenoid and in the gun solenoid. Halo particles experience nonlinear transverse kicks and are driven towards the collimators. If the hollow current distribution is axially symmetric, there are no electric or magnetic fields inside and the beam core is unperturbed. A magnetically confined electron beam is stiff, and experiments with electron lenses showed that it can be placed very close to and even overlap with the circulating beam. Another advantage is that, contrary to conventional systems, no nuclear breakup is generated in the case of ion collimation. In a setup similar to that of the TEL, with a peak current of 1 A, an overlap length of 2 m, and a hole radius of 3 mm, the corresponding radial kick is 0.3 μrad for 980-GeV antiprotons. The intensity of the transverse kicks is small and tunable: the device acts more like a soft scraper or a diffusion enhancer, rather than a hard aperture limitation. Because the kicks are not random in space or time, resonant excitation is possible if faster removal is desired.

Analytical expressions for the current distribution were used to estimate the effectiveness of the HEBC on a proton beam. They were included in tracking codes such as STRUCT [23], Lifetrac [45], and SixTrack [46] to follow core and halo particles as they propagate in the machine lattice. These codes are complementary in their treatment of apertures, field nonlinearities, and beam–beam interactions. Preliminary simulations suggested that effects would be observable and that measurements are compatible with normal collider operations [47, 48].

A 15-mm-diameter hollow electron gun was designed and built (Fig. 6.26c–e) [49, 50]. It is based on a tungsten dispenser cathode with a 9-mm-diameter hole bored through the axis of its convex surface. The peak current delivered by this gun is 1.1 A at 5 kV. The current density profile was measured on a test stand by recording the current through a pinhole in the collector while changing the position of the beam in small steps. The gun was installed in one of the TEL-2 in

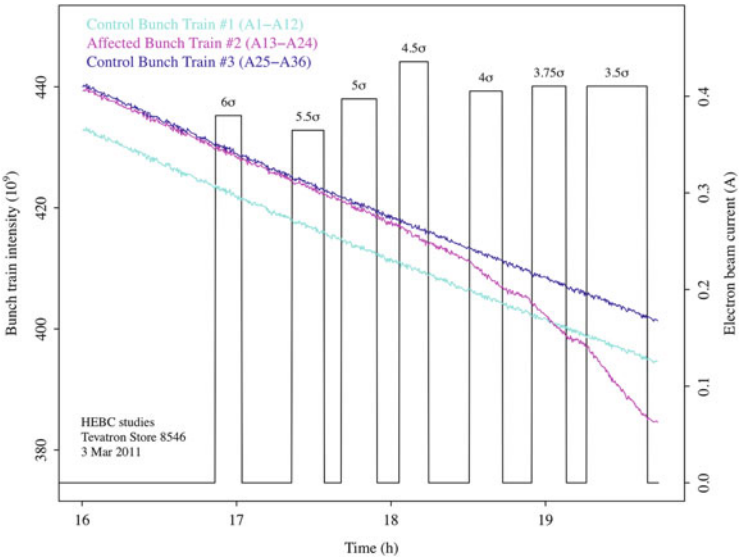

Fig. 6.27 Scraping effect of the hollow electron beam acting on one antiproton bunch train (*magenta*) at the end of a collider store. The intensities of the two control trains are shown in *cyan* and *blue*. The electron beam current (*black trace*) was turned on and off several times with different values of the hole radius, from $6\sigma_y$ to $3.5\sigma_y$ [27]

August 2010. The pulsed electron beam could be synchronized with practically any bunch or group of bunches.

The behavior of the device and the response of the circulating beams were measured for different beam currents, relative alignments, hole sizes, pulsing patterns, and collimator system configurations. Preliminary results were presented in [51, 52]. Here, we discuss a few representative experiments illustrating the main effects of the electron beam acting on antiproton bunches. Antiprotons were chosen for two main reasons: their smaller transverse emittances (achieved by stochastic and electron cooling in the Antiproton Source accelerators) made it possible to probe a wider range of confining fields and hole sizes; and the betatron phase advance between the electron lens and the absorbers was more favorable for antiproton collimation.

The particle removal rate was measured by comparing bunches affected by the electron lens with other control bunches. In the experiment described in Fig. 6.27, the electron lens was aligned and synchronized with the second antiproton bunch train, and then turned on and off several times at the end of a collider store. The electron beam current was about 0.4 A and the radius of the hole was varied between $6\sigma_y$ and $3.5\sigma_y$, with $\sigma_y = 0.57$ mm being the vertical rms beam size. The black trace is the electron-lens current. One can clearly see the smooth scraping effect. The corresponding removal rates are of a few percent per hour.

There is a concern related to adverse effects of hollow beam on the core of the circulating beam, because an asymmetry in the gun emission results in that the

beam in the overlap region is not a perfect hollow cylinder. The asymmetry is amplified by evolution of electron beam distribution under space its charge, and by the bends in the transport system. The problem was approached from several points of view. First, one can see in Fig. 6.27 that no decrease in intensity was observed with large hole sizes, when the hollow beam was shadowed by the primary collimators. This implies that the circulating beam was not significantly affected by the hollow electron beam surrounding it, and that the effect on the beam intensity of residual fields near the axis was negligible. Second, we observed no difference in the emittance growth for the affected bunches. If there was an emittance growth produced by the electron beam, it was much smaller than that driven by other two main factors, namely IBS and beam–beam interactions. The effect of halo removal can also be observed by comparing beam scraping with the corresponding decrease in luminosity. The luminosity is proportional to the product of antiproton and proton bunch populations, and inversely proportional to the overlap area. If antiprotons are removed uniformly and the other factors are unchanged, luminosity should decrease by the same relative amount. If the hollow beam causes emittance growth or proton loss, luminosity should decrease even more. A smaller relative change in luminosity was observed, which is a clear indication of halo scraping. Also, the ratio between luminosity decay rates and intensity decay rates increased with decreasing hole size. Finally, one can attempt to directly measure the particle removal rate as a function of amplitude. This was done with collimator scans. A primary antiproton collimator was moved vertically in 50-μm steps towards the beam axis. All other collimators were retracted. The corresponding beam losses and decay rates were recorded. Particles were removed from the affected bunch train, but as soon as the primary collimator shadowed the electron beam, eliminating the halo at those amplitudes, the relative intensity decay rate of the affected bunch train went back to the value it had when the lens was off. Even with a hole size of $3.5\sigma_y$, the effects of residual fields on the core appeared to be negligible. The time evolution of losses during a collimator scan was also used to measure changes in diffusion rate as a function of amplitude, using an extended version of the technique presented in [26, 53].

Another observation was that the hollow electron lens mitigated the effects of beam jitter. In the Tevatron, beams oscillate coherently at low frequencies (from sub-Hz to a few Hz) with amplitudes of a few tens of microns, due to mechanical vibrations and ground motion. This causes periodic bursts of losses at aperture restrictions, with peaks exceeding a few times the average loss rate. When the collimators are moved inward, these loss spikes can cause quenches in the superconducting magnets or damage electronic components. In March 2011, to measure the loss spikes and the effects of the hollow electron beam, scintillator paddles were installed downstream of one of the antiproton secondary collimators (F48). These loss monitors could be gated to individual bunch trains. It was observed that losses from the two control trains were completely correlated, and that their frequency spectra showed strong peaks at 0.39 Hz and its harmonics (corresponding to the acceleration cycle of the Main Injector) and at 4.6 Hz (mechanical vibrations from the Central Helium Liquefier). The electron lens

suppressed these peaks and eliminated correlations with the other trains. This can be interpreted as a reduction in the population of the beam tails. Note that it adversely affects the beam stability reducing the Landau damping for the affected bunches.

Losses generated by the electron lens were mostly deposited in the collimators, with small changes in the loss observed by the experiments. Alignment of the beams was done manually, with a setup time of about 15 min. Alignment is crucial for HEBC operation, and the procedures based on the electron-lens beam-position monitors were found to be reliable in spite of the different time structure of the electron and (anti)proton pulses. No instabilities or emittance growth were observed over the course of several hours at nominal antiproton intensities (10^{11} particles/bunch) and electron beam currents up to 1 A in confining fields above 1 T in the main solenoid. Most of the studies were done parasitically during regular collider stores.

Experiments at the Tevatron showed that the HEBC is a viable option for scraping high-power beams in storage rings and colliders. Its applicability to the LHC is under study. To make the device more versatile, larger cathodes and higher electron beam currents appear to be feasible, and experimental tests in this direction are planned.

6.5 Luminosity Evolution Model

6.5.1 Longitudinal Dynamics and Particle Loss from RF Bucket

While colliding at the top energy, the Tevatron proton and antiproton bunches lose their intensities as particles escape stable RF buckets. That occurs mostly due to the IBS and RF noise while infrequent occurrences of the longitudinal instabilities or trips of the RF power amplifiers can contribute large spills of particles to the uncaptured beam. Uncaptured beam particles are outside of the RF buckets, and therefore, move longitudinally relative to the main bunches, lose about 9 eV/turn due to the synchrotron radiation (SR), slowly spiral radially inward and die on the collimators, which determine the tightest aperture in the Tevatron during collisions. The typical time for a particle between its escape from the RF bucket and its reach of a collimator is about 20 min. The TEL operating in the abort cleaning regime (see Sect. 6.4.3) reduces the removal time of uncaptured beam from 20 min to about 2 min, thereby significantly reducing the particle population in the abort gap. That resulted in complete elimination of the quenches related to the uncaptured beam [31].

In the case of single harmonic RF, a particle phase trajectory in the longitudinal phase space (see Fig. 6.28) is described by the following equation [54]:

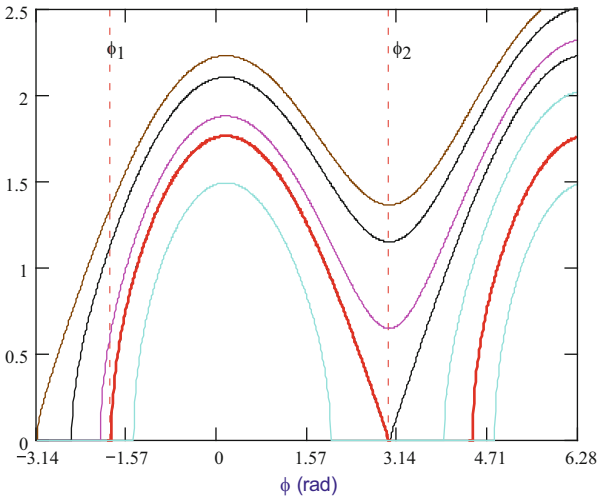

Fig. 6.28 Upper half of phase space trajectories in the vicinity of the separatrix (*red line*) for $\varphi_0 = 0.15$. Momentum spread (*vertical axis*) is presented in units of $(\eta h/Q_s)\ \Delta p/p_0$

$$\left(\frac{\Delta p}{p_0}\right)^2 = \frac{2Q_s^2}{\eta^2 h^2}(\cos\varphi - \cos\varphi_m + (\varphi - \phi_m)\sin\phi_0), \tag{6.125}$$

where $\Delta p/p_0$ is the relative particle momentum deviation, η is the slip factor, h is the harmonic number, Q_s is the synchrotron tune, ϕ is the RF phase, φ_0 is the accelerating phase, and φ_m determines the boundary of phase space trajectory. In the stationary state φ_0 is determined by particle energy loss due to synchrotron radiation eV_{SR}: $\sin\varphi_0 = V_{SR}/V_{RF}$. The SR radiation damping is neglected in Eq. (6.125) since the damping time is much longer than the store duration.

The outermost orbit, called the separatrix, determines the boundary of the RF bucket:

$$\left(\frac{\Delta p}{p_0}\right)^2 = \frac{2Q_s^2}{\eta^2 h^2}(\cos\varphi + \cos\varphi_0 + (\varphi - \pi + \varphi_0)\sin\phi_0). \tag{6.126}$$

If the equilibrium phase ϕ_0 is small, $\varphi_0 \ll 1$, the separatrix boundaries in the RF phase are:

$$\begin{aligned} \varphi_1 &\approx -\pi + \sqrt{4\pi\varphi_0} - \varphi_0, \\ \varphi_2 &= \pi - \varphi_0. \end{aligned} \tag{6.127}$$

As an example Fig. 6.28 presents the phase space trajectories for $\varphi_0 = 0.15$. The accelerating phase is much smaller for Tevatron at collisions: $\varphi_0 \approx 10^{-11}$, $\varphi_1 \approx -\pi + 10^{-5}$ and $\varphi_2 \approx \pi - 10^{-11}$. Thus, the Tevatron RF buckets are separated by a gap of $\sim 10^{-5}$ rad. A particle with initial momentum above the RF bucket boundary is decelerated by energy loss due to SR and eventually passes through a gap between buckets to the lower momentum side where it is decelerated to the nearest apertures limiting the beam energy spread.

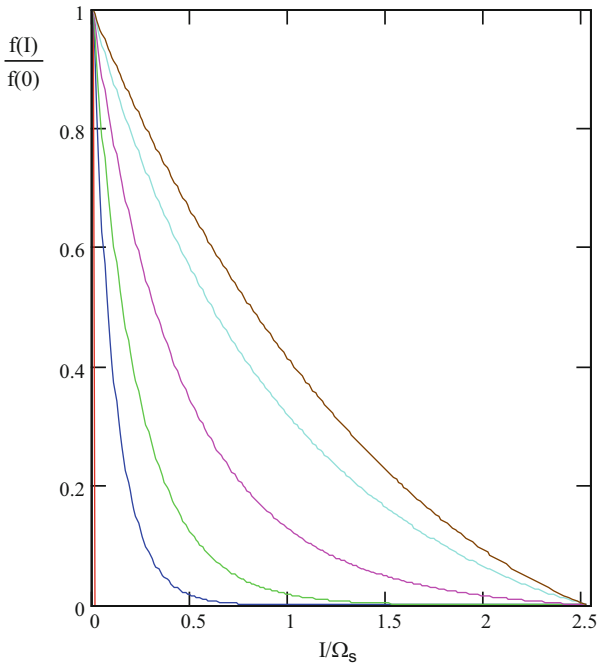

Fig. 6.29 Dependence of the distribution function on time for $Dt/\Omega_s{}^2 = 0$, 0.125, 0.25, 0.5, 1 and asymptotic at $t \to \infty$

6.5.2 *Longitudinal Diffusion and Particle Loss*

There are three major mechanisms creating the uncaptured beam. They are the diffusion due to amplitude and phase RF noises (see, e.g., [55]), multiple IBS and single IBS (Touschek effect) [56]. The RF bucket size at injection is 4.4 eV. Measurement showed that it is completely filled at the injection. The bucket size grows in the course of acceleration while the longitudinal emittance remains the same. At the acceleration end the bucket size reaches 11 eV s. Acceleration is sufficiently fast and therefore immediately after acceleration the bunch tails are negligible and the bunch occupies the same phase space as at injection. In the absence of tails the single IBS is the only mechanism for longitudinal particle loss. Shortly after acceleration the diffusion due to IBS and RF noise creates tails in the distribution function and results in additional beam loss, which significantly exceeds the loss due to single IBS (see, e.g., [57]). Therefore, in the following analysis we neglect the single IBS.

Figure 6.29 presents a numerical solution of diffusion equation (6.74) assuming (1) constant diffusion, $D(I) = D_0$, as a zero-order approximation, (2) the initial distribution being a δ-function, $f_0(I) = \delta(I)$, and (3) the boundary condition $f(I_b) = 0$ at the RF bucket boundary with $I_b = 8\Omega_s/\pi$. Figure 6.30 presents the corresponding beam intensity, rms momentum spread, and rms bunch length.

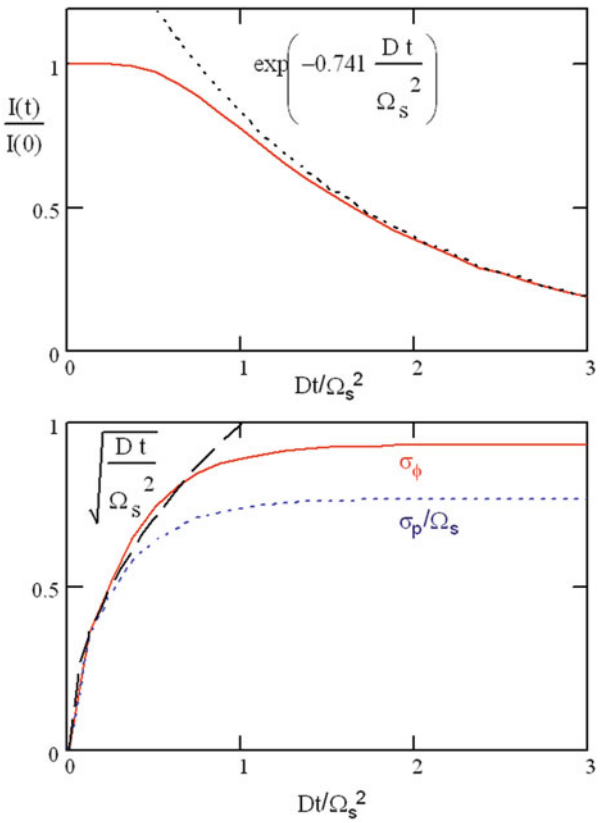

Fig. 6.30 Time dependence of beam intensity (*top*) and rms bunch length and momentum spread (*bottom*)

Initially, the bunch length and the momentum spread grow proportionally to $\sqrt{t}$ and the distribution function is close to the Gaussian distribution, $f(I,t) \propto (\Omega_s/Dt)\exp(-I\Omega_s/Dt)$. However when the bunch length becomes comparable to the bucket length, the non-quadratic behavior of the potential results in the bunch-length growing faster than the momentum spread. Finally, the distribution function and, consequently, the bunch length and momentum spread approach their asymptotic values, and the intensity decays exponentially as $\sim\exp(-0.741\ Dt/\Omega_s^2)$.

The results of simulations yield the following approximate relationships between the bunch parameters:

$$\begin{aligned}
\sigma_s &\approx \Gamma_s \sigma_{\Delta p/p} \left(1 + \frac{1}{4}\left(\frac{2\sigma_{\Delta p/p}}{\Delta P/P|_{\text{sep}}}\right)^2 + \frac{1}{6}\left(\frac{2\sigma_{\Delta p/p}}{\Delta P/P|_{\text{sep}}}\right)^3\right), \\
\frac{1}{N}\frac{dN}{dt} &\approx \frac{2.425(2\pi\sigma_s)^7}{\lambda_{\text{RF}}{}^7 + 1.65(2\pi\sigma_s)^7}\frac{d\left(\sigma_\varphi{}^2\right)}{dt}\bigg|_{\text{LM}}, \\
\frac{d\left(\sigma_{\Delta p/p}{}^2\right)}{dt} &\approx \left(1 - \left(\frac{2\sigma_{\Delta p/p}}{0.765\Delta P/P|_{\text{sep}}}\right)^5\right)\frac{d\left(\sigma_{\Delta p/p}{}^2\right)}{dt}\bigg|_{\text{LM}},
\end{aligned} \tag{6.128}$$

where $\Delta P/P|_{\text{sep}}$ is the height of the RF bucket. The top equation accounts nonlinear dependence between the bunch length σ_s and the momentum spread $\sigma_{\Delta p/p}$ in the single harmonic RF bucket. The second and third equations account for appearing the particle loss from the bucket and the reduction in the momentum spread growth rate which occur when the bunch distribution achieves the bucket boundary.

6.5.3 Longitudinal Evolution Model

Numerous factors affect the Tevatron collider luminosity and its evolution in time. Each store is different and because of finite instrumentation accuracy it is practically impossible to state what was different or what came wrong for every particular store. Nevertheless the luminosity evolution is very similar for most of the stores. It is driven by some basic processes, which are not very sensitive to the details of distribution functions, and therefore the luminosity evolution can be described by comparatively simple parametric model [58] presented below. The model takes into account the major beam heating and particle loss mechanisms. They are (1) the emittance growth and the particle loss due to scattering on the residual gas, (2) the particle loss and the emittance growth due to scattering in IPs, (3) the transverse and longitudinal emittance growth due to IBS, (4) the bunch lengthening due to RF noise, and (5) the particle loss from the bucket due to heating of longitudinal degree of freedom. If the collider tunes are correctly chosen, the beam intensity is not too high, and the beams are well formed, then the beam–beam effects are not very important and the model describes the observed dynamics of beam parameters and the luminosity comparatively well. Detailed discussion of how the beam–beam effects and lattice nonlinearities interact with diffusion and how they can be incorporated into the model can be found in Chap. 8.

If aperture limitations are sufficiently large in comparison with the beam size ($A_{x,y} \geq 5\sigma_{x,y}$), then the multiple and single scattering on the residual gas atoms can be considered separately. In this case the single scattering causes the particle loss, while the multiple scattering causes the emittance growth.

The beam lifetime due to single scattering is described by the well-known formula [59]

Table 6.3 Gas composition used in the simulations

Gas	H_2	CO	N_2	C_2H_2	CH_4	CO_2	Ar
Pressure [nTorr]	1.05	0.18	0.09	0.075	0.015	0.09	0.15

$$\tau_{\text{scat}}{}^{-1} == \frac{2\pi c {r_{\text{p}}}^2}{\gamma^2\beta^3}\left(\sum_i Z_i(Z_i+1)\left(\frac{\overline{\beta_x n_i}}{\varepsilon_{mx}}+\frac{\overline{\beta_y n_i}}{\varepsilon_{my}}\right)\right)+\sum_i n_i\sigma_i c\beta, \tag{6.129}$$

where $\overline{\beta_{x,y}n_i} = \int \beta_{x,y}n_i ds/C$ are the average gas density weighted by beta-functions, $\varepsilon_{mx,my}$ are the horizontal and vertical acceptances, r_{p} is the proton classical radius, γ and β are the relativistic factors, the summing is performed over all residual gas species, and the averaging is performed over ring circumference. The first addend is related to the electromagnetic scattering and the second one to the strong interaction. Taking into account that the scattering angle due to strong interactions ($\theta \sim m_\pi c/p \approx 140$ μrad) significantly exceeds rms angles in the beam (~7 μrad) σ_i can be considered to be the total nuclear cross section with sufficiently good accuracy. At the collision energy of 980 GeV the beam lifetime is dominated by the strong interaction.

The emittance growth rate due to multiple scattering is closely related to the electromagnetic part of the single scattering lifetime and is determined by the following formula:

$$\frac{d\varepsilon_{x,y}}{dt} = \frac{2\pi c {r_{\text{p}}}^2}{\gamma^2\beta^3}\left(\sum_i \overline{\beta_{x,y}n_i} Z_i(Z_i+1)L_{\text{c}}\right), \tag{6.130}$$

where L_{c} is the Coulomb logarithm ($L_{\text{c}} \approx 9$). Table 6.3 presents the gas composition used in the model. Overall pressure was scaled to fit the measurement results.

Similar to the gas scattering the scattering in the interaction point (IP) can be separated into the single scattering due to strong interaction and the emittance growth due to electromagnetic scattering. The total $\overline{p}p$ cross section consists of two parts: the inelastic cross section of 60 mbarn and the elastic cross section of 15 mbarn at 1 TeV energy. All particles scattered inelastically are lost immediately, while as shown in [59] about 40 % of elastically scattered particles remain in the beam (within 3σ). That happens because the beta-functions in the IP are small and, consequently, particle angles are large; so that the scattering angles are comparable to the particle angles (~100 μrad). The total cross section of particle loss obtained by fitting of the observations to the model is equal to 69 mbarn which coincides well with expectations.

The emittance growth due to electromagnetic scattering in one IP is equal to:

$$\frac{d\varepsilon_{x,y}}{dt} = \frac{4r_p{}^2 N L_{bb} f_0}{\gamma^2\beta^3\sqrt{(\varepsilon_{px}+\varepsilon_{py})(\varepsilon_{ax}+\varepsilon_{ay})}}. \tag{6.131}$$

Here ε_{px}, ε_{py}, ε_{ax}, and ε_{ay} are the emittances for proton and antiproton beams, f_0 is the revolution frequency, L_{bb} is the Coulomb logarithm ($L_{bb} \approx 20$), and N is the number of particles in the counter-rotating bunch. For two IPs and present Tevatron parameters it yields the antiproton emittance growth rate of about 0.0015 mm mrad/h. Although emittance growth rate is almost negligible in comparison with gas scattering the nuclear absorption in the IP is the main mechanism for antiproton loss during collisions.

Another important diffusion mechanism is determined by IBS. For the Tevatron collider parameters the longitudinal energy spread in the beam frame is significantly smaller than the transverse ones (e.g., the ratio of longitudinal to transverse particle velocities in the beam frame is about $v_{\|}/v_{\perp} \approx 0.02$ at collision energy, and $v_{\|}/v_{\perp} \approx 0.15$ at injection energy). In this case comparatively simple IBS formulas presented in Eq. (6.54) can be used. Tevatron has sufficiently smooth lattice and therefore IBS can be described with good accuracy in the smooth approximation. In this case Eq. (6.54) can be rewritten as follows [58]:

$$\begin{bmatrix} d\sigma_{\Delta p/p}{}^2/dt \\ d\varepsilon_x/dt \\ d\varepsilon_y/dt \end{bmatrix} = \frac{r_p{}^2 c N L_c \Xi_{\|}(\overline{\theta}_x, \overline{\theta}_y)}{4\sqrt{2}\gamma^3\beta^3\overline{\sigma}_x\overline{\sigma}_y\sigma_s\sqrt{\overline{\theta}_x{}^2+\overline{\theta}_y{}^2}} \begin{bmatrix} 1 \\ \overline{A}_x(1-\kappa) \\ \overline{A}_x\kappa \end{bmatrix}, \tag{6.132}$$

where

$$\begin{aligned} \overline{\sigma}_x &= \sqrt{\varepsilon_x\overline{\beta}_y + \overline{D}_x{}^2\sigma_{\Delta p/p}{}^2}\ , \quad \overline{\sigma}_y = \sqrt{\varepsilon_y\overline{\beta}_y}\ , \\ \overline{\theta}_x &= \sqrt{\varepsilon_x/\overline{\beta}_x}\ , \qquad\qquad \overline{\theta}_y = \sqrt{\varepsilon_y/\overline{\beta}_y}\ . \end{aligned} \tag{6.133}$$

For Tevatron the averaged beta-functions, the dispersion and the horizontal motion invariant are: $\overline{\beta}_x = R/\nu_x = 49$ m, $\overline{\beta}_y = R/\nu_y = 49$ m, $\overline{D}_x = \int D_x ds/2\pi R = 2.84$ m, and $\overline{A}_x = \int A_x ds/2\pi R = 0.2$ m. To obtain Eq. (6.132) we neglected in variations of $\Psi(0,\theta_x,\theta_y)$ along the lattice in Eq. (6.54) and assumed that $\Psi(0,\theta_x,\theta_y) = 1$ and $\Psi_{x,y}(\theta_x,\theta_y) = 1$ (their accounting makes quite small correction), and we additionally introduced the coupling parameter κ which takes into account the redistribution of heating between horizontal and vertical degrees of freedom. An experimental value for κ is about 0.4. It is quite large and due to the strong coupling in Tevatron which additionally is amplified by the beam–beam interaction. To verify accuracy of the smooth approximation we performed averaging of Eq. (6.54) with Tevatron lattice parameters for the rms bunch length of 62 cm, zero coupling ($\kappa = 0$) and 1.6×10^{11} protons/bunch. It yielded the horizontal and longitudinal emittance growth lifetimes of

22.5 and 28.5 h, correspondingly. The use of smooth approximation yields 18.9 and 26.9 h. As one can see the difference is sufficiently small and therefore the smooth approximation has been used in the described below parametric model.

For Gaussian beams the luminosity of the collider is determined by the well-known formula:

$$L = \frac{f_0 N_\mathrm{b} N_\mathrm{p} N_\mathrm{a}}{2\pi\beta^* \sqrt{\left(\varepsilon_{\mathrm{p}x} + \varepsilon_{\mathrm{a}x}\right)\left(\varepsilon_{\mathrm{p}y} + \varepsilon_{\mathrm{a}y}\right)}} H\left(\frac{\sqrt{{\sigma_{sp}}^2 + {\sigma_{sp}}^2}}{\sqrt{2}\beta^*}\right), \tag{6.134}$$

where N_b is the number of bunches, N_p and N_a are the number of protons and antiprotons per bunch, β^* is the beta-function in the interaction point (IP), and $\varepsilon_{\mathrm{p}x}$, $\varepsilon_{\mathrm{p}y}$, $\varepsilon_{\mathrm{a}x}$, and $\varepsilon_{\mathrm{a}y}$ are the horizontal and vertical emittances for proton and antiproton beams. The hourglass factor $H(x)$ takes into account the finite value of the longitudinal bunch size. It is equal to:

$$H(x) = \frac{2}{\sqrt{\pi}} \int_0^\infty \frac{e^{-y^2}}{1 + x^2 y^2} dy \overset{x \le 3}{\to} \approx \frac{1}{\sqrt[3]{1 + 1.3x^2}}. \tag{6.135}$$

To describe the evolution of the luminosity we write a system of differential equations, which bounds up all basic parameters of the proton and antiproton beams:

$$\frac{d}{dt}\begin{bmatrix} \varepsilon_{\mathrm{p}x} \\ \varepsilon_{\mathrm{p}y} \\ {\sigma_{\mathrm{pp}}}^2 \\ N_\mathrm{p} \\ \varepsilon_{\mathrm{a}x} \\ \varepsilon_{\mathrm{a}y} \\ {\sigma_{\mathrm{pa}}}^2 \\ N_\mathrm{a} \end{bmatrix} = \begin{bmatrix} 2d\varepsilon_{\mathrm{p}x}/dt\big|_{\mathrm{BB}} + d\varepsilon_{\mathrm{p}x}/dt\big|_{\mathrm{IBS}} + d\varepsilon_{\mathrm{p}x}/dt\big|_{\mathrm{gas}} \\ 2d\varepsilon_{\mathrm{p}y}/dt\big|_{\mathrm{BB}} + d\varepsilon_{\mathrm{p}y}/dt\big|_{\mathrm{IBS}} + d\varepsilon_{\mathrm{p}y}/dt\big|_{\mathrm{gas}} \\ d{\sigma_{\mathrm{pp}}}^2/dt\big|_{\mathrm{total}} \\ -N_\mathrm{p}{\tau_{\mathrm{scat}}}^{-1} - dN_\mathrm{p}/dt\big|_{\mathrm{L}} - 2L\sigma_{\mathrm{p}\bar{\mathrm{p}}}/n_\mathrm{b} \\ 2d\varepsilon_{\mathrm{a}x}/dt\big|_{\mathrm{BB}} + d\varepsilon_{\mathrm{a}x}/dt\big|_{\mathrm{IBS}} + d\varepsilon_{\mathrm{a}x}/dt\big|_{\mathrm{gas}} \\ 2d\varepsilon_{\mathrm{a}y}/dt\big|_{\mathrm{BB}} + d\varepsilon_{\mathrm{a}y}/dt\big|_{\mathrm{IBS}} + d\varepsilon_{\mathrm{a}y}/dt\big|_{\mathrm{gas}} \\ d{\sigma_{\mathrm{pa}}}^2/dt\big|_{\mathrm{total}} \\ -N_\mathrm{a}{\tau_{\mathrm{scat}}}^{-1} - dN_\mathrm{a}/dt\big|_{\mathrm{L}} - 2L\sigma_{\mathrm{p}\bar{\mathrm{p}}}/n_\mathrm{b} \end{bmatrix}. \tag{6.136}$$

Here indices "p" and "a" denote protons and antiprotons, the derivatives $d\varepsilon/dt|_{\mathrm{BB}}$ are the emittance growth rates due to scattering in the IP determined by Eq. (6.131) (factor of 2 takes into account 2 IPs), the derivatives $d\varepsilon/dt|_{\mathrm{IBS}}$ are the emittance growth rates due to IBS determined by Eq. (6.132), the derivatives $d\varepsilon/dt|_{\mathrm{gas}}$ are the emittance growth rates due to multiple scattering on the residual gas determined by Eq. (6.130), the derivatives $d\sigma^2/dt|_{\mathrm{total}}$ are the momentum spread growth rates determined by Eq. (6.128), the derivatives $dN/dt|_{\mathrm{L}}$ are the particle loss rate from bucket determined by Eq. (6.128), and the addends $2L\sigma_{\mathrm{p}\bar{\mathrm{p}}}/n_\mathrm{b}$ determines particle loss in two collision points due to luminosity. We also took into account that the momentum spread growth rates used in Eq. (6.128) include contributions from the IBS and RF noise.

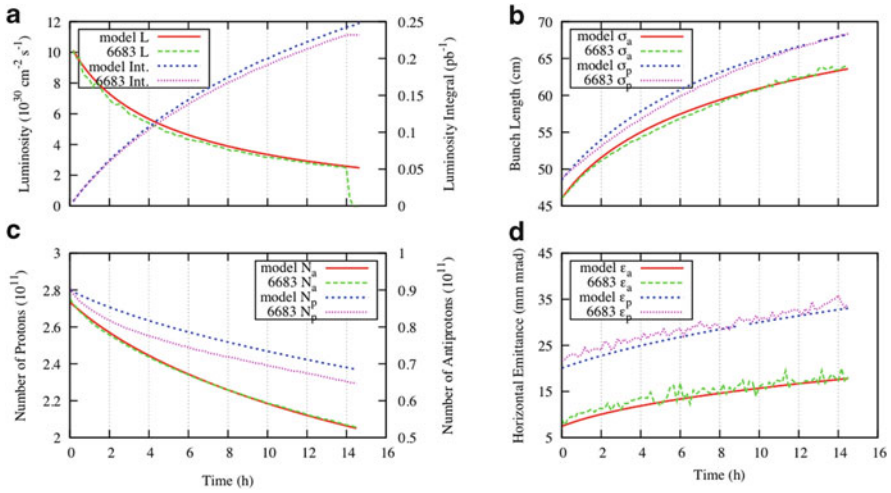

Fig. 6.31 Observed beam parameters in store 6683 compared to store analysis calculation (model). $L_0 = 3.5 \times 10^{32}$ cm^{-2} s^{-1}. (**a**) Single bunch luminosity and luminosity integral. (**b**) Intensity of proton bunch no. 6 and of antiproton bunch colliding with it (no. 13). (**c**) proton and antiproton rms bunch lengths. (**d**) proton and antiproton horizontal 95 % normalized bunch emittances

It is worth noting one more time that this model was able to predict evolution of the beam parameters in the case of weak beam–beam effects. When these effects are not small, it provides a reference for evaluation of their strength. We used that analysis on a store-by-store basis to monitor the machine performance in real time [60] because such calculations were very fast compared to a full numerical beam–beam simulation.

Figure 6.31 presents an example comparison of the evolution of beam parameters in an actual high luminosity store to the calculations. Note that there is no transverse emittance blow up in both beams, and the emittance growth is dominated by processes other than beam–beam interaction. The same is true for antiproton intensity and bunch length. The most pronounced difference between the observation and the model is seen in the proton intensity evolution. Beam–beam effects caused the proton lifetime degradation during the initial 2–3 h of the store until the proton beam–beam tune shift drops from 0.02 to 0.015. The corresponding loss of the luminosity integral was about 5 %.

The IBS model allows us to calculate the longitudinal beam loss rate in a typical Tevatron store (Fig. 6.32). The initial longitudinal loss rate is not equal to zero because of the Touschek effect. Later in the store, when more particles move closer to the boundaries of the RF buckets through diffusion processes, multiple IBS scattering starts to dominate over the single scattering effect. Note that for antiprotons, luminosity burning is the main loss contribution and the longitudinal loss due to IBS is much smaller than its total intensity loss rate. Normally about 40 % of antiprotons are “burnt” in the collisions due to elastic and inelastic interactions with protons.

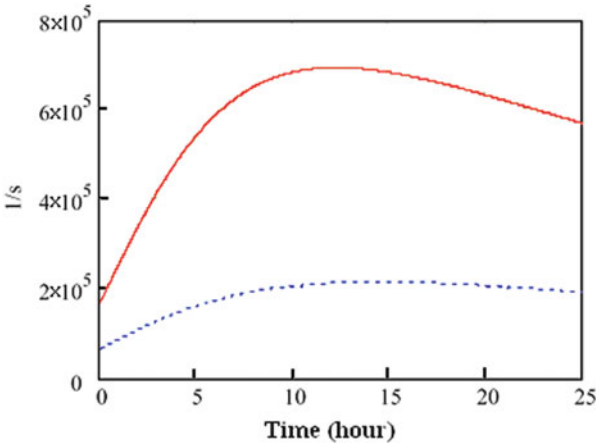

Fig. 6.32 Calculated longitudinal beam loss rate in unit of particles per second for a typical store using the IBS model, the *red curve* is for the proton bunch and the *blue dashed line* is for the antiproton bunch

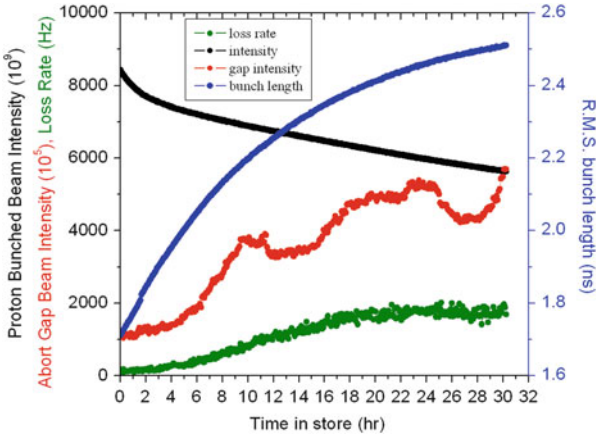

Fig. 6.33 Decay of proton bunch intensity (*black curve*) and growth of its length (*blue*) as well as abort gap loss rate at CDF detector (*green*) and proton abort gap intensity (*red*) in a typical HEP store (#5157, the TEL was on)

The calculated loss rate is in good qualitative agreement with the Tevatron observations. For example, Fig. 6.33 shows the evolution of the total proton bunched beam intensity, proton loss rate, proton rms bunch length, and the abort gap beam intensity during HEP store #5157. Bunch length and bunch intensity are reported from a wall current monitor (known as the "Sampled Bunch Display", described in Chap. 9). The loss rate is measured by gated scintillation counters on the CDF detector, which integrate over the time intervals corresponding to the abort gaps between the three proton bunch trains, while the simulation yields losses for the whole Tevatron storage ring.

References

1. E.M. Lifshitz, L.P. Pitaevskii, *Physical Kinetics*, vol. 10 (Pergamon Press, New York, 1981)
2. A. Piwinski, in *Proceedings of the 9th International Conference on High Energy Accelerators*, SLAC, Stanford, CA, USA, 1974, p. 405
3. J.D. Bjorken, S.K. Mtingwa, Part. Accel. **13**, 115 (1983)
4. L.D. Landau, Phys. Z. Sowjetunion **10**, 154 (1936)
5. M.N. Rosenbluth, W.M. MacDonald, D.L. Judd, Phys. Rev. **107**, 1 (1957)
6. S. Chandrasekhar, Rev. Mod. Phys. **15**, 1 (1943)
7. S. Nagaitsev, Phys. Rev. ST Accel. Beams **8**, 064403 (2005)
8. S. Ichimaru, M.N. Rosenbluth, Phys. Fluids **13**, 2778 (1970)
9. V. Lebedev et al., NIM A **391**, 176 (1997)
10. V. Parkhomchuk, *Physics of fast electron cooling*, in Proceedings of the Workshop on Electron Cooling and Related Applications, Karlsruhe, 1984
11. J.D. Jackson, *Classical Electrodynamics*, 3rd edn. (Wiley, New York, 1998)
12. C. Bernardini et al., Phys. Rev. Lett. **10**, 407 (1963)
13. J. Haissinski, LAL Orsay report 41-63 (1963)
14. V. Levedev, in *Proceedings HB-2004 Bensheim*, AIP Conference Proceedings, vol. 773, New York, 2005, p. 440
15. G. Dome, *Diffusion due to RF Noise*, in Proceedings of the CERN Accelerator School Advanced Accelerator Physics Course, Oxford, 1985, Preprint CERN 87-03 (April 1987), pp. 370–401
16. I.S. Gradshteyn, I.M. Ryzhik, *Tables of Integrals, Series and Products* (Academic, New York, 1980)
17. H. Hancock, *Theory of Elliptic Functions* (Dover Publications, New York, 1958)
18. V. Lebedev, L. Nicolas, A. Tollestrup, beams-doc-1155 (2004)
19. V. Shiltsev et al., Phys. Rev. ST Accel. Beams **8**, 101001 (2005)
20. V. Shiltsev, A. Tollestrup, Emittance growth mechanisms in the Tevatron beams. JINST **6**, P08001 (2011)
21. N.V. Mokhov, *Beam Collimation at Hadron Colliders*, in AIP Conference Proceedings, vol. 693, 2003, pp. 14–19
22. M.D. Church, A.I. Drozhdin, A. Legan, N.V. Mokhov, R.E. Reilly, *Tevatron Run-II Beam Collimation System*, in Proceedings of the 1999 IEEE Particle Accelerator Conference (IEEE Conference Proceedings, New York, 1999), pp. 56–58; Fermilab-Conf-99/059
23. I. Baishev, A. Drozhdin, N. Mokhov, STRUCT Program User's Reference Manual, SSCL-MAN-0034 (1994)
24. N.V. Mokhov, The MARS Code System User Guide, Version 13(95), Fermilab-FN-628 (1995); N.V. Mokhov et al., Fermilab-Conf-98/379 (1998); LANL Report LA-UR-98-5716 (1998); *nucl-th/9812038 v2 16 Dec 1998*; http://wwwap.fnal.gov/MARS/
25. L.Y. Nicolas, N.V. Mokhov, Impact of the A48 Collimator on the Tevatron BØ Dipoles, FERMILAB-TM-2214, June 2003
26. K.-H. Mess, M. Seidel, Nucl. Instrum. Methods A **351**, 279 (1994)
27. N. Mokhov, J. Annala, R. Carrigan, M. Church, A. Drozhdin, T. Johnson, R. Reilly, V. Shiltsev, G. Stancari, D. Still, A. Valishev, X.-L. Zhang, V. Zvoda, Tevatron beam halo collimation system: design, operational experience and new methods. JINST **6**, T08005 (2011)
28. J.M. Butler, D.S. Denisov, H.T. Diehl, A.I. Drozhdin, N.V. Mokhov, D.R. Wood, Reduction of TEVATRON and Main Ring induced backgrounds in the DØ detector. Fermilab FN-629 (1995)
29. A.I. Drozhdin, V.A. Lebedev, N.V. Mokhov et al., *Beam Loss and Backgrounds in the CDF and D0 Detectors due to Nuclear Elastic Beam-Gas Scattering*, in Proceedings of the 2003 IEEE Particle Accelerator Conference, Portland, 2003, pp. 1733–1735; Fermilab-FN-734
30. Tevatron Sequencer Software Help and Explanation. http://wwwbd.fnal.gov/webhelp_edit/pa1028/pa10281_1.html

31. X.-L. Zhang et al., Phys. Rev. ST Accel. Beams **11**, 051002 (2008)
32. E. Tsyganov, Fermilab preprint FNAL-TM-682 (1976)
33. V.M. Biryukov, Y.A. Chesnokov, V.I. Kotov, *Crystal Channeling and Its Application at High Energy Accelerators* (Springer, Berlin, 1997)
34. M. Maslov, N. Mokhov, L. Yazynin, Preprint SSCL-484 (1991)
35. R.A. Carrigan Jr. et al., Phys. Rev. ST Accel. Beams **1**, 022801 (1998)
36. R.A. Carrigan Jr. et al., Phys. Rev. ST Accel. Beams **5**, 043501 (2002)
37. R.A. Carrigan Jr. et al., Fermilab preprint FNAL-Conf-06-309 (2006)
38. N. Mokhov et al., in *Proceedings of the 2009 IEEE Particle Accelerator Conference,* Vancouver, 2009, p. 1836
39. V. Shiltsev et al., in *Proceedings of the International Particle Accelerator Conference*, Kyoto, 2010, p. 1243
40. W. Scandale et al., Phys. Rev. Lett. **101**, 234801 (2008)
41. R. Fliller et al., Phys. Rev. ST Accel. Beams **9**, 013501 (2006)
42. V. Biryukov, CATCH, 1.4 User's Guide. CERN SL/Note 93-74 AP (1993)
43. V. Shiltsev, in *Proceedings of LHC-LUMI-06 CARE-HHH-APD Workshop,* Valencia, 2006, CERN-2007-002 (2007), p. 92
44. V. Shiltsev, in *Proceedings of BEAM07 CARE-HHH-APD Workshop,* Geneva, 2007, CERN-2008-005 (2007), p. 46
45. D. Shatilov et al., in *Proceedings of the 2005 IEEE Particle Accelerator Conference,* Knoxville, 2005, p. 4138
46. G. Robert-Demolaize et al., in *Proceedings of the 2005 IEEE Particle Accelerator Conference,* Knoxville, 2005, p. 4084
47. V. Shiltsev et al., in *Proceedings of the European Particle Accelerator Conference,* Genoa, 2008, p. 292
48. J.C. Smith et al., in *Proceedings of the 2009 IEEE Particle Accelerator Conference,* Vancouver, 2009, WE6RFP031
49. G. Stancari et al., in *Proceedings of the International Particle Accelerator Conference,* Kyoto, 2010, p. 1698
50. G. Stancari et al., in *Proceedings of 14th Advanced Accelerator Concepts Workshop*, Annapolis, 2010, AIP Conference Proceedings 1299, 638
51. G. Stancari et al., in *Proceedings of the 2011 IEEE Particle Accelerator Conference,* New York, 2011, MOP147
52. G. Stancari et al., Phys. Rev. Lett. **107**, 084802 (2011)
53. M. Seidel, Ph.D. Thesis, Hamburg University, DESY 94-103 (1994)
54. D. Edwards, M. Syphers, *Introduction to the Physics of High Energy Accelerators* (Wiley, New York, 1993)
55. J. Steimel et al., in *Proceedings of the 2003 IEEE Particle Accelerator Conference,* Portland, 2003, p. 48
56. A. Wrulich, Single-Beam Lifetime, in *CERN Accelerator School, 5th General Accelerator Physics Course*, CERN Preprint 94-001 (1994)
57. V. Lebedev, in *Proceedings of the 33rd ICFA Advanced Beam Dynamics Workshop on High Brightness Hadron Beam* (Bensheim, 2004), AIP Conference Proceedings 773, in I. Hoffmann (ed) Comprehensive theoretical analysis of the longitudinal diffusion due to RF noise can also be found in S. Krinsky and J.M. Wang. Part. Accel. **12** (1982), p. 107
58. V. Lebedev, *Beam Physics at Tevatron Complex*, in *Proceedings of the 2003 IEEE Particle Accelerator Conference*, Portland, 2003, p. 29
59. N.V. Mokhov, V.I. Balbekov, Beam and luminosity lifetime, in *Handbook of Accelerator Physics and Engineering*, ed. by A.W. Chao, M. Tigner, 2nd edn. (World Scientific, Singapore, 2002), p. 218
60. A. Valishev, Tevatron store analysis package, Software code supported in 2006–2011, http://www-bd.fnal.gov/SDAViewersServlets/valishev_sa_catalog2.html